MULTI-JUNCTION THIN FILM SOLAR CELLS FOR AN OPTIMAL LIGHT HARVESTING

Paola MANTILLA PÉREZ

ICFO - INSTITUT DE CIÈNCIES FOTÒNIQUES

UNIVERSITAT POLITÈCNICA DE CATALUNYA

BARCELONA, 2017

MULTI-JUNCTION THIN FILM SOLAR CELLS FOR AN OPTIMAL LIGHT HARVESTING

Paola MANTILLA PÉREZ

Under the supervision of

Prof. Jordi MARTORELL

submitted this thesis in partial fulfilment

of the requirements for the degree of

DOCTOR

by the

UNIVERSITAT POLITÈCNICA DE CATALUNYA

BARCELONA, 2017

Agradecimientos

En primer lugar quiero agradecer a mi supervisor Profesor Jordi Martorell por la oportunidad de desarrollar mi labor investigativa dentro de su grupo y en este instituto. Esta oportunidad me ha permitido dedicarme a lo que ha sido desde hace algún tiempo mi pasión, la fotovoltaica. Agradezco su guía, los conocimientos aportados y la confianza que ha tenido en mi trabajo.

Un lugar importante también lo han tenido mis compañeros de trabajo. En particular quiero agradecer a Rafa, Marina y Xavi, antiguos compañeros, quienes me enseñaron la mayoría de nociones necesarias para desenvolverme en el laboratorio y en las tareas cotidianas de un investigador dentro del ICFO. De Marina y Xavi debo decir que fueron excelentes fuentes de conocimiento sobre la cultura, el carácter y el humor catalán. Aparte de ellos, han pasado otros muchos investigadores dentro del grupo quienes me han aportado desde lo profesional, pero también desde lo personal. Muchas gracias a todos por su ayuda y disponibilidad.

Agradezco también al grupo de Optoelectronics dirigido por el profesor Valerio Pruneri en ICFO, al igual que investigadores de EMPA y EPFL en Suiza, por su colaboración a la hora de obtener resultados importantes en este trabajo de tesis.

Con particular gratitud me refiero a todos los departamentos de este instituto. Desde el personal de logística, mantenimiento, compras, recursos humanos, recepción, comunicaciones, IT, KTT, etc. Sólo he encontrado amabilidad y eficiencia a la hora de solicitar su ayuda. Agradezco el apoyo que me han prestado durante todos estos años.

A mis amigos también muchas gracias por su interés, por sus consejos y reflexiones. Finalmente, agradezco a mi esposo y mi familia de un lado y otro del Atlántico por su apoyo constante e incondicional.

Abstract

Thin film photovoltaics encompass a group of technologies able to harvest light within a few microns thickness. The reduced thickness allows a low cost of manufacture while making the films flexible and adaptable to different surfaces. This, combined with their low weight, positioned thin film solar cells as ideal candidates for building integrated photovoltaics. For the latter, organic solar cells (OSC) can provide a high quality semi-transparency that closely mimics the aesthetics of standard windows.

Indeed, some unique features of organic solar cells make them the optimal solution for applications where standard Si technology cannot be used. However, for large-scale electricity production where efficiency is, perhaps, the most determining factor, newer thin film technologies like perovskites solar cells may be a more adequate option. At the moment of writing this thesis, state of the art efficiencies of single junction perovskites nearly double that of the best single junction organic solar cell. A limitation found in both technologies, especially in organics and to a lesser degree in perovskites, is the low mobility of the carriers. This, together with other processing shortcomings in the organic absorbers and perovskites limit their thickness to 100-130 nm, and 500-600 nm, respectively. In summary, light management must be an essential ingredient when designing device architectures to achieve the optimal performance in the specific application being considered.

In this thesis, in order to achieve an optimal light harvesting and therefore increase the performance of thin film solar cells, we take two approaches. On one hand, we increase the total thickness of the absorber material used in the device

without increasing the thickness of the single active material layer and, on the other hand, we combine complementary absorbers to cover a wider portion of the solar spectra. These approaches pose the double challenge of finding the optimal electromagnetic field distribution within a complicated multilayer structure containing two or more active layers, while at the same time implementing an effective charge collection or recombination in the intermediate layers connecting two adjacent sub-cells. In the case of OSC, we consider multi-junction cells where the same active material is used in all the junctions. This can be implemented by fabricating structures where the active layer thickness in each sub-cell does not exceed the 100 nm. For other types of thin film solar cells, we consider configurations using complementary absorbers. In both cases, but particularly in the former one, a systematic approach to optimize light absorption is needed. In order to obtain such optimal configurations, we implement an inverse integration approach combined with a transfer matrix calculation of the electric field. Furthermore, we develop several new approaches to optimize charge collection in the sub-cell interconnection layers which we apply to tandem, triple, 4-terminal and series-parallel configurations.

The thesis has been organized into five chapters. Chapter 1 introduces concepts required for the development of the thesis work including the optical model. Chapter 2 describes the optical optimization and experimental implementation of current-matched multi-junction devices using PTB7:$PC_{71}BM$, including applications. In order to profit from the advantage of electrically separated devices, Chapter 3 evaluates different types of 4-terminal architectures using PTB7:$PC_{71}BM$ and PTB7-Th:$PC_{71}BM$. In one of the architectures we establish a serial-connection between sub-cells while in other we leave the sub-cells completely independent. Chapter 4 theoretically proposes a novel monolithic architecture combining perovskites and CIGS which does not require current-

matching. Finally, in Chapter 5, an in-depth study of the semi-transparent inner electrodes is given that include vacuum-based and solution-processed layers.

Resumen

La fotovoltaica de capa delgada engloba un grupo de tecnologías capaces de capturar la luz en tan sólo unos pocos nanómetros de espesor. Su bajo costo de manufactura, flexibilidad y bajo peso, hace a las capas delgadas candidatas ideales para la integración en edificios. En particular, las celdas orgánicas pueden proveer una transparencia de alta calidad similar a las ventanas convencionales irrealizable con tecnologías basadas en Silicio. Sin embargo, para la producción de electricidad a gran escala en donde la eficiencia es, tal vez, el factor determinante, existen nuevas tecnologías como las celdas solares de perovskita que pueden resultar más adecuadas. Al momento de escribir esta tesis, las eficiencias de celdas de perovskita de simple unión casi duplican la de las mejores celdas orgánicas de simple unión. Una limitante de ambas tecnologías, en especial de las celdas orgánicas y en menor medida de las perovskitas, es la baja mobilidad de las cargas. Esta, junto a otras desventajas de los absorbentes orgánicos y perovskitas limita su espesor al rango de los 100 a los 130 nm, y entre los 500 a 600 nm, respectivamente. En resumen, el manejo de la luz debe constituir un ingrediente esencial para el diseño de los dispositivos, tal que se consiga un desempeño óptimo en la aplicación para la cual sean considerados.

En esta tesis, con el fin de alcanzar un aprovechamiento óptimo de la luz y por ende aumentar el desempeño de las celdas solares de capa delgada, utilizamos dos enfoques. Por un lado, aumentamos el espesor total de material absorbente dentro del dispositivo sin incrementar el espesor de las capas activas individuales y por otro lado, combinamos absorbentes complementarios para cubrir una porción más amplia del espectro solar. Estos enfoques conllevan al doble reto de encontrar la distribución de campo electromagnético óptima dentro

de una estructura compleja de multicapas con dos o más capas activas, junto a la implementación de una recolección o recombinación de cargas efectiva por parte de las capas intermedias encargadas de conectar dos subceldas adyacentes. En el caso de las celdas orgánicas, consideramos celdas de multiunión usando el mismo material activo para todas las subceldas. Para implementarlas, se realizan estructuras cuyas capas activas no excedan los 100 nm. También estudiamos configuraciones donde los materiales tienen absorciones complementarias usando perovskitas. En ambos casos, sobretodo en el primero, se requiere un método sistemático para optimizar el aprovechamiento de la luz. Para obtener las configuraciones óptimas empleamos una estrategia de integración inversa junto con un cálculo del campo eléctrico basado en el modelo de matriz de transferencia. Además, desarrollamos nuevas estrategias para optimizar la colección de cargas en las capas de interconexión de las subceldas aplicables a dispositivos tipo tandem, triple, 4-terminales y serie-paralelo.

Esta tesis ha sido organizada en cinco capítulos. El primero introduce los conceptos necesarios para el desarrollo de este trabajo de tesis incluyendo el modelo óptico. El capítulo 2 describe la optimización óptica e implementación experimental de arquitecturas de multiunión que cumplen el criterio de igualación de corrientes usando PTB7:$PC_{71}BM$, incluyendo aplicaciones. Para aprovechar las ventajas de subceldas intrínsicamente desconectadas, en el capítulo 3 se evalúan diferentes tipos de celdas de 4 terminales usando PTB7:$PC_{71}BM$ y PTB7-Th:$PC_{71}BM$. En una de estas arquitecturas, las subceldas se conectan externamente en serie mientras que en otra las subceldas se dejan completamente independientes. El capítulo 4 propone teoréticamente una arquitectura nueva y monolítica, combinando celdas de perovskita y CIGS, y que no requiere igualación de corrientes. Finalmente, en el capítulo 5 se presenta un estudio detallado de electrodos semi-transparentes que incluye opciones basadas en métodos de vacío y a través de capas fabricadas por disoluciones.

List of publications

Included in this thesis:

1. *4-Terminal Tandem Photovoltaic Cell Using Two Layers of PTB7:$PC_{71}BM$ for Optimal Light Absorption.* Paola Mantilla-Perez, Alberto Martinez-Otero, Pablo Romero-Gomez, and Jordi Martorell. ACS Appl. Mater. Interfaces 2015, 7 (33), pp 1843518440.

2. *Monolithic CIGS-Perovskite Tandem Cell for an Optimal Light Harvesting Without Current Matching.* Paola Mantilla-Perez, Thomas Feurer, Juan-Pablo Correa-Baena, Quan Liu, Silvia Colodrero, Johann Toudert, Michael Saliba, Stephan Buecheler, Anders Hagfeldt, Ayodhya N. Tiwari and Jordi Martorell. ACS Photonics. Accepted.

3. *Oxide layers in organic solar cells for an optimal photon management.* Chapter in book *The Future of Semiconductor Oxides in Next Generation Solar Cells.* Elsevier. Paola Mantilla-Perez, Q. Liu, Pablo Romero-Gomez, Silvia Colodrero, Jordi Martorell. In progress.

4. *An extremely thin and robust interconnecting layer providing 76% fill factor in a tandem polymer solar cell architecture.* Alberto Martnez-Otero, Quan Liu, Paola Mantilla-Perez, Miguel Montes Bajo and Jordi Martorell. J. Mater. Chem. A, 2015,3, 10681-10686.

5. *Neutral Water Splitting Catalysis with a High FF Triple Junction Polymer Cell* Xavier Elias, Quan Liu, Carolina Gimbert-Suriach, Roc Matheu, Paola Mantilla-Perez, Alberto Martinez-Otero, Xavier Sala, Jordi Martorell, and Antoni Llobet. ACS Catal., 2016, 6 (5), pp 3310331.

Other publications:

6. *A two-resonance tapping cavity for an optimal light trapping in thin-film solar cells.* Quan Liu, Pablo Romero-Gomez, Paola Mantilla-Perez, Silvia Colodrero, Johann Toudert and Jordi Martorell. Adv. Ener. Mater. Accepted.

7. *An Indium Tin Oxide-Free Polymer Solar Cell on Flexible Glass.* Nadia Formica, Paola Mantilla-Perez, Dhriti S. Ghosh, Davide Janner, Tong Lai Chen, Minghuang Huang, Sean Garner, Jordi Martorell, and Valerio Pruneri. ACS Appl. Mater. Interfaces, 2015, 7 (8), pp 45414548.

8. *Enhanced light harvesting in semitransparent organic solar cells using an optical metal cavity configuration.* Francesco Pastorelli, Pablo Romer-Gomez, Rafael Betancur, Alberto Martinez-Otero, Paola Mantilla-Perez, Nicolas Bonod, Jordi Martorell. Adv. Energy Mater. 2014, 1400614.

9. *Highly Flexible Transparent Electrodes Containing Ultrathin Silver for Efficient Polymer Solar Cells.* Dhriti Sundar Ghosh, Quan Liu, Paola Mantilla-Perez, Tong Lai Chen, Vahagn Mkhitaryan, Minghuang Huang, Sean Garner, Jordi Martorell, Valerio Pruneri. Adv. Funct. Mater. 2015, 25, 7309-7316.

10. *Nanoparticle Assisted Mechanical Delamination for Freestanding High Performance Organic Devices.* Silvia Colodrero, Pablo Romero-Gomez, Paola Mantilla-Perez, Jordi Martorell. Adv. Funct. Mater. 2016.

11. *UV-Induced Oxygen Removal for Photostable, High-Efficiency PTB7-Th:$PC_{71}BM$ Photovoltaic Cells.* Quan Liu, Paola Mantilla-Perez, Miguel Montes Bajo, Pablo Romero-Gomez, and Jordi Martorell. ACS Appl. Mater. Interfaces, 2016, 8 (42), pp 2875028756.

12. *Semi-transparent polymer solar cells.* Pablo Romero-Gomez, Francesco Pastorelli, Paola Mantilla-Perez, Marina Mariano, Alberto Martinez-Otero, Xavier Elias, Rafael Betancur, Jordi Martorell. J. Photon. Energy. 5(1) 057212.

Book chapter:

13. *Organic & Hybrid Photonic Crystals* by Davide Camoretto. 2014. Ed. Springer Science & Business and Media. Chapter: *One-dimensional photonic crystals for light management in organic solar cells.* M. Mariano, Paola Mantilla-Perez, Pablo Romero-Gomez, Alberto Martinez-Otero, Xavier Elias, Rafael Betancur and Jordi Martorell.

Contents

Chapter 1

Introduction

For many centuries, the levels of atmospheric carbon dioxide in earth have varied between the 180 ppm and 280 ppm. From 1950, this trend has changed to a steep incline reaching the current level of 400 ppm [1]. This represents an increase of 40% compared to pre-industrial levels. Based on this fact, and all the collected scientific evidence, most of the climate scientists agree that climate warming over the last century is caused very likely by human activities [2].

Among the effects of human-induced climate change, there are increases in ocean and freshwater temperatures, frost-free days and heavy downpours. Additionally, the global sea level has risen while there have been reductions in snow-covered areas and sea ice [3]. If the warming trend continues, it is likely that major changes in the ecosystems will occur, including extinction of some species or relocation of others. The increase in sea levels could lead to intrusion into freshwater aquifers, thus threatening sources of drinking water and the growing of crops. In addition, it might force populations to evacuate certain areas. Even if all the possible consequences of a rising world temperature are not completely clear, under the scenarios considered, climate change could have an impact on human living, mainly for the worse, affecting basic needs and sectors such as energy

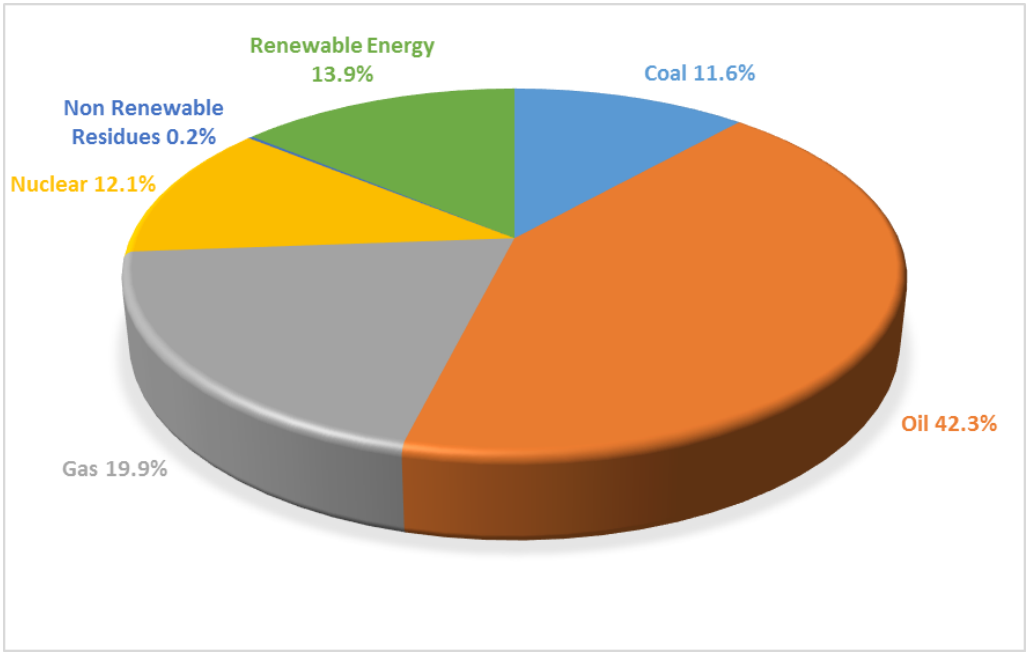

Figure 1.1: Percentage of primary energy consumption in Spain in 2015 [5].

and transportation. To diminish the consequences of climate change, it has been proposed to keep the increase in the average global temperature to well below 2°C above pre-industrial levels, and, furthermore, to aim to limit the increase to 1.5°C [4].

From the technological point of view, reaching the above-mentioned objectives implies a huge effort to change the current energy usage scenario into a more sustainability-oriented one. As a case study, one could observe the primary energy consumption in Spain during 2015 and clearly contemplate a scheme dominated by the use of oil (see Figure 1.1).

Clean energy sources like wind energy, solar and hydropower become important in a new greener scenario. In particular, solar energy benefits from certain

advantages. Solar power, for instance, is one of the most environment friendly renewable energy options. It allows for a simple mounting and the possibility of being installed in difficult to access terrains [6]. PV systems don't pollute the air and don't produce noise, which makes them suitable for installation within or close to the sites where the energy is demanded. Moreover, solar is one of the renewable energy solutions that easily integrates with building façades as an additional architectural design element.

The evolution of photovoltaic technology has often been described by three generations of solar cell devices. The first generation comprises devices fabricated with monocrystalline silicon operating under a semiconductor p-n junction. This technology has proven its effectiveness and stability, and it is the most wide spread on the market, representing around 93% of the world's total production in 2015 [7]. The next generation of solar cells, or so-called second generation, aims for processing methods requiring less energy and a lesser quantity of bulk material for the solar cell fabrication. The second generation of solar cells includes a part of the group of thin film technologies such as CIGS, amorphous Si and CdTe. This second generation of PV exhibits new advantages including flexibility, light-weight and building integration capability. However, there is still a huge gap between the best lab scale devices compared to the modules, caused mainly by poor material homogeneity and uniformity across large areas [8]. The third generation of solar cells comprises the so-called emerging technologies. Among them, there are multi-junction tandem solar cells, organic solar cells (OSC), dye sensitized solar cells (DSSC) and perovskite solar cells (PVK). In principle, the latter are also thin film technologies given that the active materials stay in the nanometer range. At the time that the third generation of solar cells started, the aim was to reduce the cost of second generation photovoltaics, which was in the $ 1/W level, to values of $ 0.5/W or better by enhancing the efficiencies but

keeping the advantages of thin-film deposition technologies [9]. For this reason, new materials and architectures able to surpass the Schockley-Queisser limit were implemented.

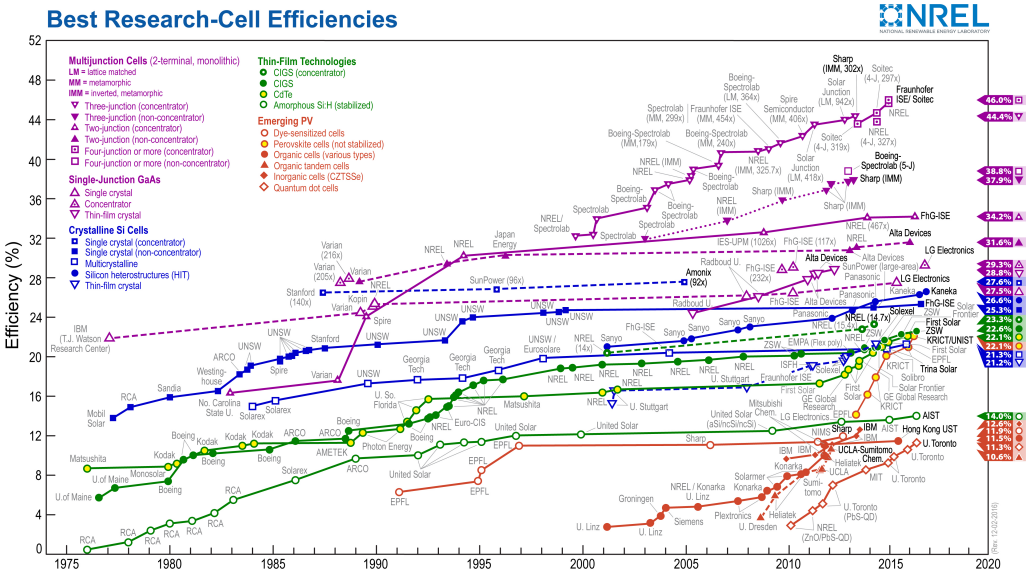

Figure 1.2: Best solar cell devices certified by NREL (Jan 2017) [10].

Intense research in the field of third generation photovoltaics has led to high power conversion efficiency (PCE) devices. These have already surpassed the 11% PCE for single junction OSC and 12% for tandem architectures as observed in the NREL efficiency chart depicted in Figure 1.2. On the other hand, Perovskites already show remarkably high PCEs above 22%.

1.1 Overview of thin film technologies

1.1.1 Organic solar cells (OSC)

OSC have attracted enormous interest given their compatibility with roll-to-roll processing and ability for semi-transparency [11, 12]. Currently, there exist other kinds of technology allowing easy manufacture; however, none of them can provide the neutral semi-transparency and stability of organic solar cells, which makes OSC still very competitive for building integrated photovoltaics (BIPV) .

In recent years, the PCE of single-junction organic solar cells has been rising steadily due to the implementation of several strategies that include optical trapping [13, 14, 15, 16], the design of new polymers [17, 18, 19], the use of ternary blends [20, 21], fullerene-free blends [22, 23] and interfacial engineering, among others. High performance blends including polymers like PTB7-Th, also known as PCE10, PffBT4T-2OD and PBDB-T have brought certified efficiency of OSC to values surpassing the 10% barrier [22].

However, further increasing the PCE is still severely limited by the low charge carrier mobility [24]. Many different factors including molecular packing, disorder or low crystallinity, the presence of impurities, temperature, electric field, charge-carrier density, size/molecular weight, and pressure can degrade such mobility [25]. The detrimental effects become more apparent for thicker blends by causing a dramatic reduction in fill factor (FF) for the majority of polymers [26]. Thus, increasing light absorption by means of thicker blends to obtain higher efficiencies is not a viable alternative. Different alternatives have been explored for the improvement of organic solar cells, as discussed in section 1.3.2.

1.1.2 Perovskite solar cells (PVK)

Perovskite solar cells have recently emerged as a promising technology for cost-effective photovoltaics [27, 28, 29, 30, 31, 32]. A wide variety of perovskite architectures have shown the remarkable opto-electronic properties of these materials, which in less than five years have reached efficiencies above 20% [33, 34, 35] . Perovskites are crystallized from organic and metal halide salts to build ABX_3 structured crystals, where A is the organic cation, B is the metal cation and X is the halide anion [36].

One interesting characteristic of organic-inorganic metal trihalide perovskites is the tunability of their bandgap by means of substituting both cation and anion [37, 38, 39]. For instance, the perovskite structure $MAPb(I_{1-x}Br_x)_3$ can be tuned in composition following the substitution of I with Br to exhibit bandgaps from 1.57 eV to 2.29 eV. This capability allows, among other things, the application of PVK in tandem devices using only PVK, silicon or CIGS [40, 41, 42, 43, 44, 45]. In fact, given the low prices per watt of the electricity generated by commercial silicon solar cells, PVK have arisen lately as an interesting material to enhance efficiency of silicon solar cells by using multi-junction configurations [133, 47, 48, 49, 50].

1.1.3 Other thin film solar cells

Solar cells based on $CuIn_{1-x}Ga_xSe_2$ absorbers, also known as CIGS, are currently the most efficient devices within the second generation of photovoltaics, with a laboratory scale PCE of 22.6% [51]. However, scarcity of indium and its growth in price motivated by the demand of display manufacturers [52] is expected to limit the production of CIGS solar cells.

To circumvent this problem, a new type of solar cells, denominated Kesterites,

were developed. In structure, they are similar to CIGS solar cells but the indium is replaced with non-toxic, earth-abundant, lower cost materials such as Tin and Zinc [53]. Their efficiency has remained at 12.6% since 2013 [54]. There are currently several aspects that need improving in these devices, including reducing bulk defects within the kesterite, improving interfaces to achieve higher V_{oc}, and passivation of defects at grain boundaries, among others [52].

Quantum dot solar cells are another type of inorganic devices. Apart from enabling solution processing, an important advantage of these devices is their ability to tune the optical and electrical properties by adjusting the size and shape of the nanoparticles [55, 56, 57]. Recent colloidal quantum dot research has focused on methods for nanoparticles synthesis, and film processing [58, 59]. Power conversion efficiencies above 11% have already being reached [10]. Efforts towards the improvement of electronic transport are required, such as a reduction of defects, elimination of trap states and an increase in nanocrystal packing [60].

Cadmium Telluride solar cells (CdTe) are also thin film devices, fabricated by either high-temperature ($\geq$770K) or low-temperature ($\leq$670K) based processes. The first group include methods as close-spaced sublimation, vapor transport deposition and atmospheric pressure vapor transport deposition and the latter include high vacuum evaporation, sputtering, spray pyrolysis and electro-deposition [61]. Considering the market share of thin film devices, CdTe solar cells have been above CIGS and amorphous silicon for the last 9 years [7]. The performance of CdTe solar cells has recently been improved, especially in terms of photocurrent, but further efforts are needed to improve the V_{oc} and FF. Recently, the company First Solar achieved an efficiency of 18.6% for CdTe modules, similar to that of polysilicon solar modules.

1.2 Working principles of thin film solar cells

1.2.1 Circuit model of single junction solar cells

Generic dark and illuminated current voltage (IV) curves of thin film solar cells can be fitted using the single diode model. This describes the IV behavior with four components: a photocurrent source, a diode, a serial resistor, and a shunt resistor. The photocurrent source represents the free charges generated after the light absorption, the diode accounts for the electron-hole recombination at the p-n junction, the serial resistor models the internal resistance of the cell (including the resistance of the electrodes) and the shunt resistor accounts for leakage current through the cells. The mathematical expression for the current throughout the solar cell upon illumination is as follows:

$$J = J_0 \left[exp\left(\frac{q(V - JR_S)}{nk_BT}\right) - 1 \right] + \frac{V - JR_S}{R_{SH}} - J_{sc} \tag{1.1}$$

where the first term represents the diode or recombination current, the second term the shunt current and the third term the generated photocurrent. Following the original p-n junction theory of Shockley, J_0 is the saturation current at reverse bias for an ideal p-n junction diode, V is the potential difference between the contacts, T is the temperature in Kelvin, n is the ideality factor of the diode and k_B is the Boltzmann constant. R_S is the internal series resistance of the cell and R_{SH} the parallel shunt resistance.

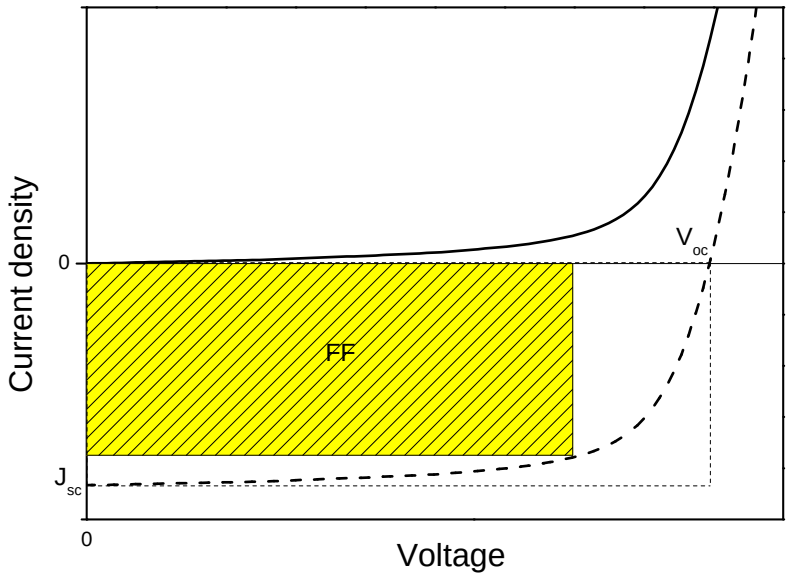

Figure 1.3: Typical JV curve of a solar cell.

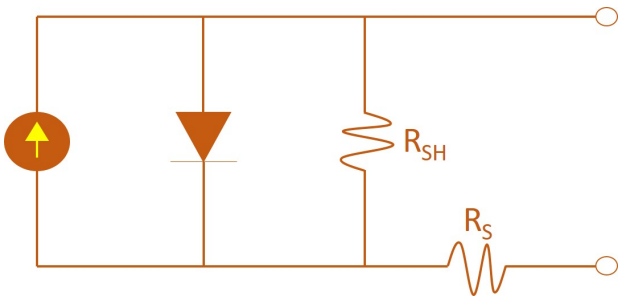

Figure 1.4: Circuit model of a solar cell.

The dark and illuminated JV curve of a solar cell is shown in Figure 1.3. The electrical parameters that characterize the device are the open circuit voltage V_{oc}, the short circuit current density J_{sc}, the fill factor FF, and the PCE. The

open circuit voltage is the maximum voltage that can be achieved by a solar cell. At the V_{oc} condition, the generated carriers balance with the recombined carriers leaving no net current at any position within the device. In most of the thin film solar cells, the V_{oc} shows a linear relation to the bandgap of the semiconductors. In the case of organic solar cells, there is a consistent linear relation between the V_{oc} and the difference between the HOMO level of the donor polymer and the LUMO level of the acceptor, with little dependence on the work function of the electrodes [62]. The J_{sc} is governed by the materials' absorption, together with interference effects that arise from stacking multiple layers with thicknesses in the order of the wavelength of light. This is measured when the voltage across the solar cell is zero. The so-called fill factor (FF) is a parameter that describes how much of the power product V_{oc}, J_{sc} can be provided by the solar cell, represented by the squareness of the JV curve. Ideally, the more squared the JV curve is, the more power can be delivered to the load. The PCE of a solar cell is expressed in terms of the V_{oc}, J_{sc} and FF using the following expression:

$$PCE = \frac{V_{oc} J_{sc} FF}{P_{in}} * 100 \tag{1.2}$$

where P_{in} corresponds to the incident power of light per unit area, which for AM 1.5 illumination is 100 mW/cm^2.

1.2.2 Operation of OSC

In the majority of inorganic semiconductors, free electrons and holes are produced directly upon light illumination. However, within organic semiconductors the absorption of light creates electron-hole pairs (excitons) which at room temperature are still bound and need additional energy for their dissociation [63, 64, 65]. The reason for these strongly bound excitons is the low dielectric constants of organic materials when compared with their inorganic counterparts, leading to an electron-hole binding energy in the range of 0.35-0.5eV that exceeds by an or-

der of magnitude the thermal energy value at room temperature. The HOMO and LUMO of organic molecules correspond to their Highest Occupied Molecular Orbital and Lowest Un-occupied Molecular Orbital, respectively, analog to the valence and conduction band in inorganic materials [66]. A way to facilitate the generation of free charges is having a difference in the LUMO between the donor and acceptor materials, that provides the driving force for the transfer of an electron from donor to acceptor molecule [11, 67].

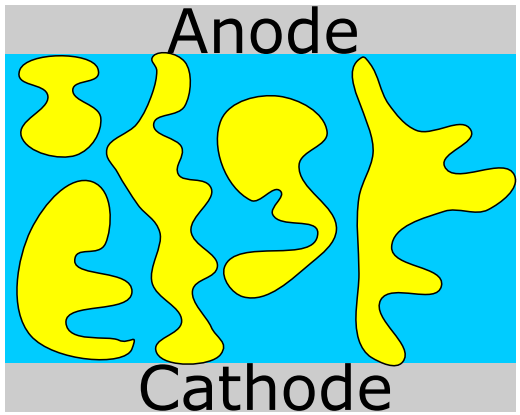

Figure 1.5: Bulk Heterojunction.

The first organic solar cells were fabricated with an organic heterojunction formed by a bilayer of donor (polymer) and acceptor (fullerene) material [68]. This approach proved better than just having a single polymer. The major improvement in organic solar cells, however, was introduced with the bulk heterojunction concept (see Figure 1.5)[69, 70]. A bulk heterojunction consists of a mix of polymer and fullerene materials where ideally both are phase segregated in the scale of 10 nm, which is the exciton diffusion length. Such nanomorphology favors the splitting of the excitons, which can reach an interface where they separate and are finally collected at the electrodes to produce a photocurrent in the external

circuit [71]. The film thickness of the bulk heterojunction is typically limited to 100 nm to minimize charge recombination losses from the low carrier mobilities in organic semiconductors. For instance, an electron mobility of 2 x 10^{-3} cm^2/Vs has been measured for the reference blend system P3HT:PCBM [72].

Although organic semiconductors are not intentionally doped, they have been found to contain holes as majority carriers. Such p-doping originates from negatively charged defects within the polymers, upon exposition to air or moisture [73, 74]. Under dark conditions, a Schottky barrier forms between the blend and the cathode after putting them together, thus generating a depletion region at this contact.

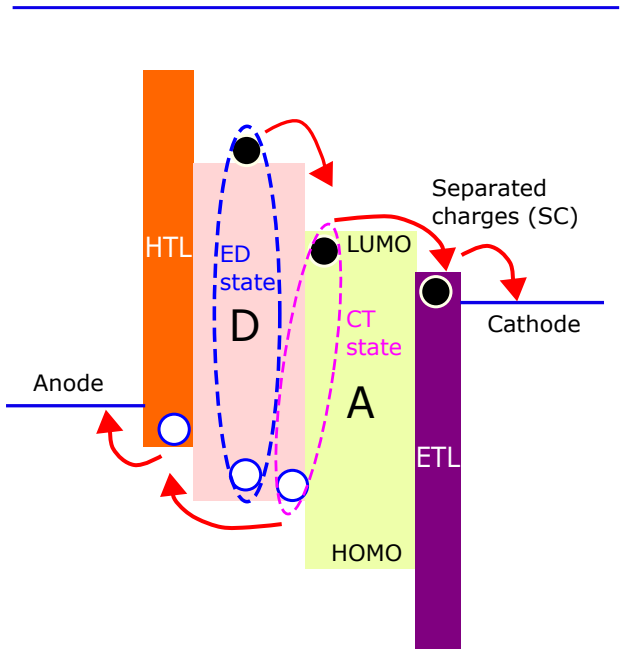

Figure 1.6: Charge generation in OSC.

A scheme for charge generation in a bulk heterojunction upon light illumination is depicted in Figure 1.6. According to this model, absorption of a photon

in the donor material generates a bound electron-hole pair or exciton (ED state). Upon relaxation to lower energy sites within the polymer, the exciton diffuses to the interface between donor (D) and acceptor (A) where the difference in the energy of the LUMO levels enables the transfer of an electron onto the acceptor. At this point, a bound electron-hole state at the interfaces called charge transfer state CT is created. Such a state is an intermediate between excitons and completely dissociated charges [75, 76]. After the CT state, the bound charges may separate to overcome the Coulombic interaction and dissociate completely to be dragged towards the electrode by the internal build-in field, and eventually to be extracted as generated photocurrents (SC) [67]. The presence of a hole transporting layer (HTL) and an electron transporting layer (ETL), located at the proper energy levels with respect to the donor and acceptor respectively, guarantee that charges will flow in the right direction thus minimizing recombination.

The likelihood of photon conversion to charges can be described using the external quantum efficiency (EQE) according to:

$$EQE(\lambda) = A(\lambda)\eta_{ed}\eta_{ec}\eta_{cc} = A(\lambda)PTCCE \tag{1.3}$$

where $A(\lambda)$, η_{ed}, η_{ec} and η_{cc} correspond to the photon absorption, the efficiency of exciton diffusion, the efficiency of charge separation, and the efficiency of carriers transport and carriers collection, respectively. Except for the photon absorption, the rest of these parameters are wavelength independent and can be in general terms represented by one single product denoted as the absorbed photon to current conversion efficiency (PTCCE).

1.2.3 Operation of PVK

Perovskite films are typically placed in between p- and n-type selective layers. However, the fact that good efficiencies can be achieved in PVK also without the

electron or hole selective layers indicate that, as opposed to organic solar cells, PVK are good electron and hole conductors [77, 78].

The diffusion length has been estimated to surpass one micron for both electrons and holes in films processed from mixed-halide precursor solutions [79, 80]. Such a diffusion length derives from the high mobility of electrons and holes in the range of 10 to 30 cm^2/Vs. The exciton binding energy is also an important parameter to describe electronic properties. Initial studies of different phases of PVK have determined an exciton binding energy in the range of 37 to 50 meV [81, 82]. Nevertheless, more recent studies argue that at room temperature the exciton binding energy is only a few millielectronvolts, suggesting that the photovoltaic performance is mainly a free-carrier phenomenon [83].

Figure 1.7 shows a common architecture for perovskites. A layer of mesoporous TiO_2 lies above a compact layer of TiO_2. The PVK material infiltrates the mesoporous TiO_2 [84, 85, 86]. Upon photon absorption, a free electron and a free hole are generated inside the PVK. The electron travels through the n-type mesoporous and compact layers of TiO_2 towards the FTO cathode, while the hole reaches the Au anode through a hole transporting material. PVK absorbers have been tested within a large variety of architectures employing different hole and electron transporting layers [87, 88]. Both types of transporting layers have been shown to reduce the recombination rates in PVK, and in particular, the hole transporting layer has been found to improve the V_{oc} [89].

For the electron transporting layers different materials have been used including TiO_2, ZnO, Al_2O_3, PCBM. Similarly, for the hole transporting layers, a large group of tested materials have been trialed such as Spiro O-MeTAD, PTAA, P3HT, PEDOT:PSS and PCPDTBT [90]. A huge amount of the different architectures have proved effective, thus showing the enormous versatility of these

materials.

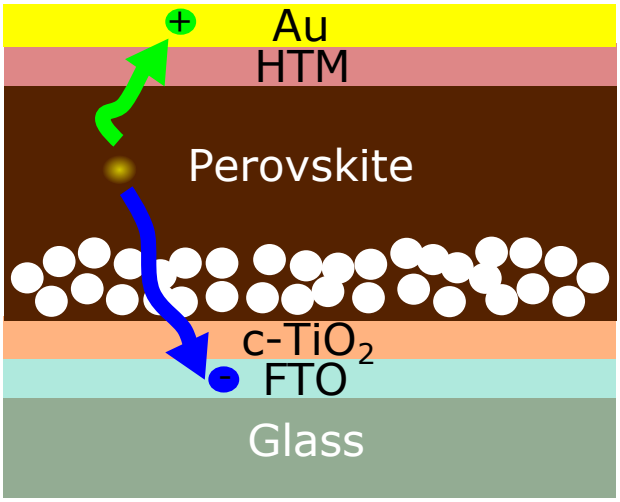

Figure 1.7: Operation of a PVK solar cell.

1.3 Overcoming efficiency limitations of single junction organic solar cells

1.3.1 Improving V_{oc}

One main limitation that has been encountered for OSC is the relatively large voltage loss from the absorber bandgap to the V_{oc} of the solar cell. Such a voltage loss, coming from the energy offset between the bandgap of the blend system and the energy of the CT state, is required for charge separation in OSC. Paths towards improvement of the V_{oc} in organic solar cells include the development of new polymer-acceptor systems where the driving force required for charge separation is minimal, for instance, blend systems deploying non-fullerene acceptors [91].

1.3.2 Light harvesting techniques

As previously mentioned, the photoactive material in OSC is typically limited to 100 nm. Such a small thickness leads to insufficient photon absorption within the active material. As a consequence, it is very important to manage light inside the OSC such that the electromagnetic field intensity is maximized within the photoactive layers. To achieve that, a model employing the optical properties of each composing layer has been developed, which takes into account effects such as reflections and interferences [92]. With regard to the materials, improvements in the photocurrent may arise from the use of buffer layers exhibiting low extinction coefficients. In this way, parasitic absorption coming from these layers is reduced [93, 94]. Tuning the thicknesses of the layers in opaque OSC is also an effective way to obtain an optimal interference inside the cells [95, 96]. In the case of semi-transparent devices, optical management has proven to be particularly relevant [97]. In such cases, incorporation of periodic photonic structures on top of the semi-transparent metallic electrode allows for the re-harvesting of near-infrared photons [98, 99]. Even more interesting is the use of non-periodic photonic structures in semi-transparent devices to re-harvest both near-UV and near-infrared photons [100] such that the resulting device reaches 80% of the efficiency of the opaque reference, with a luminosity of 30% in the visible range. A direct approach towards obtaining a larger transparency in the visible has also been employed, which consists in lowering the band-gap of the absorber polymers. This approach can generate a nice colorless level of transparency [101, 102, 103]. Photonic crystals have also been combined with low band-gap polymers to enhance both efficiency and transparency in the visible [104, 105].

Besides the optimization of 1D flat architectures, photocurrent enhancements have also been demonstrated by the incorporation of micro layers and by the nanostructuring of charge extraction layers [106], photoactive layers or the sub-

strate itself. For instance, Moths eye nanostructures (MEN) have been patterned on the PEDOT:PSS or ZnO layer on ITO coated substrates of OSC. Then, organic layers and the top metal electrode have been deposited following a conformal coating. Compared to flat references, such nanostructured devices can achieve improvements of up to 20% in the photocurrent (when also incorporating the MEN on the substrate side) [107]. An improvement of 7.8% in the photocurrent has also been demonstrated for the case of a MEN incorporated directly on the photoactive layer [108].

Another alternative has been the application of plasmonics to OSC. Surface plasmons have been exploited in OSC to induce light trapping [109, 110, 111, 112]. This occurs because the metallic nanostructures scatter light that is then coupled into the photoactive layers. In many occasions the introduction of nanostructures within OSC have led to degradation of PV parameters like the V_{oc} or the FF. A method to incorporate a nanostructure on the top Ag electrode of an OSC which induces no cell degradation has been shown by Niesen et al. [113]. An improvement of almost 5% in the photocurrent was achieved when comparing with the best flat reference. Based on simulations and experimental results, the conclusion was that the main plasmonic effect behind the enhanced absorption was light scattering. The plasmonic structures have been inserted in different layers within the OSC. For instance, metallic nanoparticles have been incorporated in the hole transporting layer achieving current enhancements from 9% up to 20% [114, 115]. A similar effect has been obtained by implementing metallic nanoparticles in the active layers of OSC, which has increased the short circuit current up to 16% compared to the reference devices [116, 117, 118, 119].

There exist different light trapping elements that can be attached to the substrate to achieve photocurrent enhancements, without being in close contact to

the photoactive layers. A design employing a close-packed, hemispherical, transparent polymer microlens array (MLA) fabricated on top of the substrate where light is incident has been shown as a universal optical approach to enhance the efficiency of OSC. This is attributed to a longer optical path length for the incident light inside the photoactive layer and a reduced surface reflection induced by the MLA [13]. Additional structures have been explored with elements separated from the photoactive layer, including a pyramidal rear reflector [14], or a microprism substrate [15]. The former increases the optical path length in the active layer more than 2.5 times compared to a planar reflector. In the latter, a gain in the absorption in the photoactive layer results from the inclined incidence of radiation and from the multiple reflections. Another novel geometry that explodes the multiple reflections is the V-shaped architecture, where two cells are facing each other in a folded configuration. Reflected light experiences multiple bounces between both cells, thus increasing the probability of being absorbed. Such light would be lost in a planar configuration [16].

1.4 Multi-junction thin film solar cells

An interesting approach to increase solar cell efficiency is the multi-junction configuration obtained by stacking different materials with complementary absorption to harvest energy from a larger portion of the solar spectra [120, 121, 122, 123, 124]. An efficiency of 13.2%, the highest efficiency for an organic solar cell to date, has been reached by using a multi-junction approach combining three different absorbers [125]. Lately, newer materials like perovskites have shown themselves to be promising options for efficient multi-junction devices, together with more mature PV technologies employing different architectures [41, 42, 43, 44]. The most common configuration, where two sub-cells based on different active materials are piled up, is also known as $hetero-tandem$. On the other hand, the use

of the same active material in the sub-cells has also proven effective in enhancing absorption and efficiency, with the added advantage of being available to more OSC research groups, as only a few are able to design high quality polymers with tailored absorption profiles [126, 127, 128]. This configuration is also known as $homo-tandem$. In this work, we will also discuss homo-triple devices, which are composed of three serially connected layers of the same active material.

In the tandem structures, regardless of the active materials chosen, the sub-cells are deposited one on top of the other using an intermediate layer which connects them electrically in series. This type of architecture might be also referred to as 2-terminal. A second approach is to develop devices which are not intrinsically connected but instead are separated by a dielectric layer, having the full set of electrodes free, referred as 4-terminal architectures (for the case of two active layers) [129, 130]. A posteriori, the cells can be connected in series or parallel, according to the application. The need for an interconnecting layer and intrinsic current-matching is removed in this architecture.

1.4.1 Semi-transparent electrodes (TE) for multi-junction solar cells

In any of the configurations used to achieve a multi-junction solar cell, it is necessary to include one or more semi-transparent electrodes in between the absorber materials. This is particularly challenging, as organic layers can usually withstand only specific deposition methods, thus limiting the type of electrodes that can be deposited on top of them.

In the case of tandem solar cells, the composed semi-transparent electrode that serves as a common connection between front and rear sub-cells is referred to as an interconnecting layer or ICL. This ICL must comply to strict criteria, for

instance, it should efficiently collect holes from one of the sub-cells in order to recombine them with electrons from the other sub-cell. Processing of the ICL must be compatible with the bottom layers and, furthermore, the finished ICL must have surface properties that allow the deposition of the top layers [131, 132]. The energy levels of the ICL must match on one side, the acceptor's HOMO of one subcell and on the other side, the donor's LUMO of the other subcell similarly to the case of anodic and cathodic buffer layers within single junction devices. Optically, the ICL must show a high level of semi-transparency, to avoid parasitic losses. The ICLs are formed by metallic or semi-metallic layers [120], by tunnel junctions (n++/p++) [133, 134] and by sequential deposition of thin layers of an n-type material, a p-type material and ultra-thin evaporated metallic layers (usually between 0.5 and 2 nm) in between [135, 136, 137]. Other alternatives include fully solution processed ICLs containing modified PEDOT:PSS formulations and ZnO [138, 123].

The need for semi-transparent inner TEs is as important in the 4-terminal architecture, as it is for tandem devices. The TEs used in this kind of structure are, however, typically less transparent than ICLs because they require a higher degree of lateral conductivity for the extraction of charges. This conductivity is mainly achieved by increasing the thicknesses of the thin metallic layers (to around 10 nm). Within 4-terminal devices, a transparent dielectric layer is introduced, which separates the TEs of both sub-cells. As a consequence, deposition of the second sub-cell is not directly on top of the semi-transparent TE but on the dielectric in this case. Evaporated oxide/metal/oxide structures are a typical alternative, given their compatibility with organic layers and the high-transparencies that they can reach. An example is the electrode comprising MoO_3/Ag/MoO_3 also denominated as MAM, which has been used both as an anode and a cathode in single junction solar cells [139, 140]. A similar structure

using Au has also been demonstrated [141, 142].

4-terminal structures can also be obtained by stacking two cells, without requiring a monolithic integration, with each of them being in their respective substrate. In such cases, if one of the inner TEs were built upon a glass substrate, it could be sputtered as in the case of ITO or other multi-layered configurations of the oxide/metal/oxide type.

1.5 Modeling light absorption in thin film cells with a planar architecture

Thin film solar cells typically consist of a group of layers sequentially deposited one on top of the other and having a thickness in the range of tens to hundreds of nanometers. The photocurrent that can be provided by the solar cell is mainly determined by the absorber or active layer that generates most of the charges collected by the electrodes. However, interference between the incident and reflected waves inside such layered device also plays a determining role in the absorption intensity distribution profile, thus affecting the cell generated photocurrent. Such reflected wave arises mainly from the back metallic electrode but also from the other interfaces present in such planar layered device. An effective way to determine the optimal cell architecture is by implementing an inverse integration approach where photocurrent from each one of a large set of possible configuration solutions is numerically computed using a transfer matrix formalism (TMM).

A standard procedure to find the optimal solution for a photovoltaic problem would consist in taking the parameters that define a given cell structure and calculating the output photocurrent derived from it, in other words, the logic flow goes from the cause to the result. Subsequently, one would adjust such parame-

ters to eventually find the optimal solution. In inverse problem solving, a target solution is set as the starting point without any pre-setting of the parameters that define the cell structure. In photovoltaic type problems, that target solution would typically be the one that maximizes the photocurrent of the solar cell or its power conversion efficiency. In other cases, for instance in semi-transparent cells, this target could be one that offers the optimal balance between efficiency and transparency. Once that target solution is defined there are several numerical methods that may be implemented to find the parameters that define the cell configuration capable to provide the performance that one has set as target. A very effective procedure in solving problems that do not require a large discretization of the space, such as for instance in 1-dimensional configurations, is to numerically compute the targeted variable for a large set of configurations encompassing all possible cell architectures that make sense given the physical restrictions that may apply. For instance, when trying to determine which one is the optimal active layer thickness, large values for that thickness that imply a low FF for the cell should be excluded. In this thesis we implemented this procedure by computing the performance of a large set of configurations corresponding to a large set of different input parameters, including thicknesses and/or optical constants for some or all the device layers. Such parameters were allowed to vary within a specified range. Each configuration is unique and represent a possible solution. Once all such solutions are computed one may implement simple different procedures to select the configuration that leads to the solution that is closest to the target initially defined.

To implement the TMM model, it is assumed that:

1. All layers are considered homogeneous and isotropic, such that their optical characteristics can be represented by scalar complex indexes of refraction.

2. Interfaces between adjacent layers are parallel and optically flat.

3. Incident light is perpendicular to the stack and can be described by plane waves. With respect to the angle of incidence, different authors have studied the dependence of the photocurrent with varying angles of incidence in organic single, tandem solar cells and PVK solar cells, finding a weak dependence once the illumination area is corrected [143, 144, 145]. For this reason, in all our calculations we consider only the case of perpendicular incidence.
4. The efficiency of exciton diffusion, the efficiency of charge separation, and the efficiency of carriers transport and carriers collection, are not dependent on wavelength [92].

For every layer, the complex index of refraction $\tilde{n}$ must be known:

$$\tilde{n} = n + ik \tag{1.4}$$

where n is the refractive index and k is the extinction coefficient. The chosen propagation direction is along the z axis. The wavenumber of the l layer in the direction of propagation z is denoted as $k_{z,l}$ and is related to $\tilde{n}$ by the following equation:

$$k_{z,l} = \frac{2\pi\tilde{n}}{\lambda} \tag{1.5}$$

The numerical computation of the optical electrical fields must be performed backwards, starting from the interface between the air and the last layer of the device stack, which is typically a 100 nm thick silver layer, and finishing at the glass substrate interface. Boundary conditions are as shown in Figure 1.8, where the forward optical electrical field E_F^+ of the last layer (Air) is set to 1 and the backward optical electrical field E_F^- is equal to zero, provided no light is entering from the right hand side of the structure. For the rest of the layers, there exist a superposition of a forward and backward optical electric field components. To

propagate the fields from right to left, continuity conditions for the tangential component of the optical electrical field and the normal component of the optical magnetic field are considered at the interfaces.

The forward and backward optical electrical field amplitudes for a given layer $l-1$ can be calculated in a sequential manner from the components of the subsequent layer l using the following equation:

$$\begin{bmatrix} E_{l-1}^{+} \\ E_{l-1}^{-} \end{bmatrix} = \begin{bmatrix} A & B \\ C & D \end{bmatrix} \begin{bmatrix} E_{l}^{+} \\ E_{l}^{-} \end{bmatrix} \tag{1.6}$$

where the 2-dimension matrix elements are given in terms of the complex wavenumber of the l layer $k_{z,l}$, and the complex wavenumber and thickness of the $l-1$ layer, $k_{z,l-1}$ and d_{l-1}, respectively:

$$\begin{bmatrix} A & B \\ C & D \end{bmatrix} = \begin{bmatrix} (k_{z,l-1}+k_{z,l})e^{-ik_{z,l-1}d_{l-1}} & (k_{z,l-1}-k_{z,l})e^{-ik_{z,l-1}d_{l-1}} \\ (k_{z,l-1}-k_{z,l})e^{ik_{z,l-1}d_{l-1}} & (k_{z,l-1}+k_{z,l})e^{ik_{z,l-1}d_{l-1}} \end{bmatrix} \tag{1.7}$$

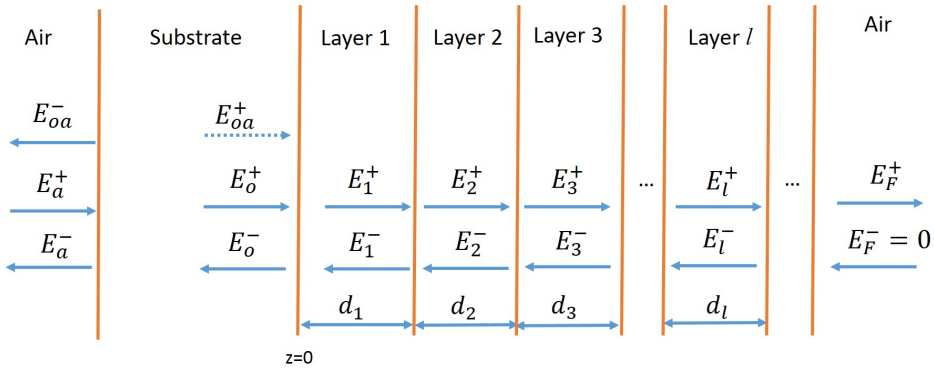

Figure 1.8: Scheme of an organic solar cell as a multilayer optical stack.

From the optical electrical field amplitudes in the glass substrate E_o^+ and E_o^- one can obtain their corresponding intensities $|E_o^+|^2$ and $|E_o^-|^2$, respectively. Given that the substrate is normally a 1 or 2 mm thick piece of glass, the superposition of E_o^+ and E_o^- is likely to be non-coherent. Therefore, it is assumed correct to relate E_o^+ and E_o^- to the incident field E_a^+ using the intensity Fresnel equations. At the interface between the air and the substrate, one must also consider the field that is reflected back to the device, denoted as E_{oa}^- to fulfill the energy conservation condition.

To determine the absorbed energy within the active layer(s), we start with:

$$Re\left\{-\frac{1}{2}\int_V(\vec{E}\cdot\vec{J}_d^*)dV=-\frac{1}{2}\int_S(\vec{E}\times\vec{H}^*)d\vec{S}\right\} \tag{1.8}$$

where both sides of the equation represent a decrease in the electromagnetic energy due to absorption [146]. On the left side of the equation, $\vec{J}_d^*$ can be written in terms of $\vec{E}$ as follows:

$$\vec{J}_d^*=\frac{\partial\vec{D}^*}{\partial t}=(-iw\epsilon\vec{E})^* \tag{1.9}$$

being ϵ the complex dielectric function where $\epsilon=\epsilon^{'}+i\epsilon^{''}$. Expressing ϵ in terms of n and k and inserting equation 1.9 in the left side of equation 1.8:

$$-\frac{iw\epsilon^*}{2}\int_V(\vec{E}\cdot\vec{E^*})dV=-\frac{2\pi c}{2\lambda}(i(n^2-k^2)+2nk)\epsilon_0\int|E(\vec{z})|^2dV \tag{1.10}$$

The real part of equation 1.10 can be written as:

$$\frac{2\pi cnk\epsilon_0}{\lambda}\int|E(\vec{z})|^2Adz \tag{1.11}$$

where the volume dV is expressed by an area A multiplied by dz.

To calculate the integral in equation 1.11 we discretize the thickness of the layer(s) into a given number of steps. The discretization integer to label each of such steps is m. The number of steps is selected according to the computation time and the thickness of the active layer, being higher when thicker films are being considered. Using the wavelength dependent optical electrical field intensity in a given interval of the discretization centered at position z_m, we calculate the absorbed energy in layer l:

$$E_A(z_m) = \frac{2\pi cnk\epsilon_0}{\lambda} \sum_{m=1}^{M} |E_l(\vec{z_m})|^2 \Delta z_m A \tag{1.12}$$

where c is the light velocity in vacuum, ϵ_0 is the permittivity of free space, and

$$\left|\vec{E_l}(z_m)\right|^2 = \left|\vec{E^+}_l(z_m) + \vec{E^-}_l(z_m)\right|^2 \tag{1.13}$$

By performing the discretized integration of the absorbed energy $E_A(z_m)$ over the complete active layer thickness and normalizing against the intensity of the incident optical electrical field, we obtain the normalized wavelength dependent absorption $A(\lambda)$. The $EQE(\lambda)$ is determined using equation 1.3. Finally, the short-circuit current density generated by the solar cell can be determined by integrating the $EQE(\lambda)$ over the solar spectra according to:

$$J_{sc} = q \int EQE(\lambda) F(\lambda) d\lambda \tag{1.14}$$

where q stands for the electron charge and $F(\lambda)$ is the sunlight photon flux under AM1.5G conditions.

1.6 Thesis outline

In this thesis, we aim for an optimal light harvesting within multi-junction solar cells to increase the performance of single-junction thin film solar cells. Specific objectives within the work include:

1. To design and develop homo-tandem and homo-triple structures based in organic solar cells
2. To design and develop homo-tandem structures in a 4-terminal configuration, allowing for an independent characterization of the organic sub-cells
3. To propose and theoretically evaluate a new hetero-multi-junction scheme based on PVK and CIGS with the added advantage of not requiring current matching
4. To evaluate different type of semi-transparent electrodes to be implemented within the multi-junction structures

In general, we investigate both homo and hetero-tandem structures. In the former structure, we increase the total thickness of the absorber material being used in the device without increasing the thickness of either single active material sublayer while, in the latter, we combine complementary absorbers to cover a wider portion of the solar spectra. In either structure, we must find the optimal electromagnetic field distribution within a complicated multilayer cell structure containing multiple absorbers. To achieve this, we implement an inverse integration approach combined with a transfer matrix calculation of the electric field. In addition, we develop different types of charge collection or recombination layers to be placed in between two adjacent sub-cells which we apply to tandem, triple, 4-terminal and series-parallel configurations.

The thesis is organized into five chapters. Chapter 1 introduces concepts required for the development of the thesis work including the optical model.

Chapter 2 describes the development of homo-multi-junction organic solar cells comprising homo-tandem and homo-triple devices with the blend PTB7:$PC_{71}BM$. This chapter gives insights into the role of optical optimization in achieving the current-matching required in such structures. A description of the optical interconnecting layer (ICL) used in both architectures is introduced as well as potential applications of the multi-junction structures. We report experimental results that confirm the improvement of the homo-tandem structure over the single junction devices, and the applicability of homo-triple devices to drive a water splitting reaction with a remarkable solar-to-hydrogen efficiency of 6%.

In Chapter 3, we explore the 4-terminal architecture using blends based on PTB7:$PC_{71}BM$ and PTB7-Th:$PC_{71}BM$. In this chapter, an in-depth study of different variants of the 4-terminal architecture are discussed, including the role of the semi-transparent electrodes and the intermediate dielectric. By using optical simulations, we determine the optimal architectures for photocurrent enhancement, considering both current-matched devices, or completely independent devices. With this type of architecture, we are able to corroborate the simulated and measured EQE of the individual sub-cells. We show that, with a proper selection and optimization of the inner electrodes in the 4-terminal structure, an improvement in photocurrent over the single junction device can be achieved.

Chapter 4 extends our study of multi-junction structures to Perovskites and CIGS solar cells. In this chapter, we describe a new configuration that has the advantages of being monolithic but does not require current-matching between the CIGS and PVK. Using realistic parameters for all the layers in the multi-junction architecture, we predict power conversion efficiencies of close to 28%, which is higher than any of the single junction sub-cells and the conventional tandem architecture.

Finally, Chapter 5 details experimental and theoretical work towards the solution of a common problem throughout this thesis, namely, the development of high quality transparent electrodes to be deposited on top of the solar cells. Different alternatives are studied, for instance, the use of ultrathin metallic layers combined with a microgrid, solution-processed AgNWs and standard evaporated metallic layers. We discuss the advantages and disadvantages of each solution and choose evaporation of metallic films for our solar cells. Results from upscaling experiments are also shown for the selected technology.

Chapter 2

Optical Management in Tandem and Triple OSC

Owing to the relatively modest carrier mobilities inherent to organic semiconductors (10^{-3} to 10^{-5} cm^2/Vs), the thicknesses of polymer-fullerene active layers are typically limited to the range between 100 and 130 nm. As these active layers are too thin to absorb all the incident light from the solar spectra, additional active layers of the same material can be serially connected in a multi-junction stack to mimic a single thick layer. Considering the ideal case of optical lossless ICLs, the number of active layers in a stack would be limited by the sub-cell receiving the least amount of light.

There have been a number of reports where homo-tandem configurations outperform single junction solar cells using different band-gap polymers. Examples include the 1.38 eV band-gap system PDTP-DFBT:$PC_{71}BM$ [126], where two inverted cells are interconnected through a MoO_3/modified PEDOT:PSS/ZnO ICL. A similar ICL, which omits the MoO_3 layer, is used by Bahro et al. in a tandem device with the 1.6 eV band-gap PTB7:$PC_{71}BM$ [127]. In contrast to the previous works, a tandem structure presented by Kang et al. [128] uses only a sin-

gle PEDOT:PSS recombination interlayer without the n-type metal oxide. This, in combination with a PTB7-Th:$PC_{71}BM$ blend modified with PEI, leads to an efficiency as high as 10.8%. Other reports have explored the complete removal of PEDOT:PSS from the ICL, given that its acidic and hygroscopic characteristics have been shown to reduce device stability. The work by Lu et al., for example, proposes an ICL formed of MoO_x/dipole layer/TiO_2. Insertion of such a dipole layer modifies the work function of the MoO_x preventing the S-shape typically encountered for ICLs featuring only MoO_x/TiO_2. Implementation of such an ICL between two sub-cells of PBDTTT-C-T:$PC_{70}BM$ results in a 15% improvement of the homo-tandem over the single device [147].

An interesting application for multi-junction organic solar cells is electrochemical water splitting. The necessary potential for water splitting typically varies between 1.4 - 1.9V and is strongly dependent on the type of electrodes, the electrolyte and the current density [148]. The organic blends that nowadays exhibit the highest V_{oc} together with a high FF are fullerene-free blends. They can reach a V_{oc} as high as 1.1 V [22]. Such a remarkable value for polymers is, however, below the required electrolysis potential. In their early work, Esiner et al. presented a triple-junction device composed of a front sub-cell of a wide band-gap polymer (PF10TBT, E.g. = 1.95 eV) followed by a middle and a rear sub-cell each with a small band-gap polymer (PDPPTPT, E.g. = 1.53 eV), using PCBM as electron acceptor in all cases [149]. With such a configuration, a device of 5.2% efficiency and 3.1% solar-to-hydrogen (STH) conversion efficiency was achieved. More recent work from the same group shows another photovoltaic-electrochemical system (PV-EC) based on an organic triple-junction device that reaches an STH efficiency of 5.4% [148].

In this chapter, we show the design and implementation of a current-matched homo-tandem using PTB7:$PC_{71}BM$. Combining a novel ICL with the optical optimization of the structure, we demonstrate an improvement of 12% over the single device. Successively, we extend the concept to a homo-triple-junction employing the same blend and ICL as the homo-tandem. Even though optical losses within the ICL prevent the efficiency of the triple device overtaking that of the single reference, it achieves a remarkably high FF of 76%. Such a FF sets the V_{mpp} very close to the thermodynamic water splitting potential threshold, thus minimizing electrical power losses. This allows a 6% STH efficiency in the production of hydrogen at neutral pH.

2.1 Multi-junction devices employing the same active material

Having multi-junction solar cells with two or three sub-cells based on the same active material has proven effective in overcoming the low absorption of the thin film OSC. To illustrate this, we consider in Figure 2.1 a comparison between the absorptance of a single PTB7:$PC_{71}BM$ based solar cell with different active layer thicknesses versus the absorptance of a tandem solar cell.

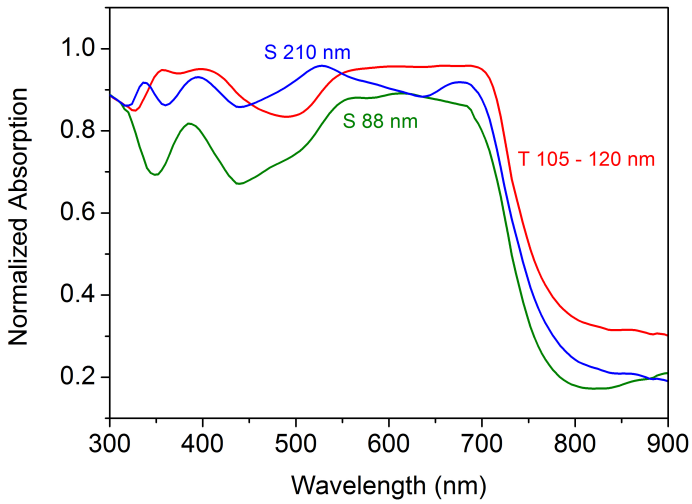

Figure 2.1: Absorptance of single junction solar cells of PTB7:$PC_{71}BM$ compared to the tandem structure.

In particular, the case of 88 nm thick and 210 nm thick PTB7:$PC_{71}BM$ single cells is shown, together with a tandem solar cell with a total blend thickness of 225 nm. Although the tandem device and the thick layer single junction device show similar absorptance, the thick layer single junction solar cell will perform poorly compared to the tandem because of charge transport limitations.

Experimentally, such a layer thickness introduces a significant loss in the FF, as is depicted in Figure 2.2. A tandem device with an optimized combination of two layers with a thickness of around 100 nm each guarantees that no electrical losses will occur. This demonstrates that the use of homo multi-junction structures is also meaningful when pushing towards higher efficiencies.

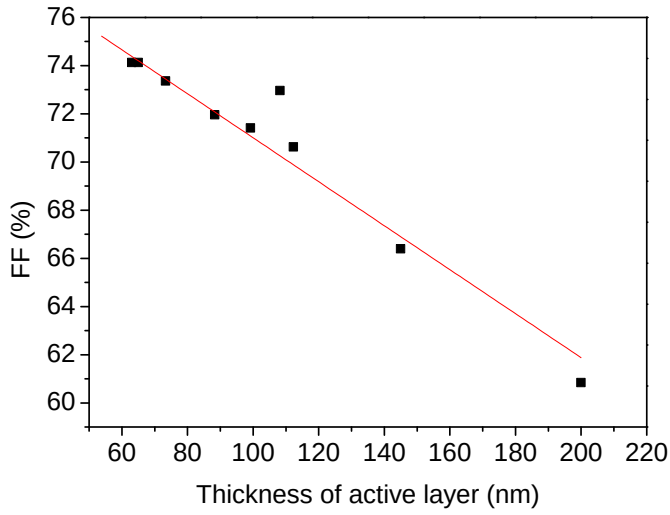

Figure 2.2: Fill Factor of the PTB7:$PC_{71}BM$ depending on layer thickness.

2.2 Achieving current-matching and enhanced efficiency in multi-junction structures

The light propagation through the multi-junction architectures was studied applying a transfer matrix method (TMM). An inverse integration approach was used to determine the optimal cell configuration given a set of physical parameters that define a solar cell architecture. Such inverse integration relies on selecting the configuration that maximizes the photocurrent of the tandem or triple cell

with the added constraint of matching the individual photocurrents generated by each cell within the stack. To perform these calculations one must know the complex index of refraction and thickness for each layer in the architecture. A large set of possible solutions is obtained using input parameters that include a range of thicknesses and/or optical constants for some of the layers. Using the calculated electric field intensities for each sub-cell, together with their optical constants, the absorption is computed to finally determine the short-circuit current density generated by each sub-cell. Further information about the optical modeling is found in section 1.5. The refractive indexes of the active materials are the ones presented in [150] and for the rest of the layers they are taken from [151] (see Appendix A for tabulated values). The thickness ranges were always in accordance with the experimental constraints to obtain optimal FF or V_{oc} for the sub-cells. In Figure 2.3 the layers composing the homo-tandem architecture are shown.

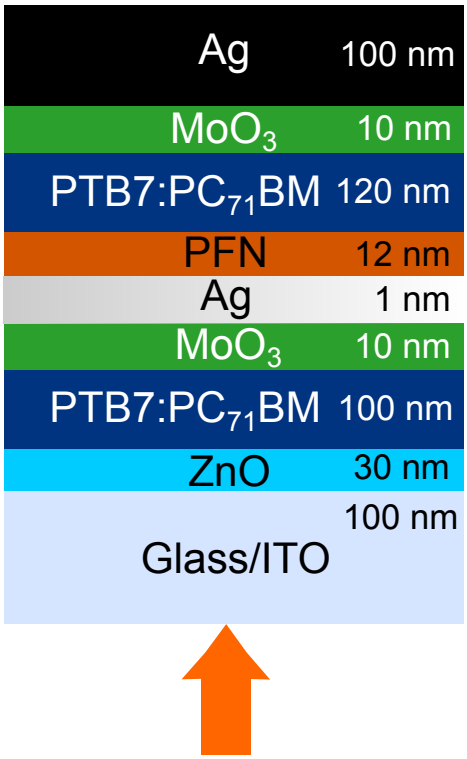

Figure 2.3: Scheme of the PTB7:PC_{71}BM tandem solar cell with optimal layer thicknesses.

Figure 2.4 shows the calculated short-circuit current density map of the homo-tandem solar cell when varying the thicknesses of the PTB7:PC_{71}BM active layers in the rear and front sub-cells. All the thicknesses of the other constituent layers are kept constant. As observed in such a current map, having a front sub-cell with a thickness of between 80 nm and 110 nm in combination with a rear sub-cell with a thickness of between 90 nm to 130 nm results in the highest values for the current density. On the other hand, lower current values arise when the front sub-cell thickness exceeds 110 nm, because the rear sub-cell current becomes a significant limiting factor. In other cases as well, for instance when the two sub-cells are below 90 nm, the current maintains low values. The tendency observed

in Fig 2.4 shows that the current maxima can even be found for thicker rear cells, above 130 nm, but these cases are not desirable from the electrical point of view because of the lower performance of solar cells with increasing thickness. For this reason, we keep the rear sub-cell thickness in our devices below 120 nm. Even if they are not in the highest current region, we achieve 7.6 mA/cm^2 for our best device as shown in Table 2.1, close to the highest value according to our simulations.

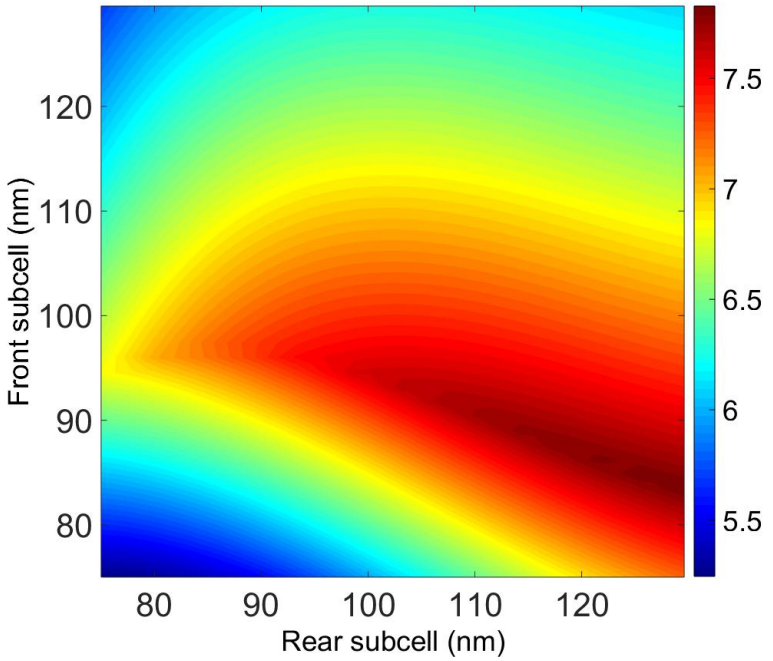

Figure 2.4: Simulated short-circuit current density generated in a tandem solar cell device as a function of the front and rear active layers.

The proposed homo-triple device is an extended version of the homo-tandem. The structure is composed of 13 layers, as seen in Figure 2.5, in which three cells of PTB7:PC$_{71}$BM are inherently connected in series to add up their voltages employing the same ICL developed for the homo-tandem devices.

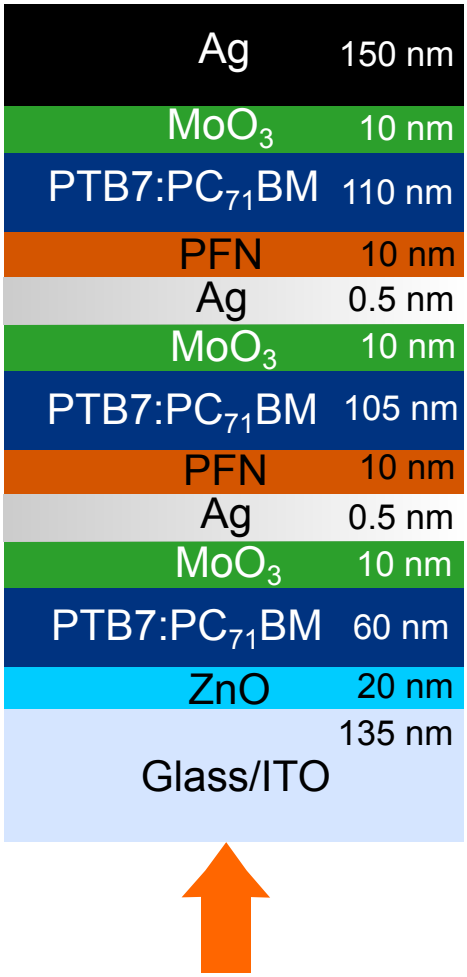

Figure 2.5: Scheme of triple junction solar cell based on PTB7:$PC_{71}BM$ with optimal layer thicknesses.

In the case of this complex architecture, optical optimization is also crucial in order to target a solution where the highest possible photocurrent is reached combined with a perfect match of the sub-cells photocurrent. The optimal optical electrical field intensity profile and simulated EQEs for each one of the sub-cells in the triple junction device is shown in Figures 2.6 and 2.7, respectively. The

optical electric field intensity shows maxima in the rear sub-cell for the near-infrared wavelengths, in the middle sub-cell for the wavelength range between 500 and 600 nm, and in the front sub-cell for the near UV range (Figure 2.6). The observed field distribution implies that absorption at shorter wavelengths is dominated by the front sub-cell, in the middle range of the visible spectrum by the middle sub-cell, and at the near-infrared by the rear sub-cell.

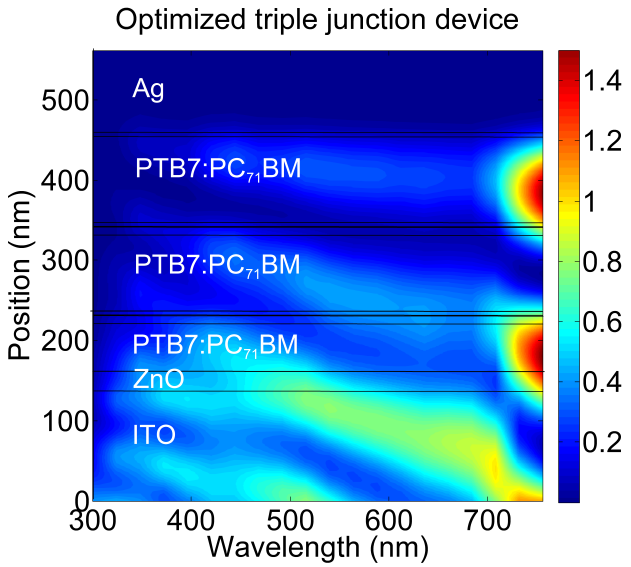

Figure 2.6: Calculated optical electrical field intensity normalized with respect to the incident field intensity as a function of wavelength for an optimized triple junction organic solar cell architecture.

Such perfectly balanced light absorption distribution among the three cells is better seen in the simulated EQEs shown in Figure 2.7. The large differences in the EQE can be explained in part by the different thicknesses of the layers, but are also due to the interference. As can be seen in Figure 2.6, constructive interference of the incident and reflected waves tends to favor IR shifted absorption for the

rear cell and UV shifted absorption for the front cell. In one of the architectures leading to such optimal light absorption, the PTB7:$PC_{71}BM$ layer thicknesses were determined to be 60, 105, and 110 nm for the front, middle, and rear sub-cells, respectively. These values were used to fabricate triple-junction devices with measured power conversion efficiencies of up to 8.7% under AM 1.5G illumination at 100 mW/cm^2 and V_{oc} equivalent to 2.1 V.

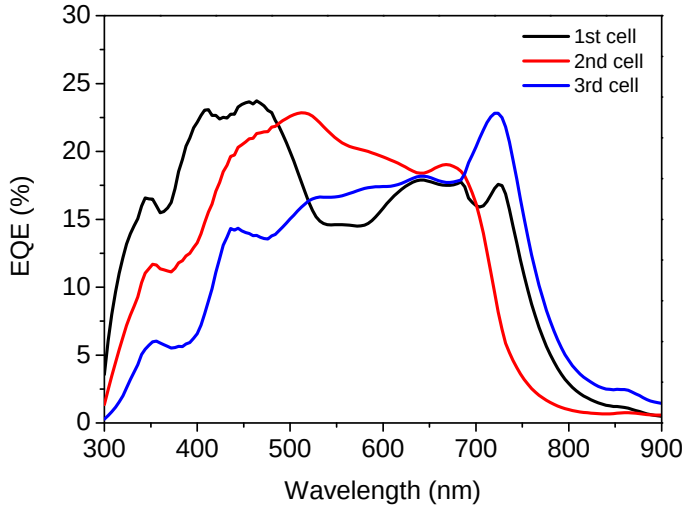

Figure 2.7: Calculated EQE for each one of the three sub-cells in an optimized architecture.

2.3 Ultrathin interconnecting layer for homo-tandem OSC

Homo-tandem devices were fabricated using two sub-cells with the blend PTB7:$PC_{71}BM$ as shown in Figure 2.3. The cells were sequentially deposited on top of an ITO transparent electrode. We employed a MoO_3/Ag/PFN ICL,

less than 20 nm thick, to connect the two identical inverted PTB7:$PC_{71}BM$ sub-cells in series. The more commonly used PEDOT and ZnO ICL materials need thermal treatments, which, despite efforts to decrease their temperature, may still be detrimental to the bottom organic layers. In this homo-tandem device architecture, we employed thin layers of thermally evaporated MoO_3 and the conjugated polyelectrolyte poly[9,9-bis(30- (N,N-dimethylamino)propyl)-2,7-fluorene]-alt-2,7-(9,9-dioctyl-fluorene)] (PFN) that can be deposited from solution without any further treatment. A thin Ag layer was evaporated between those two layers in order to favour charge recombination. The transfer matrix-based numerical determination of light absorption using the indicated materials predicts a 14% increase in J_{sc} for the same polymer tandem cells relative to the optimal single-junction cell.

We investigated the photovoltaic performance of single junction inverted PTB7:$PC_{71}BM$ OSC with two different configurations, single with ZnO: glass/ITO/ZnO/PTB7:$PC_{71}BM$/MoO_3/Ag and single with PFN: glass/ ITO/PFN/PTB7:$PC_{71}BM$/MoO_3/Ag. The single junction device with ZnO yields a V_{oc} of 0.74 V, a J_{sc} of 14.3 mA/cm^2 and an FF of 69%, resulting in a PCE of 7.3% for a blend thickness of ca. 100 nm and a ZnO thickness of 35 nm. The same PCE could be obtained with a V_{oc} of 0.72 V, a J_{sc} of 14.3 mA/cm^2 and a FF of 71% for a blend thickness of ca. 100 nm and a PFN thickness of 12 nm. The blend composed of PTB7:$PC_{71}BM$ dissolved in chlorobenzene (CB) was deposited inside a glovebox to obtain a thickness of ca. 100 nm in both cases. After a vacuum-drying period, the top electrode was evaporated on both devices, composed of 3 nm of MoO_3 followed by 100 nm of Ag. After fabrication, all measurements were carried out in air without encapsulation and showed very similar results for both inverted structures.

The tandem architecture was formed by the layers (in nm) ITO(100)/ ZnO(30)/ PTB7:$PC_{71}BM$(100) /MoO_3 (10)/ Ag(1)/PFN(12)/ PTB7:$PC_{71}BM$(120)/ MoO_3(10)/Ag(150), where the thicknesses of the layers were measured using an AFM. The JV curve for the tandem solar cell is depicted in Figure 2.8 and device performances are summarized in Table 2.1 for the best devices. The standard deviation in the PCE was low for all cases, with a $\pm$ 0.2%. To compare directly the tandem and single devices, we have added an additional parameter which is the J_{sc} multiplied by the V_{oc} equivalent to the maximum power P_{max} normalized to the V_{oc} of the single device. From the data obtained, it can be observed that there is an improvement close to 6% in the FF of the tandem relative to the single with ZnO and another 6.15% of enhancement derived exclusively from an absorption increase. Adding up the two effects, the tandem device has an efficiency that overperforms the single by 12%.

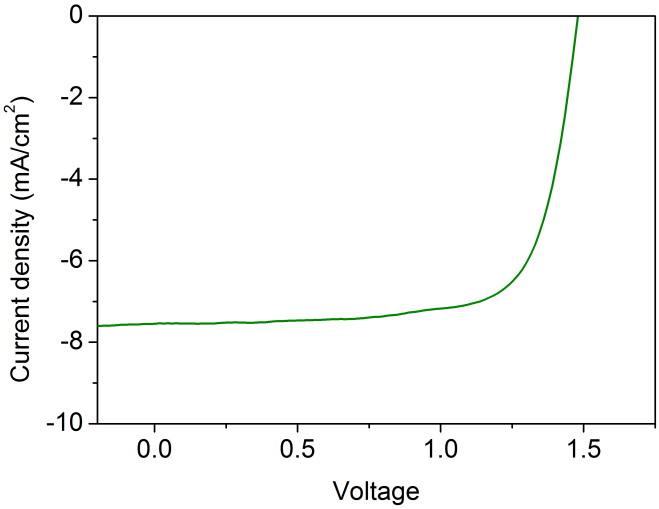

Figure 2.8: JV curve of PTB7:$PC_{71}BM$ tandem solar cell.

Table 2.1: Performance parameters of the single junction devices and tandem devices.

Device	J_{sc} $[mA/cm^2]$	V_{oc} $[mV]$	FF [%]	PCE [%]	$P_{max}/V_{oc\ single}$ $[mA/cm^2]$
Single ZnO	14.3	741	69	7.3	14.3
Single PFN	14.3	723	71	7.3	14.3
Tandem	7.6	1480	73	8.2	15.2
% change	-	-	+5.79%	+12%	+6.15%

2.4 Homo-triple OSC for water splitting

Developing a homo-triple organic solar cell can be useful for applications where it is important to have a high voltage. For instance, the open circuit voltage of a single junction OSC is not sufficient to overcome the potential barrier for the water splitting chemical reaction. In order to achieve a V_{oc} of 2.1 V, we piled up three single junction cells of the same PTB7:$PC_{71}BM$ blend, as seen in Figure 2.5. By using the same blend in the three sub-cells and the ICL previously optimized for the tandem case, we simplify the fabrication procedure while at the same time we ensure a homogeneous electrical performance throughout the device. This resulted in FF as high as 76%, significantly higher than the 71% averaged by the single junction counterparts. Such high FF are essential to minimize the impact of the overpotentials in the water splitting reaction. At the lowest measured water splitting voltage of 1.70 V, the STH conversion efficiency under 1 sun AM1.5G illumination is as high as 96% of the maximum efficiency possible, corresponding to an ideal operation at the thermodynamic potential threshold of 1.23 V. This is combined with the use of a platinum free anode and cathode electrodes immersed in a water solution buffered at pH 7. A glassy carbon rod with an extremely small

amount of RuO_2 catalyst anchored on the graphite surface was used as an anode (GC-RuO_2). The cathode was made of earth abundant materials deposited on a stainless steel plate (SST-NiMoZn). A scheme showing the complete PV-EC system is shown in Figure 2.9.

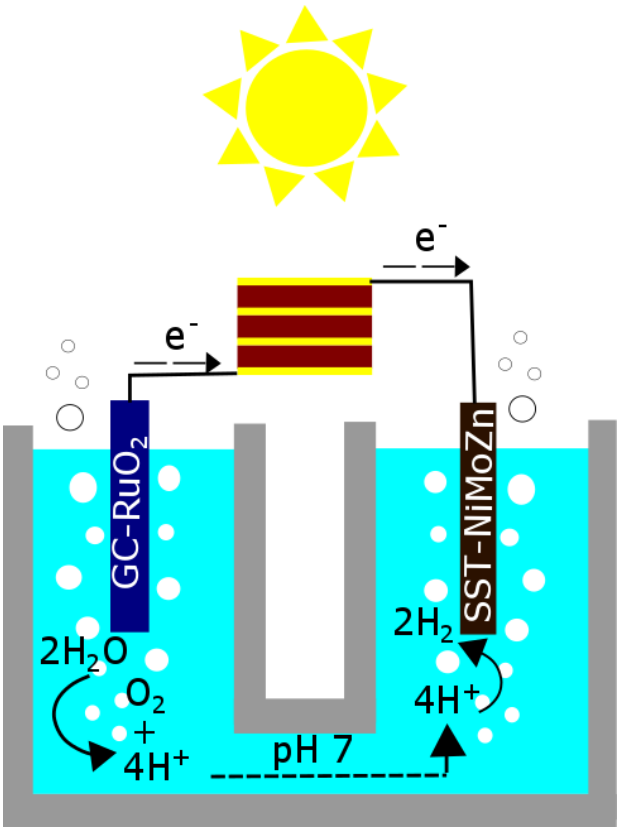

Figure 2.9: Schematic representation of the setup for the water splitting experiments using a triple junction organic solar cell, GC-RuO_2 anode, and SST-NiMoZn cathode.

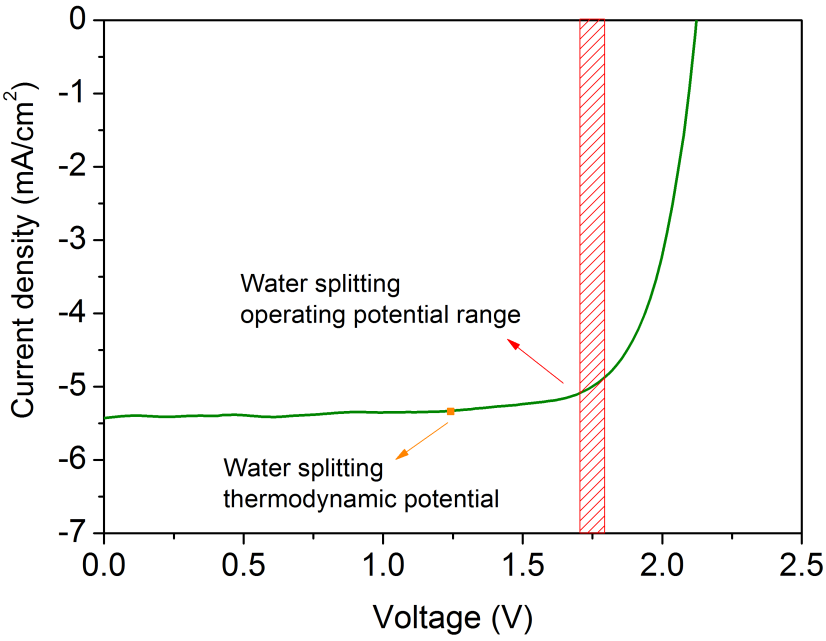

Figure 2.10: JV curve of triple junction cell. V_{oc} = 2.13 V, J_{sc} = 5.4 mA/ cm^2, FF = 76%, and PCE = 8.7% where the water splitting thermodynamic potential (orange) and water splitting operating potential range (red) are indicated.

A typical current density-voltage (JV) curve of the triple junction cell is shown in Figure 2.10, with its relevant parameters marked in red. The potential extracted at the maximum power point of the cell was close to 1.76 V, 530 mV higher than the thermodynamic potential for the water splitting reaction. As shown in Figure 2.11 using the full PV-EC system, continuous gas production was detected over a period of 5 h with faradaic efficiencies close to 100% for both gases and no apparent loss of activity.

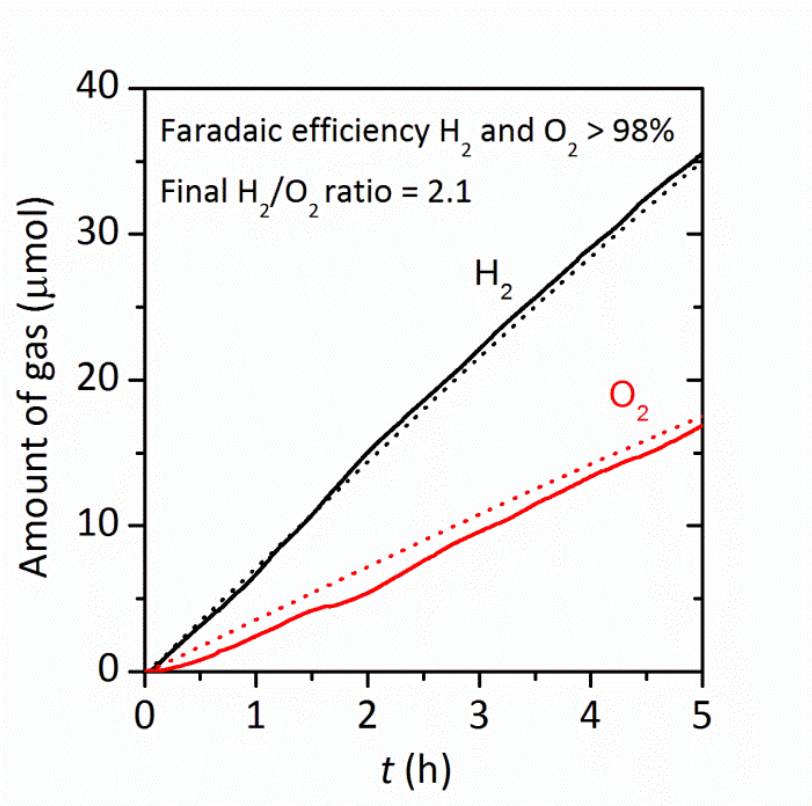

Figure 2.11: Gas evolution profile of a water splitting experiment using a triple junction solar cell, GC-RuO_2 anode and SST-NiMoZn cathode in a two electrode configuration and a two-compartment cell, containing 0.1M phosphate buffer, pH = 7, under 1 sun irradiation ($\lambda > 400$ nm). The dotted lines represent the 100% faradaic efficiency based on the charge passed during electrolysis while the solid lines represent the gas measured with Clark electrode sensor.

2.5 Conclusions

In this chapter, we have demonstrated that it is feasible to apply optical modelling to complex structures such as tandem and triple organic solar cells. In both structures, we used a thin and semitransparent interconnecting layer composed

of MoO_3, Ag and PFN. Such an ICL acted as an efficient recombination layer for the charges and from the processing point of view, it was completely innocuous to the bottom solar cells. We performed numerical calculations using the TMM combined with an inverse integration approach to design cell architectures exhibiting an optimal light absorption by the constituents' sub-cells and complying with the current-matching criteria. For the tandem devices, an overall improvement of 12% over the single device was obtained. On the one hand, the FF of the tandem was superior to the single references and on the other hand, by adjusting the thicknesses of the active layers we improved light harvesting over the single device corresponding to a 6% increase in P_{max} normalized to the V_{oc} of the single junction. Similarly, through optical simulations of the homo-triple organic solar cells we found the optimal architecture complying with current-matching. Following these guidelines, we experimentally fabricated a device able to provide a V_{oc} of 2.1V, with a high FF of 76% and matched photocurrent of 5.4 mA/cm^2, and we utilized it to drive a water splitting reaction. The high FF allowed a V_{mpp} that matched closely to the required water splitting electrochemical potential thus minimizing electrical losses. In other words, although water splitting is achieved at a potential which is 42% higher than the thermodynamic potential threshold, the current flowing through the electrochemical cell corresponds to 96% of the current that would be flowing through the cell if the water splitting reaction were to be occurring at 1.23V. Using the optimized triple-junction device, a remarkable STH efficiency conversion of 6% was achieved at neutral PH.

Chapter 3

4-Terminal Organic Solar Cells

Sub-cells in a standard tandem configuration must be current-matched to reach their optimum performance. Their serial connection requires an ICL where charges can recombine efficiently. Such an ICL must guarantee a low resistance connection that introduces no electrical potential loss. It has to be robust to protect the underlying layers from damage when processing the top sub-cells [131]. The interlayer must also be transparent to avoid optical losses. Additionally, the difficulty in testing the sub-cells independently makes the optimization of tandem cells a challenging task.

An alternative to tandem solar cells is the 4-terminal architecture. In this architecture, the sub-cells are not internally series-connected, thus being able to operate independently. The devices are in principle only optically coupled, such that the light that is transmitted through the front sub-cell reaches the back sub-cell. This architecture no longer needs an ICL or current-matching, and instead requires two additional transparent electrodes. Thus, the ICL fabrication complexity and the stringent current-matching criteria are removed but generally at the expense of an increased production cost. Despite this, 4-terminal devices have recently gained attention for the high efficiencies that they can achieve. The

improvement over standard tandem devices comes from the possibility of independently optimizing the stacked sub-cells to operate at their maximum power point. In the event that device properties or external factors vary over time, electrically uncoupled cells can still be tuned independently to readjust their operating points, delivering at all times maximum power from each sub-cell [129].

The work by Gehlhaar et al. presents results on 4-terminal modules based on complementary organic materials such as PV10 and XPbing compared to standard tandem devices [130]. They found that 4-terminal devices excel the energy output of a standard tandem device with the same organic absorber systems by more than 32% over a year considering central European solar irradiance conditions.

In this chapter, we report the design and fabrication of optically optimized 4-terminal devices in which two single junction sub-cells are fabricated using the same organic blend and are separated by a dielectric spacer. Different alternatives for the dielectric spacer and transparent electrodes are explored. Applying the inverse problem solving procedure considered in the previous chapter, we numerically designed device architectures to obtain an optimal PV performance. In these 4-terminal configurations, even when the two sub-cells use identical absorber materials, one may improve the light harvesting capacity of the best single device. In an experimental implementation of the 4-terminal device using the PTB7:$PC_{71}BM$ blend for both sub-cells, we find a very good match with the trend of the numerical predictions. Encouraged by these results, we fabricated 4-terminal configurations using PTB7-Th:$PC_{71}BM$, which for an optimized case showed an improvement in the overall photocurrent compared with the best single junction device.

3.1 4-Terminal devices with MAM as light entrance electrode

This architecture is fabricated by depositing each inverted sub-cell of PTB7:$PC_{71}BM$ on either side of a bi-coated ITO glass substrate as shown in Figure 3.1. In this configuration, the dielectric spacer is a 1.1 mm thick piece of glass where a patterned ITO is deposited on one side and a second non-patterned ITO is deposited by RF sputtering on the other side, to obtain a bi-coated ITO substrate. Two complete sub-cells are deposited on either side of the substrates, including the ZnO layers by sol-gel, the blends and the electrodes.

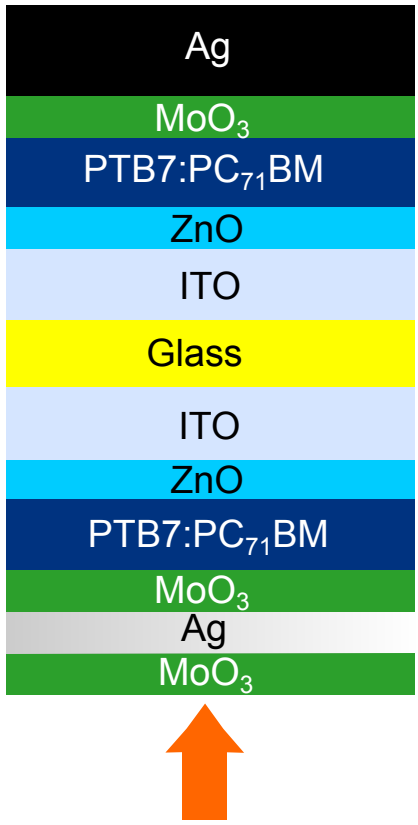

Figure 3.1: 4-Terminal architecture with MAM as light entrance electrode.

For the front sub-cell, the outer electrode is formed by a MAM structure while for the back sub-cell this electrode is a thick layer of Ag. The light enters into the structure through the front sub-cell while the back sub-cell is illuminated with the light not absorbed by the front cell.

An optimal light absorption by both sub-cells may be reached when the architecture of the entire device is optimized to enhance absorption in both active layers. In the event that both sub-cells were externally connected in a series configuration, the current flowing through both sub-cells would be the same. In accordance with this, we look for a solution such that both sub-cells provide the highest possible but the same short-circuit current (J_{sc}), similar to the case of the homo-tandem described in the previous chapter. In addition, to avoid any detrimental effect over the FF when a real device is fabricated, we ensure that the thicknesses for any of the two blend layers are not larger than 130 nm.

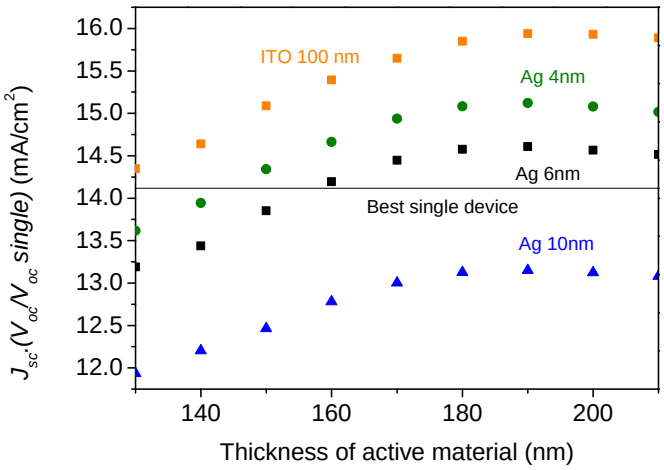

Figure 3.2: Calculated P_{max} normalized against the V_{oc} of a single device in terms of the total thickness of active material for the 4-terminal devices with varying Ag thickness in the MAM electrode.

Figure 3.2 represents the calculated P_{max} normalized against the V_{oc} of a single device in terms of the total thickness of active material for the 4-terminal devices when the Ag thickness in the MAM electrode is 10 nm (blue triangles), 6 nm (black squares), 4 nm (green circles), and the ITO is 100 nm (orange squares). The case of the best single device is shown in a straight line. In the graph, the P_{max} normalized to the single device V_{oc} is used in order to compare it with the two series connected cells that would exhibit a V_{oc} equivalent to the sum of the V_{oc} from two single junction cells. Using this parameter, it is possible to observe the improvement of the tandem structure over the single device, given that a straight forward comparison of the photocurrent densities of tandem and single devices would not clarify it.

We start our calculations from a total active layer thickness of 130 nm and continue up to 210 nm. The best result is to have a total blend thickness of 190

nm, distributed in a front sub-cell blend of 88 nm, 90 nm and 91 nm, together with a back sub-cell blend of 102 nm, 100 nm and 99 nm for Ag of 10 nm, 6 nm and 4 nm, respectively. For comparison, we also added the case where a highly transparent ITO electrode is used. The dielectric spacer and ZnO thicknesses also change depending on the thickness of the front silver electrode. The values for the best 4-terminal device are listed in Table 3.1.

Table 3.1: Layer thicknesses ranges (in nm) used in the numerical calculations and layer thicknesses for the optimal and fabricated 4-terminal device.

Layer	Range	Best device	Experiment
Total Active Layer (TAL)	130 - 210	190	180
MoO_3	Fixed at	39	39
Ag	4-6-10	4	10
MoO_3	fixed	3	3
PTB7:PC_{71}BM front (AL1)	70 - 100	91	90
ZnO	Fixed at	5	30
ITO	Fixed at	100	135
D. spacer	50 - 290	182	1100 μm
ITO	Fixed at	130	140
ZnO	5 - 30	8.75	30
PTB7:PC_{71}BM back (AL2)	TAL- AL1	99	90
MoO_3	Fixed at	3	3
Ag	Fixed at	100	100

The optimal P_{max} /V_{oc} single for the 4-terminal devices are strongly dependent on the front MAM electrode, exhibiting a very good performance when the silver layer in the MAM is thinned down to 4 nm.

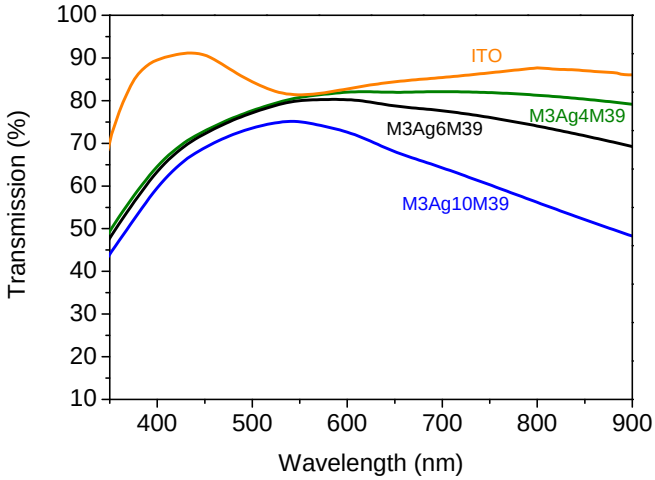

Figure 3.3: Modeled spectral transmission of MAM electrodes depending on the silver thickness.

In that event, as shown in Figure 3.3, the electrode transmission approaches that of 100 nm thick ITO for the longer wavelengths, where light absorption in PTB7:$PC_{71}BM$ is the largest.

Note that the 4 and 6 nm thick Ag electrodes of the serial connected 4-terminal devices considered exhibit an improvement over the best single junction case as observed in Figure 3.2. This improvement is directly an efficiency improvement. For the optimal 4 nm Ag MAM device, the calculated improvement relative to the best single junction reaches 7.1 %. Remarkably, such enhanced performance is obtained using the same blend in both sub-cells and, in a device configuration where the thickness for such layers is less than 100 nm, which would correspond to a high FF for both sub-cells.

The numerically calculated external quantum efficiencies (EQEs) for both

sub-cells are shown in Figure 3.4 for the optimal configuration when the thickness of the Ag layer in the MAM electrode is 4 nm. The complete stack (in nm) is MoO_3 (39)/ Ag (4)/ MoO_3 (3)/PTB7:$PC_{71}BM$ (91)/ZnO(5)/ITO(100)/ Dielectric spacer (182)/ITO(130)/ZnO (8.75)/ PTB7:$PC_{71}BM$ (99)/ MoO_3 (3)/ Ag (100). At long wavelengths above 650 nm, light absorption is larger in the back sub-cell while at the opposite range, for short wavelengths below 500 nm, light absorption is dominated by the front sub-cell. In the entire wavelength range, a local maximum in the EQE for the front sub-cell corresponds to a local minimum for the EQE in the back sub-cell and vice-versa. This kind of behavior is weakly dependent on the transparency of the light entrance electrode. In Figure 3.5 we show the EQEs for the optimal 4-terminal configuration when the thickness of the Ag electrode is 10 nm. The full structure is MoO_3 (39)/ Ag (10)/ MoO_3 (3)/PTB7:$PC_{71}BM$ (91)/ZnO(5)/ITO(100)/Dielectric spacer (182)/ITO(130) /ZnO (8.75)/ PTB7:$PC_{71}BM$ (99)/ MoO_3 (3)/ Ag (100) nm. Again, we observe that the EQE at long wavelengths is larger for the back sub-cell while at shorter wavelengths is larger for the front sub-cell.

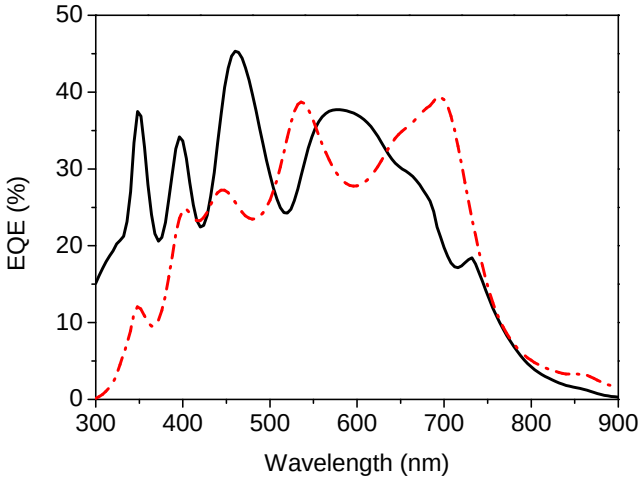

Figure 3.4: Numerically calculated EQE for the front sub-cell (black continuous line) and for the back sub-cell (dash-dotted line) for an optimized configuration.

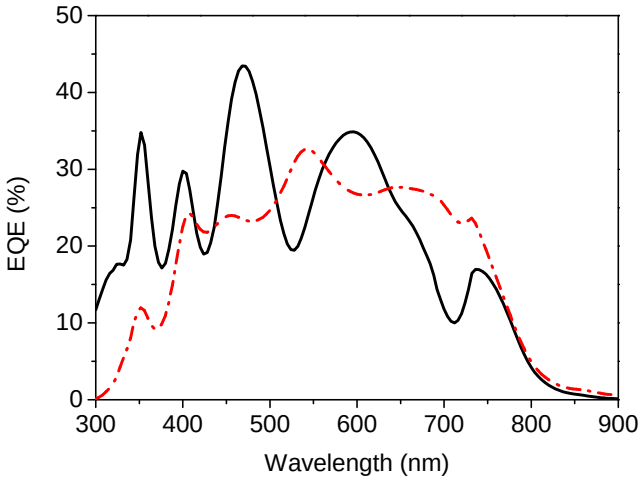

Figure 3.5: Numerically calculated EQE for the front sub-cell (black continuous line) and for the back sub-cell (dash-dotted line) for a configuration with 10 nm Ag.

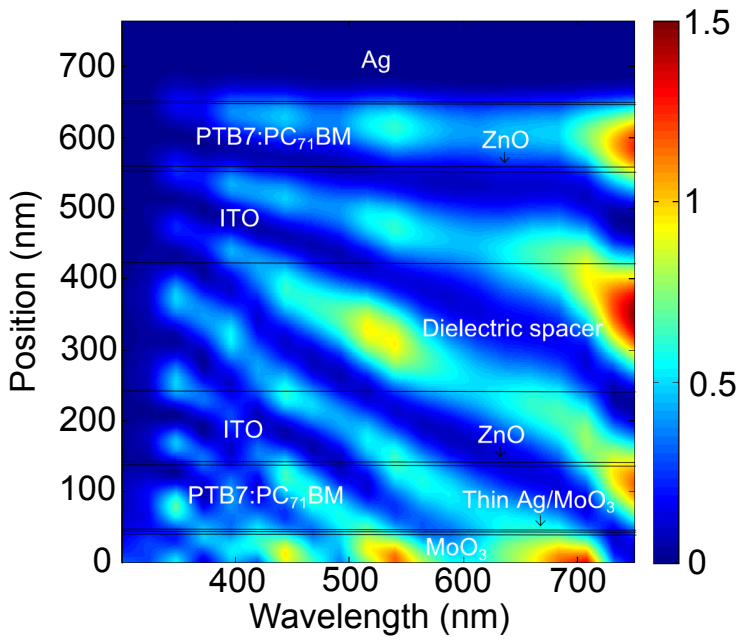

Figure 3.6: Numerically calculated optical electrical field intensity for the optimized 4-T architecture.

It is observed that the optical optimization of the multilayer structure disguises the spectral dependence on the active blend extinction coefficient leading to an EQE which is strongly linked to the optical electrical field distribution inside the solar cell. The normalized field intensity distribution map is shown in Figure 3.6 as a function of wavelength and position inside the solar cell for the optimal configuration. To enhance photon harvesting, the optical electrical field intensity must be maximized within the active layers inside the structure. As seen in Figure 3.6, such optical electrical field intensity is clearly enhanced within the back sub-cell active layer for most of the wavelength range. Because of material dispersion, this confinement of the largest field density within the active layer is not so apparent for the front sub-cell. However, when the cell architecture is

optimal, as in Figure 3.6, the minima in field intensity for the front cell are, to a certain degree, compensated with field intensity maxima in the back sub-cell.

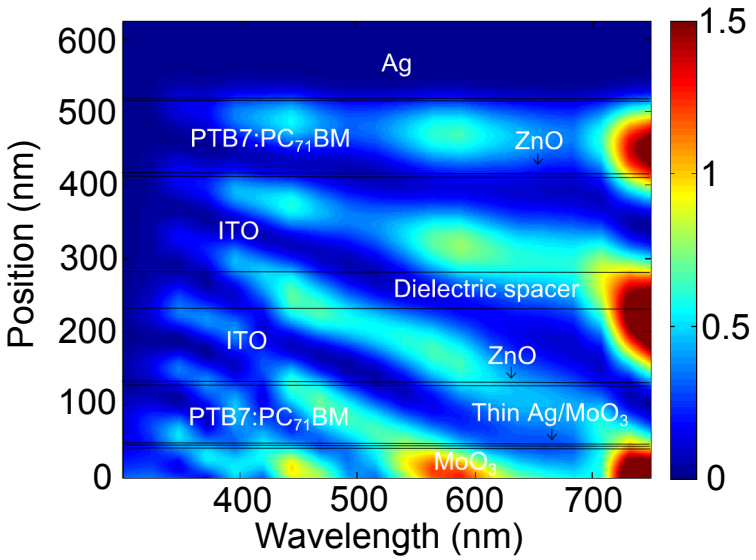

Figure 3.7: Numerically calculated optical electrical field intensity for a non-optimized 4-T architecture.

For comparison, in Figure 3.7 the field intensity distribution map is shown for a non-optimized configuration. Note that in this case, the field intensity in the active layer of the front sub-cell is weaker for the entire wavelength range being very apparent that the thickness of the active layer is thinner than it should be. This decrease in optical electrical field intensity translates into a reduced photocurrent for such a front sub-cell, thus limiting the total short-circuit current when a serial connected device is considered.

One of the advantages of the 4-terminal tandem configuration over the standard 2-terminal is that the performance of the two sub-cells can be studied independently from each other when already integrated in the entire device. The PV parameters from both sub-cells are given in Table 3.2.

Table 3.2: Solar cells parameters.

Cell	$J_{sc}[mA/cm^2]$	$V_{oc}[mV]$	$FF[\%]$	$PCE[\%]$
Front	6.36±0.28	0.703±0.007	62.42±2.46	2.79±0.13
Back	6.13±0.57	0.732±0.010	72.44±3.07	3.25±0.43
4T Series	6.13±0.53	1.439±0.007	69.19±3.14	6.10±0.42
Ratio of the 4T in series relative to single sub-cells	-	0.9979[a]	1.0392[b]	-

[a] The average of the sum of the front and back subcells V_{oc} in the 4-terminal devices is compared to the average of the measured V_{oc} for the serial connected cells.

[b] The average FF of the independent subcells is compared to the FF of the serial connected 4-terminal devices.

In terms of photocurrent generation, the implemented architecture achieves a rather good match, which is important when the cells are connected externally in a series configuration. The match of the voltages is also good, which is necessary when the cells are connected in parallel. On the other hand, we observe that the FF for the front cell is slightly worse than the one for the back cell, which may be attributed to the lower conductivity of the electrodes for the front cell when compared to the back thick silver electrode. The JV characteristic curve of the front and back cells measured independently and then externally connected in series are shown in Figure 3.8. We performed a statistical study to determine the average values for the J_{sc}, V_{oc} and FF of the series connected devices. As expected, the J_{sc} is limited to the smallest one of the two sub-cells, the V_{oc} is very close to twice the average V_{oc} for the single junction cells and the FF is slightly larger than the average FF for the single junction cells. In other

words, no degradation in the electrical performance is observed for the 4-terminal device when connected in series, relative to the single junction device.

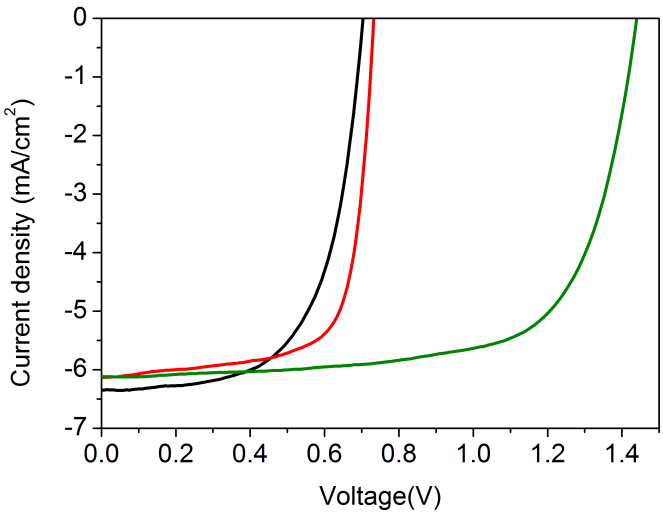

Figure 3.8: JV curves of front sub-cell (black), back sub-cell (red), and serial connected (green). The curves correspond to the best device.

The absorbing layers were fabricated following the same recipe in order to obtain thicknesses of around 90 nm for both sub-cells, which corresponds to the thicknesses predicted by the numerical modelling of the optimal configuration. At present, there are several experimental limitations that prevent the fabrication of the optimal device according to the results shown in Figure 3.4. These limitations include a lack of control at the nanoscale over the thickness of the dielectric spacer. Also, ultrathin metallic layers typically favor the formation of non-continuous or granular films with low conductivity causing the electrical properties of the MAM electrodes to degrade rapidly when the thicknesses below 10 nm are considered [140]. In addition to this, in some cases the optimal thickness for buffer layers extracted from the optical simulations cannot be obtained as, for instance, when

the ZnO layers is prepared by sol-gel. However, the fabricated device can be used to evaluate the performance and validate the 4-terminal architecture relative to the single junction device. The layer architecture of the entire fabricated device is given in Table 3.1.

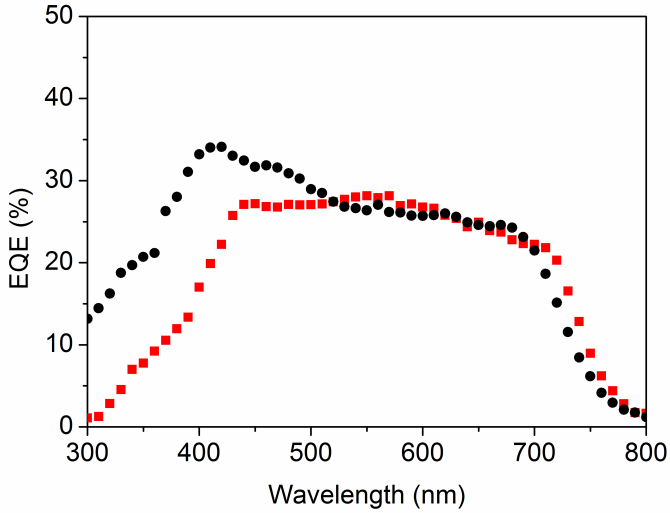

Figure 3.9: Measured EQE for the front sub-cell (black dots) and for the back sub-cell (red dots). Note that the large thickness of the dielectric spacer in between the two sub-cells eliminates the oscillatory behavior seen in the numerical prediction shown in Figure 3.5.

The experimentally measured EQEs for the front and back sub-cells are shown in Figure 3.9. Note that the interference-like pattern observed in Figures 3.4 and 3.5 is washed out because of the large thickness of the dielectric spacer, which is around 1 mm in the fabricated devices. However, the overall trend of the numerically optimized EQEs is maintained in the experimentally implemented devices. As seen in Figure 3.9, for wavelengths larger than 700 nm the EQE of the back sub-cell is large, while for wavelengths below 500 nm the EQE of the

front sub-cell dominates. In the region in between, the EQEs alternate.

3.2 4-terminal devices with ITO as light entrance electrode and Ag inner electrodes

In a second architecture, we complete a 4-terminal device built from bottom to top on one single side of the substrate using a transparent dielectric layer as observed in Figure 3.10.

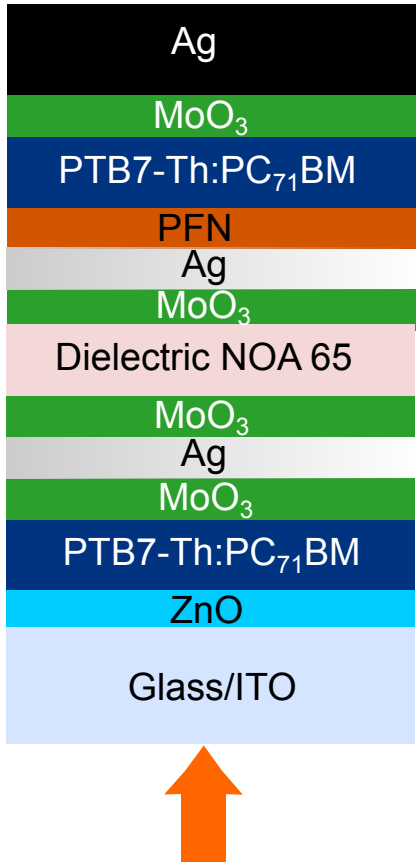

Figure 3.10: Fabricated 4-terminal architecture where light enters through an ITO electrode.

Within this 4-terminal device, the front sub-cell is a conventional semi-transparent inverted device on an ITO substrate and the back sub-cell is a less common inverted device that is built upon a thin silver layer. Theoretically, controlling the thickness of the dielectric layer as well as the thicknesses of the intermediate silver layers would lead to higher photocurrents. For this configuration, we relax the strict condition of current-matching applied for the previous 4-terminal architecture and we look for a solution that maximizes the power generated by the device. To reach this, we optimize the sum of the photocurrents, given that the V_{oc} and FF are practically the same for both active layers.

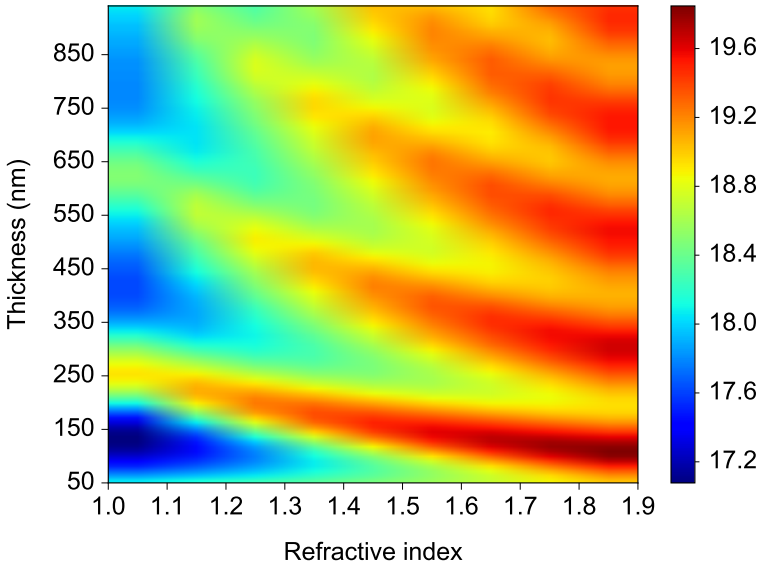

Figure 3.11: Sum of photocurrents J_{sc1} and J_{sc2} corresponding to back and front sub-cells respectively, using Ag indexes from Palik [151] and varying the refractive index and thickness of the dielectric layer.

The theoretical solutions shown in Figure 3.11 correspond to numerical cal-

culations performed for the 4-terminal device based on PTB7-Th:$PC_{71}BM$ using silver bulk constants taken from Palik (PTCCE for both cells is considered 0.9). In the simulated model, the experimentally used MoO_3 layers surrounding the dielectric as shown in Figure 3.10 are not included to consider only the effects of the dielectric. All the other layers within the stack, except for the dielectric layer, are kept constant and are listed in Table 3.3. Here, we study the effect of variations within the dielectric layer thickness and refractive index on the resultant sum of photocurrents, under the assumption of a non-absorbing dielectric layer. The graph clearly indicates that the probability of getting a higher photocurrent increases when using a thinner dielectric together with a higher refractive index. As the dielectric gets thicker, the chances of achieving higher photocurrents rely mostly on the possibility of using a material with high refractive index.

Table 3.3: Best configuration for 4-terminal device as simulated in Figure 3.11 using Palik's Ag index for the thin silver.

Layer	Thickness range [nm]	Best thick-ness [nm]	Best n	$J_{sc}[mA/cm^2]$
ITO	fixed	135	fixed	
ZnO	fixed	10	fixed	
PTB7-Th:$PC_{71}BM$	fixed	100	fixed	10.39
MoO_3	fixed	5	fixed	
Ag thin	fixed	7.5	fixed	
Dielectric layer	50-950	95	1.9	
Ag thin	fixed	7.5	fixed	
PFN	fixed	1	fixed	
PTB7-Th:$PC_{71}BM$	fixed	100	fixed	9.51
MoO_3	fixed	5	fixed	
Ag	fixed	150	fixed	
$J_{sc1} + J_{sc2}$				19.90

Note that, when performed with the bulk silver constants, the best 4-terminal configuration can theoretically surpass the best results for a single junction device based on ITO. As seen in Figure 3.12, the highest short circuit current calculated for a single inverted device of ITO/ZnO/PTB7-Th:$PC_{71}BM$/ MoO_3 /Ag is 16.65 mA/cm^2, while for the 4-terminal device the current can reach 19.90 mA/cm^2, which is equivalent to an improvement of almost 20%.

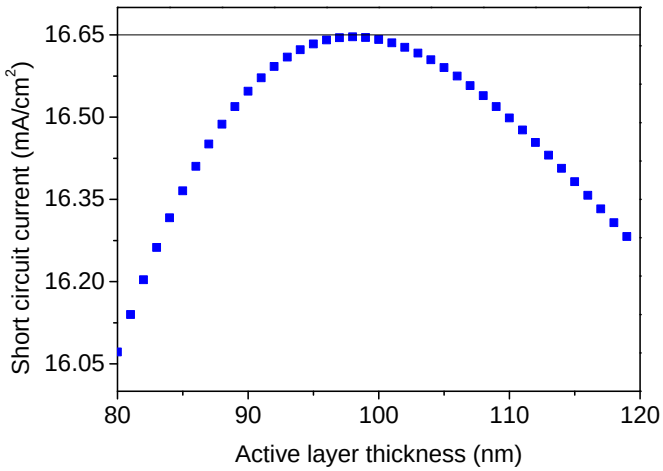

Figure 3.12: Short circuit current density for a single junction device based in PTB7-Th:$PC_{71}BM$ depending on the active layer thickness.

From the experimental point of view, the dielectric layer must be processed in a way that is innocuous to the front solar cells, and yet suitable for growing the back solar cell on top. The thickness of the dielectric layer is preferably less than 1 µm as observed in the simulations, yet still it must guarantee proper isolation of the inner silver electrodes of the back and front sub-cells.

The bottom to top fabrication of such devices imposes restrictions on the type of dielectric layer used, and also on the electron transport layer. For the back sub-cells, it is not possible to use layers with annealing temperatures above 80°C because this would reduce the performance of the PTB7-Th:$PC_{71}BM$ front sub-cell. Such a restriction rules out some of the possible dielectric layers to be employed, and also the ZnO by sol gel as it is used in the front sub-cells. As a replacement, a layer of PFN is deposited as the electron transport layer for the back sub-cell, as this can be processed either without annealing or with a mild

annealing of 70°C for 1 minute.

The search for a suitable dielectric layer included the testing of evaporated films. Metal oxides were ideal candidates for several reasons, for instance, the variety of refractive indexes that they exhibit, their transparency in the visible range, the possibility of a high thickness control through evaporation, among others. From this group of materials we tested MoO_3. We also trialled MgF_2, which is a well known dielectric material, widely used in antireflective coatings. Isolating polymers, such as PDMS, PEIE, PFN and other polymers intended for encapsulation, were tested as well. Distinct types of sol gels were trialled, including one based on a precursor to silicon oxide named Tetraethyl orthosilicate or TEOS and TiO_2. Solutions with nanoparticles and a set of UV curing epoxies were also evaluated. Out of the wide spectrum of possibilities, many of them had to be discarded for different reasons including low isolation and incompatibility with the processing of sub-cells. In the latter case, the problem could come either from an unavoidable processing step that would damage the front sub-cell, or from the inadequate roughness of the dielectric layer for the successful completion of the back sub-cell. In addition, not all the tested layers were compatible with the deposition of PFN. The material that fulfilled most of the requirements was a UV curing epoxy reference NOA65 from the company Norland Products. This material has a refractive index of 1.524 together with a high transmission, as observed in Figure 3.13.

NOA65 can be spin coated at low velocities on top of the front sub-cell in order to obtain a continuous and almost pinhole-free film. The 8 minutes of UV curing required for this material proved to have negligible effect on the front sub-cell. Perhaps the only problem with this material is that it is not possible to reach thicknesses below 1 µm given its inherent viscosity. Lower viscosity formulations

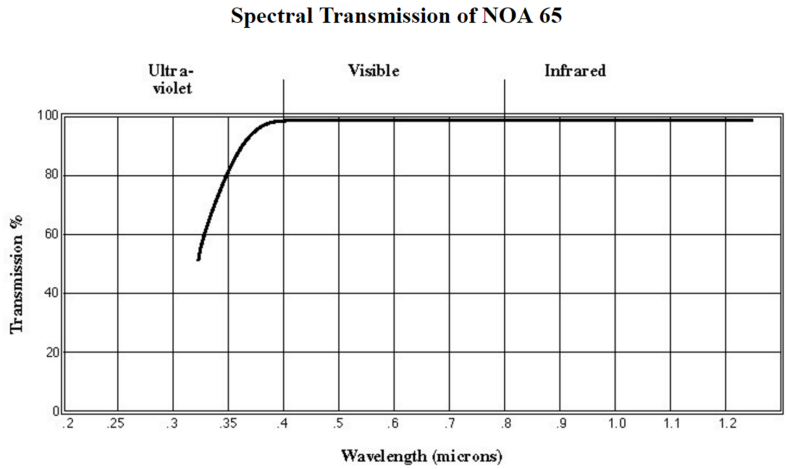

Figure 3.13: Transmission of NOA65 UV curing epoxy. As taken from [152].

of similar epoxy were tested without success and with a more frequent appearance of holes and imperfections within the layer. For this reason, NOA65 was kept as the choice for the dielectric layer fabrication.

To confirm the correct functionality of a solar cell grown on the NOA65 epoxy, a set of devices of Glass/Epoxy/MoO_3 /Ag/ MoO_3 /PFN/ PTB7-Th:$PC_{71}BM$/ MoO_3 /Ag was fabricated and compared to references directly deposited on glass. This architecture corresponds to the back sub-cells within the 4-terminal configuration.

The compared references and epoxy-grown devices showed similar performance. Voltage of 0.79V, FF of 58%, photocurrent of 14.5 mA/cm^2 and EQE shape were all similar, suggesting that, in principle, it is possible to have full operative devices grown on the epoxy. However, it was found that the devices grown on thin silver, both epoxy and glass, had a lower performance than expected according to the simulations.

The situation worsened within the complete 4-terminal structure, where the measured values for the photocurrent of both sub-cells remained well below the theoretical values. The fabricated structure, with all thicknesses in nm, was: ITO(100)/ZnO(10)/PTB7-Th:$PC_{71}BM$(100)/MoO_3 (5)/Ag(9.5)/ MoO_3 (65) / NOA65(8000) nm/MoO_3 (5)/Ag(9.5)/PFN(2) /PTB7-Th:$PC_{71}BM$(100)/ MoO_3 (5)/Ag(150). JV curves for the 4-terminal device are depicted in Figure 3.14.

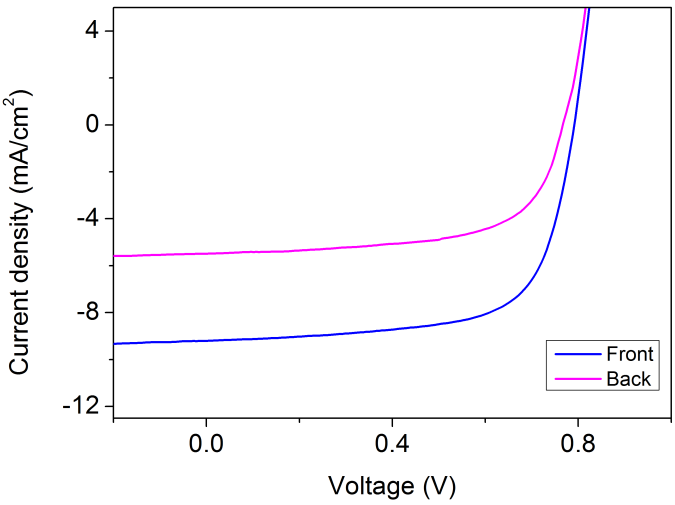

Figure 3.14: JV curve of sub-cells in a configuration (layers in nm): ITO (100)/ZnO(10)/PTB7-Th:$PC_{71}BM$(100)/MoO_3 (5)/Ag (9.5)/ MoO_3 (65)/ Dielectric (8 microns)/ MoO_3 (5)/Ag (9.5)/PFN(2)/ PTB7-Th:$PC_{71}BM$(100)/ MoO_3 (5)/Ag (150).

The fact that opaque cells based on ITO presented an accurate match to our simulations as seen in Figure 3.15 indicated that the problems were likely arising from the thin silver layers. To characterize the thin silver thoroughly, we performed ellipsometric measurements on the thin silver layers of 10 nm deposited on top of the system Glass/PTB7-Th:$PC_{71}BM$/MoO_3 in order to obtain valid optical constants.

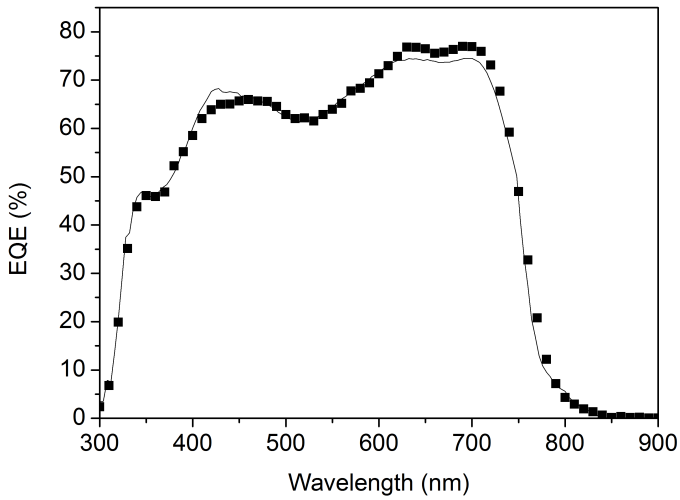

Figure 3.15: Experimental EQE (black dots) versus simulated one (continuos line) for an inverted opaque solar cell.

The significant differences between the constants reported by Palik and the ones measured at ICFO, shown in Figure 3.16, explained the dramatic reduction in photocurrent observed in our experiments (Table 3.4). The change in the optical constants resembles trends that have been published for the case of aggregated silver [153], suggesting that the flatness and homogeneity of the evaporated thin layer is far from being as required.

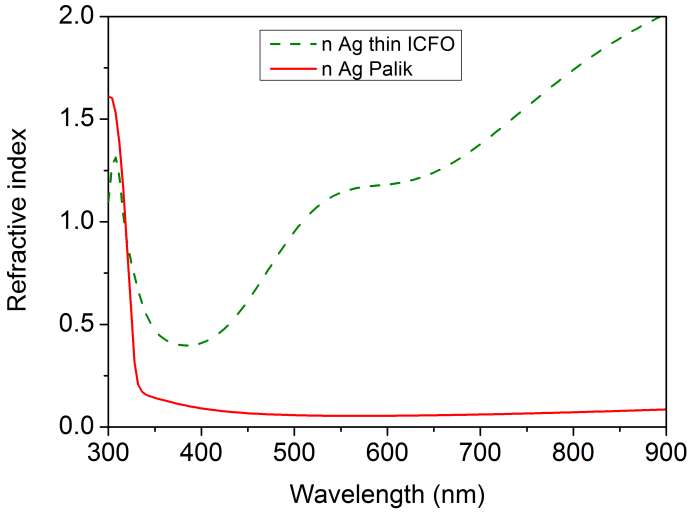

(a)

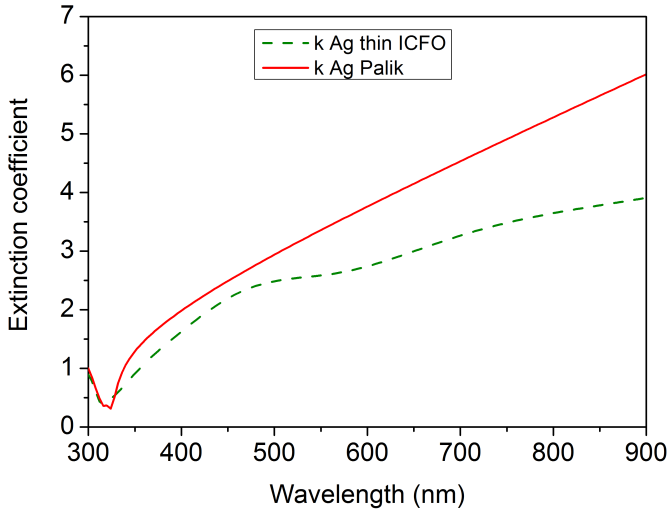

(b)

Figure 3.16: Comparison of a) refractive index and b) extinction coefficient as measured at ICFO and taken from Palik.

Table 3.4 shows the PV parameters of the fabricated 4-T device compared to the theory for such architecture employing the bulk Ag constants and the ones measured at ICFO. For the simulations, a non-absorbing dielectric of 8 µm and 1.52 refractive index is employed together with Ag layers of 8.5 nm.

Table 3.4: Experimental results and theoretical values of 4-terminal device.

Cell	$J_{sc}[mA/cm^2]$	$V_{oc}[mV]$	$FF[\%]$	$PCE[\%]$
front (experiment)	9.20	790.74	67.76	4.93
back (experiment)	5.48	770	63.25	2.67
front theory (Ag Palik)	11.06	-	-	-
back theory (Ag Palik)	8.57	-	-	-
front (Ag ICFO)	10.5	-	-	-
back (Ag ICFO)	5.4	-	-	-

Provided with the newly obtained Ag constants, we executed further simulations varying the dielectric layer while keeping the other layers constant as described in Table 3.5, and found a diminished maximum photocurrent. As observed in Figure 3.17, the highest sum of photocurrents J_{sc1} and J_{sc2}, corresponding to the back and front sub-cells respectively, does not outperform the 16.65 mA/cm^2 of the best single junction device for the architecture evaluated in Table 3.5.

Table 3.5: Configuration of 4-terminal device simulated as observed in Figure 3.10 using ICFO measured Ag index and a 7.5 nm silver layer.

Layer	Thickness range [nm]	Best thick-ness [nm]	Best n	$J_{sc}[mA/cm^2]$
ITO	fixed	135	fixed	
ZnO	fixed	10	fixed	
PTB7-Th:$PC_{71}BM$	fixed	100	fixed	10.03
MoO_3	fixed	5	fixed	
Ag thin	fixed	7.5	fixed	
Dielectric layer	50-950	230	1.9	
Ag thin	fixed	7.5	fixed	
PFN	fixed	1	fixed	
PTB7-Th:$PC_{71}BM$	fixed	100	fixed	6.00
MoO_3	fixed	5	fixed	
Ag	fixed	150	fixed	
$J_{sc1} + J_{sc2}$				16.03

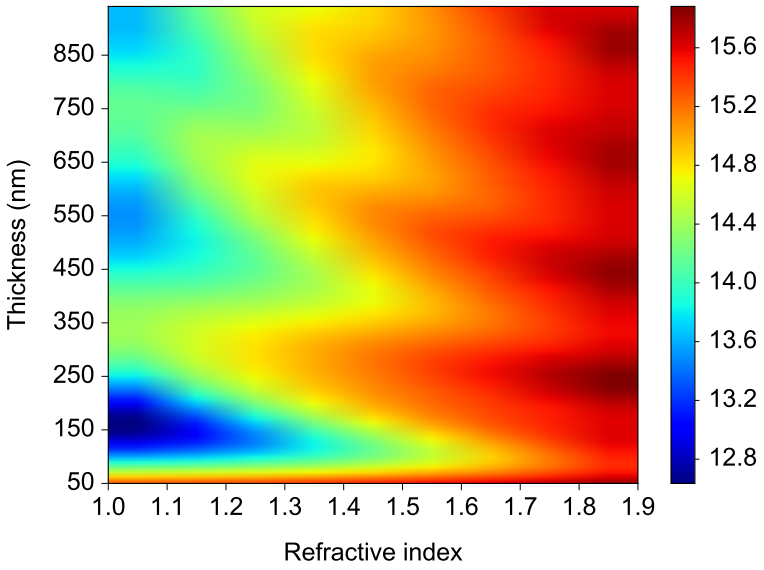

Figure 3.17: Calculated sum of J_{sc1} and J_{sc2} using ICFO Ag index against variations of the dielectric layer for intermediate silver layers of 7.5 nm.

Table 3.6 shows the effect of pushing the silver thickness further down to 4.7 nm, which allows an increase of the total photocurrent to 17.16 mA/cm^2. This value represents a subtle improvement in the photocurrent of 3% over the single junction device, assuming that the optical constants obtained for the 10 nm silver films are still valid. To check for this, it would be necessary to execute the ellipsometric measurements on such thin layers to observe how much the optical constants deviate.

Table 3.6: Configuration of 4-terminal device as observed in Figure 3.10 using ICFO measured Ag index and a 4.7 nm silver layer.

Layer	Thickness range [nm]	Best thick-ness [nm]	Best n	$J_{sc}[mA/cm^2]$
ITO	fixed	135	fixed	
ZnO	fixed	10	fixed	
PTB7-Th:$PC_{71}BM$	fixed	100	fixed	10.06
MoO_3	fixed	5	fixed	
Ag thin	fixed	4.7	fixed	
Dielectric layer	50-950	50	1.9	
Ag thin	fixed	4.7	fixed	
PFN	fixed	1	fixed	
PTB7-Th:$PC_{71}BM$	fixed	100	fixed	7.10
MoO_3	fixed	5	fixed	
Ag	fixed	150	fixed	
$J_{sc1} + J_{sc2}$				17.16

Experimental efforts towards fabrication of such ultrathin silver films to study their properties and viability are described in Chapter 5.

3.3 4-terminal devices with ITO as light entrance electrode and Au inner electrodes

In general, there are different experimental factors that affect optical performance and morphology of metallic films. These include the deposition rate, base pressure in the deposition chamber, substrate temperature and the film thickness. In

particular, we detected that thin silver films ($\leq$ 10 nm) diverged from their bulk optical properties. Such changes hindered the potential improvements of the multi-junction architecture. This limitation motivated us to try other metals for the 4-terminal architecture. Aluminum and gold were possible materials, as from literature and previous work performed inside our group we knew that both could form efficient electrodes for the opaque OSC. From the two options, we opted for gold given its improved stability and suitability for ultra-thin layers [154]. The 4-terminal structure with gold is depicted in Figure 3.18.

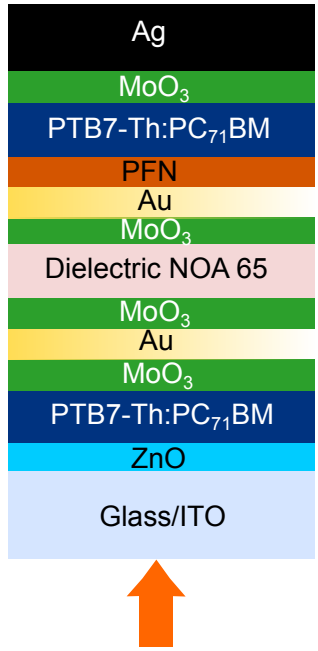

Figure 3.18: 4-terminal architecture using thin gold electrodes.

Before building the complete 4-terminal devices, single junction semi-transparent devices with gold were fabricated and characterized. The layer thicknesses in nanometers were: ITO(135)/ZnO(10) /PTB7-Th:$PC_{71}BM$(100)/ MoO_3(5)/Au(8.5). Table 3.7 shows the average values for the semi-transparent

solar cells with the best values in parentheses. The FF for a device with such a thin layer of gold stays remarkably high, with a highest value that resembles that of an opaque reference device with PTB7-Th:$PC_{71}BM$.

Table 3.7: Average PV parameters of semi-transparent devices using gold.

$J_{sc}[mA/cm^2]$	$V_{oc}[mV]$	FF[%]	PCE[%]
9.86 ± 0.07 (9.93)	784.52 ± 2.80 (788.91)	67.48 ± 1.49 (69.34)	5.22 ± 0.16 (5.27)

The experimental (squares) and calculated (line) EQE of the semitransparent device with thin Au are shown in Figure 3.19. A good agreement is observed between the two curves. Most importantly, a very good match is obtained between the measured and calculated transmission of the semi-transparent device made with gold as seen in Figure 3.20, when using the optical constants from the bulk [155]. In addition, the transmission of a single Au electrode deposited on MoO_3 is also compared with the calculated transmission in Figure 3.21, displaying a very good match. Unlike silver, the bulk constants for gold can be used for the simulations of the herein fabricated thin layers.

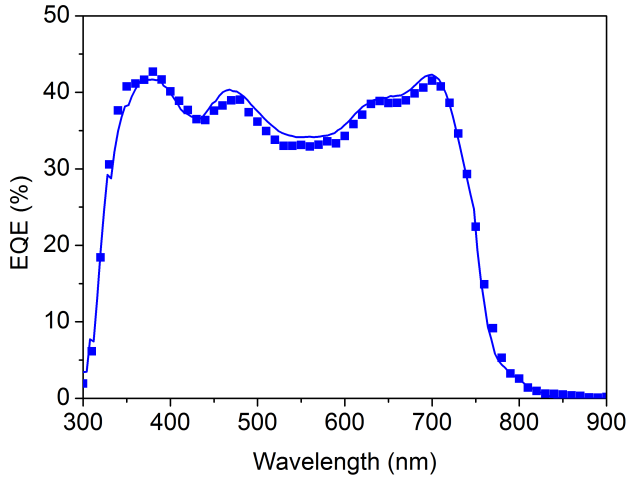

Figure 3.19: Experimental (squares) and measured (line) EQE values for the semi-transparent Au device.

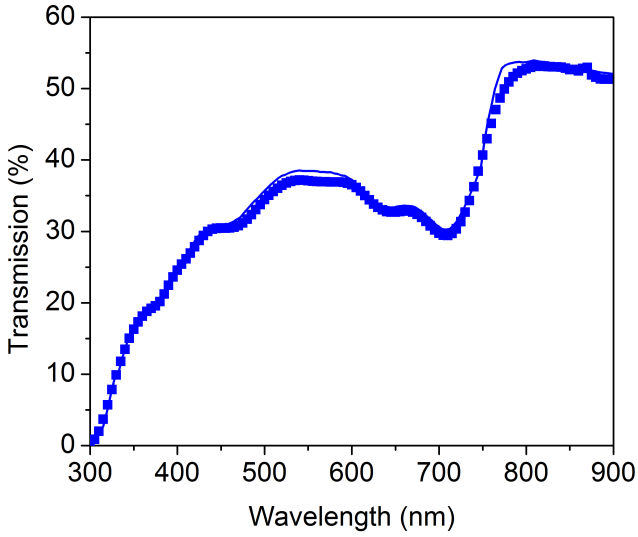

Figure 3.20: Experimental (squares) and measured (line) transmission for the semi-transparent Au device.

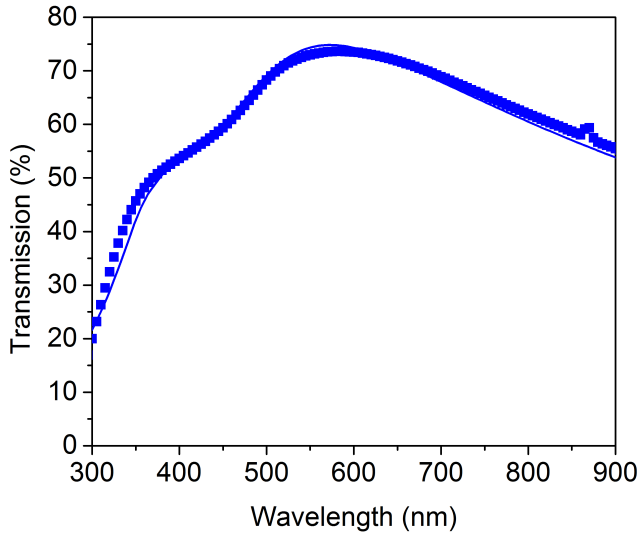

Figure 3.21: Experimental (squares) and measured (line) transmission for the semi-transparent MoO_3 5nm and Au 8.5 nm electrode.

Using the Au constants from the bulk, we performed similar calculations as those with the Ag electrodes, and obtained a new map for the sum of the photocurrents versus the thickness and refractive index of the dielectric. To perform the calculations we fixed the thicknesses of the rest of the layers, and set the thickness of both Au electrodes to 8.5 nm, as shown in Table 3.8.

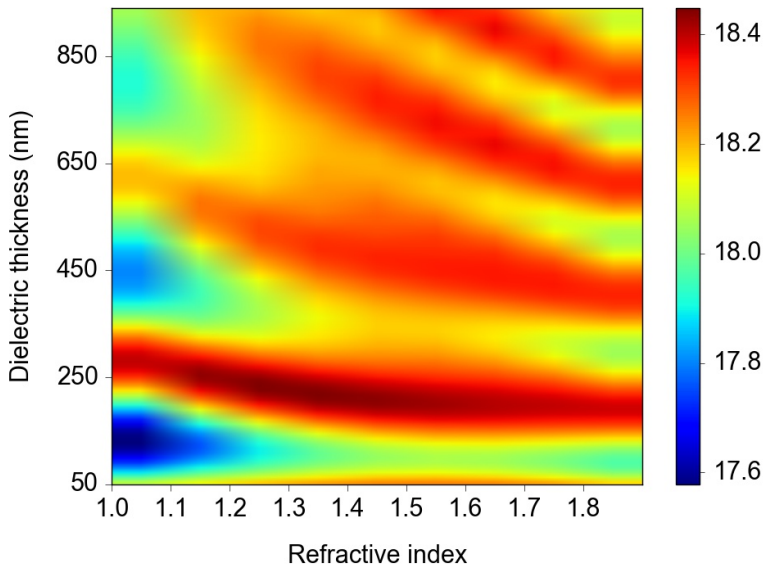

Figure 3.22: Sum of photocurrents J_{sc1} and J_{sc2} corresponding to back and front sub-cells respectively, using bulk Au index and varying the refractive index and thickness of the dielectric layer.

For such a current map, it is observed that the maximum sum of photocurrents is below the calculated with the bulk silver constants, but it is above the calculations performed with the measured silver constants. These results confirmed that implementing Au intermediate electrodes could extract the potential of the 4-terminal structure.

Table 3.8: Optimal configuration of 4-terminal device as observed in Figure 3.18 using bulk Au index and a 8.5 nm layer.

Layer	Thickness range [nm]	Best thick-ness [nm]	Best n	$J_{sc}[mA/cm^2]$
ITO	fixed	135	fixed	
ZnO	fixed	10	fixed	
PTB7-Th:$PC_{71}BM$	fixed	100	fixed	10.71
MoO_3	fixed	5	fixed	
Au thin	fixed	8.5	fixed	
MoO_3	fixed	62.8	fixed	
Dielectric layer	50-950	230	1.2	
MoO_3	fixed	20	fixed	
Au thin	fixed	8.5	fixed	
PFN	fixed	1	fixed	
PTB7-Th:$PC_{71}BM$	fixed	100	fixed	7.74
MoO_3	fixed	5	fixed	
Ag	fixed	150	fixed	
$J_{sc1} + J_{sc2}$				18.45

Once the first step of testing the single junction semi-transparent device was finished, we fabricated 4-terminal structures using the dielectric NOA 65. The proposed structure replaces the intermediate silver electrodes in Figure 3.10 with thin gold electrodes. This architecture is shown in Figure 3.18.

Table 3.9 shows the experimental results using thin gold. The experimental structure is composed by the layers in nm: ITO(135)/ZnO(10) /PTB7-Th:PC71BM(100)/MoO3(5)/Au(8.5)/ MoO3(62)/Dielectric NOA(8 µm)/ MoO3(20)/PFN(1)/ PTB7-Th:PC71BM (100)/ MoO3(8)/Ag(100). In practice, we obtained an improvement in photocurrent of 4%. In Table 3.10 we show the PV parameters of the sub-cells within the 4-Terminal structure. The efficiency of the 4-Terminal device corresponds to the sum of the efficiencies of its sub-cells. Even though a higher photocurrent is obtained, the overall efficiency is slightly below that of the single device due to losses that appear in the V_{oc} and FF of both front and back sub-cells. Further processing optimization would allow having a monolithic 4-Terminal device based on thin gold, able to provide higher efficiency than the best single devices.

Table 3.9: Experimental photocurrent density for the 4-T architecture with gold compared to single opaque reference.

Subcell	4-T exp.$J_{sc}[mA/cm^2]$	Ave. Single exp. $J_{sc}[mA/cm^2]$
Front cell	10.24	16.65
Rear cell	7.11	-
Sum of Jsc	17.35	16.65

Table 3.10: Comparison of PV parameters of semi-transparent devices using gold versus average of single opaque device.

Device	$J_{sc}[mA/cm^2]$	$V_{oc}[mV]$	$FF[\%]$	$PCE[\%]$
Single opaque	16.65	783.02	71.81	9.36
Front cell	10.24	778.9	64.56	5.15
Back cell	7.11	761.82	68.14	3.69
4-Terminal with Au	-	-	-	8.84

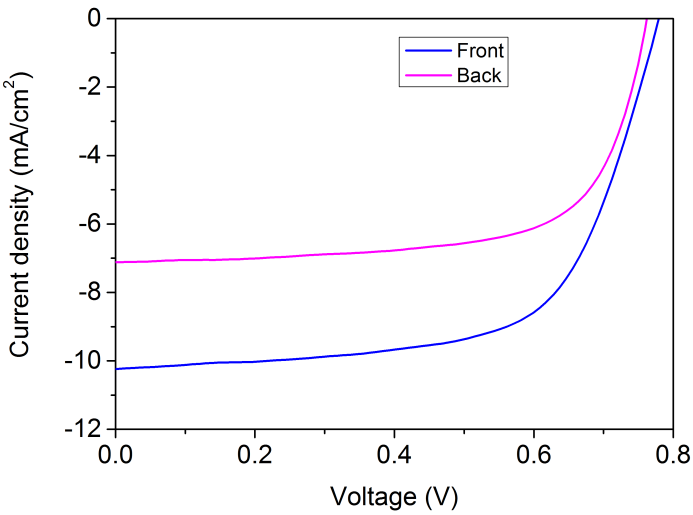

Figure 3.23: JV curves of sub-cells within 4-terminal architecture with thin gold electrodes. Front cell (blue) and back cell (magenta).

3.4 Conclusions

By numerically determining the optimal layer configuration in a 4-terminal tandem cell of the same active blend on a bi-coated ITO substrate, we demonstrated that it is possible to obtain devices that perform better than single junction devices with an equivalent thickness of active material. In other words, the configuration we proposed is optimal to increase light absorption by using active layers with thicknesses below 130 nm, able, in principle, to deliver a good electrical performance for the majority of the low band gap polymer cells. We have used the optical simulations as a guideline to fabricate a proof of principle 4-terminal device using PTB7:$PC_{71}BM$ blend as the blend material for the active layers of two inverted sub-cells. We fabricated the two sub-cells on each side of a 1.1 mm thick glass substrate coated on both sides with ITO. The overall trend of light harvesting capacity seen in the experimentally measured EQEs for the two sub-cells of the fabricated devices is in agreement with the EQEs predicted by the optical model. We have demonstrated that absolutely no degradation in the electrical performance of the 4-terminal cell relative to the single junction devices is seen when the two sub-cells are connected in a series configuration.

The theoretical photocurrent improvements of the 4-terminal architectures when operated independently over the best single junction device reach the 20% when using silver and 11% when using gold as intermediate electrodes. We fabricated the 4-terminal devices on a one-sided ITO coated substrate based on PTB7-Th:$PC_{71}BM$ using both metals as intermediate electrodes. In this way, a standard full bottom to top fabrication was used. We found an appropriate dielectric layer to deposit in between the two sub-cells which was innocuous to the front sub-cell and suitable for the fabrication of the back sub-cell. In such 4-terminal devices based on PTB7-Th:$PC_{71}BM$ the cells operated independently. As in the case of the 4-terminal devices on a bi-coated ITO, we observed that ex-

perimental and theoretical results followed the same trends, once the right optical constants were employed. By implementing thin gold as intermediate transparent electrodes, we demonstrated experimentally that the photocurrent of the homo 4-T configuration can be increased by more than 4% relative to an optimal single junction device. Further optimization in the processing is required to keep the V_{oc} and FF at their optimal levels in such 4-T architecture.

Chapter 4

Monolithic CIGS-Perovskite Tandem Cell for an Optimal Light Harvesting Without Current-Matching

As discussed in the previous chapter, 4-terminal devices represent an alternative to partially circumvent the problem of current-matching in regular tandem solar cells devices. Recent reports have shown outstanding results for 4-terminal devices employing only PVK, and PVK combined with CIGS or Silicon [40, 41, 42, 43, 44, 45]. The connectivity complexity of the 4-T modules is, however, a pending issue. Additional connection schemes have been suggested. On a theoretical basis, it was proposed to connect an indefinite number of cells in each one of the branches of a parallel configuration in series until the voltages of the two branches are matched [156]. However, no practical implementation of the device configuration was considered. An alternative option proposed piling up three cells, two of them in a series connection, with these two then connected

in parallel with the remaining one [157]. The latter combination is an interesting proposal to match the voltage but the problem of current-matching remains unresolved.

In this chapter, we propose a new configuration, denoted as S-P (serial-parallel) and using PVK and CIGS sub-cells, which is different from the standard or any other tandem scheme considered until now. We describe an architecture that, in spite of being monolithic, does not require current-matching between the PVK and CIGS cells. Performing an optical optimization of the structure, we predict an efficiency close to 28% using a 1.56 eV band-gap PVK, superior to any of its constituents' sub-cells. Furthermore, we discuss the experimental viability of the proposed architecture.

4.1 Analysis of S-P architecture

The configuration denoted as S-P, is different than the standard or any other tandem scheme considered until now. As shown in Figure 4.1, the configuration is formed with a semi-transparent PVK solar cell deposited on top of two CIGS solar cells laterally connected in series. A schematic drawing of the architecture with connection nodes numbered from 1 to 3 is shown in Figure 4.2. Voltage-matching at nodes 1 and 3 from both branches of the circuit may, in principle, be achieved provided the maximum power point voltage V_{mpp} of the light-filtered CIGS cells is close to half the one from the PVK cell. The serial connection between the two CIGS cells can be implemented by means of laser scribing, a standard technique for the upscaling of CIGS cells to modules. As seen in Figure 4.1, a 1-D photonic non-periodic dielectric structure (NDS) is inserted on top of the first CIGS solar cell, serving the double purpose of avoiding short-circuiting of nodes 1 and 2 and maximizing light absorption for the first and second cell. The necessary current-matching between the two serial connected CIGS devices

can be easily obtained by defining an equal area for both.

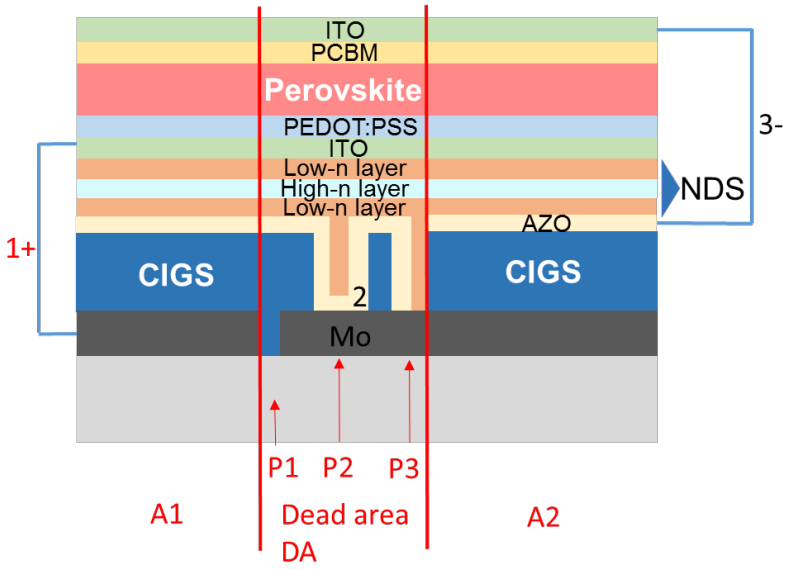

Figure 4.1: Schematic drawing of the monolithic multi-junction device composed of two series connected CIGS cells connected in parallel with a PVK cell.

In the implementation of the optical optimization, we consider an architecture where the CIGS solar cell is maintained but some changes are introduced to the PVK device, for instance, the use of top and bottom transparent conductive electrodes (TE). Specifically, the S-P architecture consists of the semi-transparent PVK cell on top of a CIGS cell separated by the NDS as follows: Glass/Mo/MoSe/CIGS/CdS/i-ZnO/AZO/ Low-n film/High-n film/ Low-n film/TE /PEDOT:PSS/PVK/PCBM/ TE /MgF_2. As TEs for the semi-transparent PVK we considered 90 nm ITO films. The ITO is chosen instead of the common FTO due to its better processing compatibility with the underlying materials and its improved near infrared transmission. Similar thickness of ITO films, prepared at room temperature, have been employed to form a recombina-

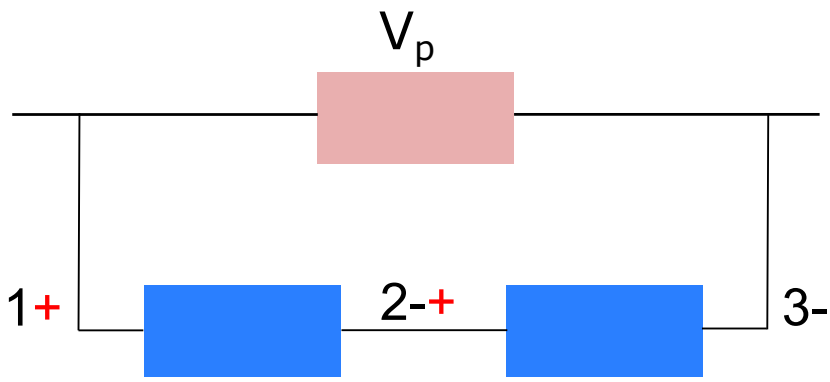

Figure 4.2: Schematic drawing of the connections of the S-P configuration.

tion layer and top contact in a monolithic tandem architecture with PVK and Silicon, exhibiting high fill factors [158]. In the S-P configuration considered here, the optical optimization is performed for a device that includes the NDS between the inner TE/AZO interface as seen in Figure 4.1. Such an NDS is formed by combining three layers of intercalated low and high refractive index materials, and has a two-fold functionality. Firstly, it electrically separates the TE anode of the PVK and the AZO cathode from the CIGS and, secondly, it confines the incident sunlight above the PVK band-gap in the PVK absorber layer, while increasing the transparency for sunlight below the PVK band-gap for an efficient coupling into the CIGS bottom cell. To prevent tunneling from electrical charges between the PVK and CIGS cells, as the low-n material one may use MgF_2, a highly insulating transparent material exhibiting a refractive index close to 1.38. For the high-n film, a highly transparent dielectric material with a refractive index of 2.2 would be the optimal. Possible materials for the high index layer may be TiO_2 or Si_3N_4. Considering the three films, the thickness of the NDS would be above 500 nm, sufficient, in principle, to prevent electrical charge tunneling. When the inverse integration optical optimization detailed in section 4.2 is applied, the EQEs obtained for the NDS separated PVK and CIGS cells are shown

in Figure 4.3a. We found that three layers provided better results than using only a single dielectric. Also, implementing five or more low-n and high-n layers was not considered as the gain in photocurrent was negligible.

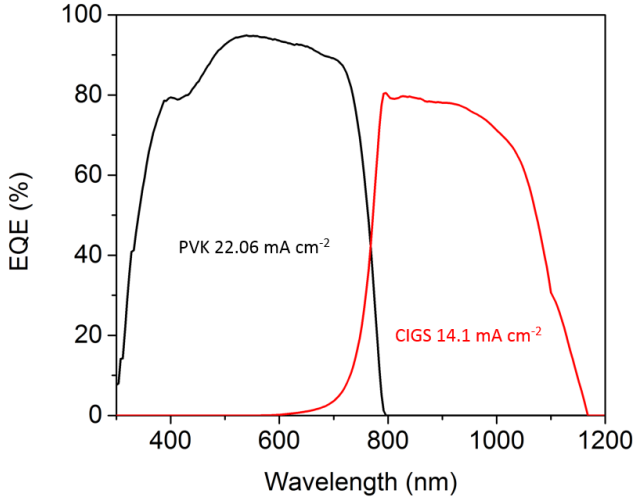

(a)

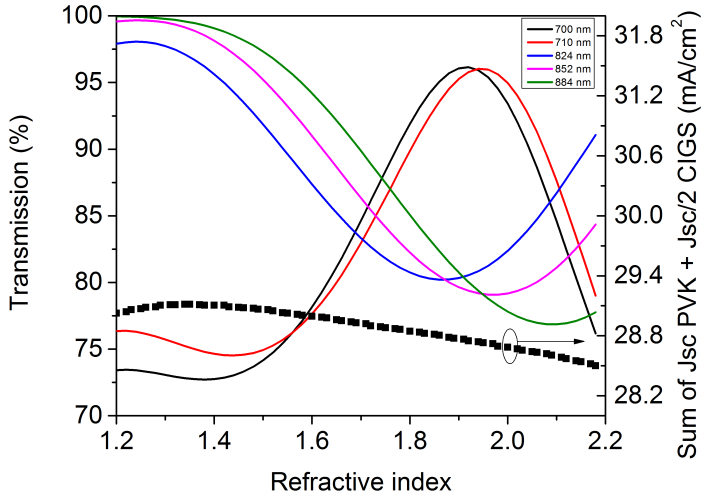

(b)

Figure 4.3: a) Calculated EQE for the Perovskite (black) and the CIGS (red) sub-cells for the optimal configuration. b) Sum of PVK and CIGS photocurrents densities (black squares) and transmission of the NDS at 700 nm (black line), 710 nm (red), 824 nm (blue dash), 852 nm (magenta dash dot), and 884 nm (green dash dot dot) as a function of the refractive index of the low-n NDS layer.

Under the assumption of a negligible extinction coefficient for any of the layers within the NDS, we observe an enhancement in the maximum short-circuit current of the PVK and CIGS sub-cells, especially in the wavelength range between 700 and 900 nm. The NDS fine tuning required to reach maximum PCE may be extracted from Figure 4.3b where the transmission at 5 different wavelengths just above and below the PVK bandgap is shown as a function of the NDS low refractive index material. In such figure one observes that for the cell architecture with the highest short-circuit current sum, when the NDS low index material is close to 1.38, the inverse integration leads to an NDS transmission larger at longer wavelengths to favour absorption at the CIGS and smaller at shorter wavelengths to favour absorption in the PVK. Note that the unbalanced current density in both sub-cells explains why the PCE of the S-P configuration is considerably larger than the PCE for the current matched tandem, as seen in Figure 4.4.

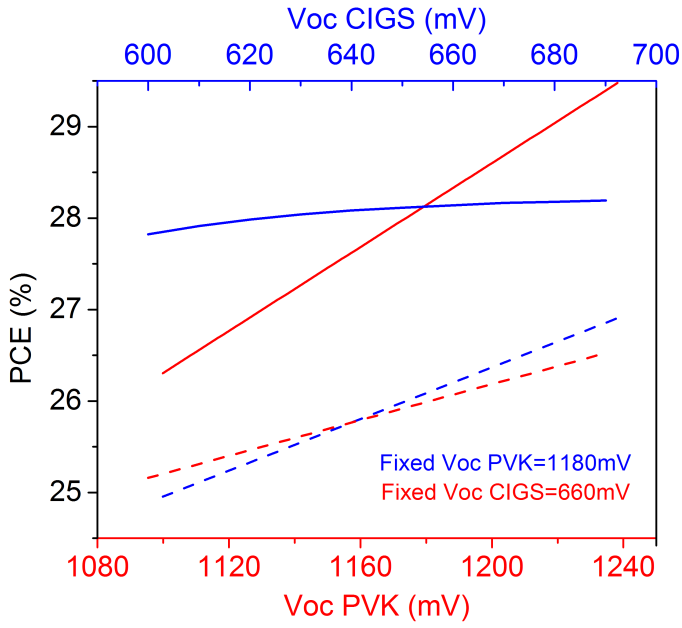

Figure 4.4: PCEs for the tandem (dashed) and S-P (continuous) configurations. Red lines correspond to a fixed V_{oc} for the CIGS solar cells at 660 mV while the V_{oc} of the PVK is allowed to change from 1080 to 1240 mV. Blue lines correspond to a fixed V_{oc} of the PVK at 1180 mV while the V_{oc} of the CIGS is allowed to change from 600 to 690 mV.

To confirm that such increase in photocurrent in the S-P configuration corresponds to an equivalent increase in PCE, we determined the rest of the electrical parameters that characterize the overall IV curves employing the single diode electrical equivalent circuit model. The single diode circuit model was applied to each branch of the circuit and then the currents were added point by point to obtain the resulting IV curve. To reach optimal PCEs we set the FF between 80 % and 81 % for all the single junction cells used in the S-P configuration. A similar procedure was used to determine the optimal configuration for a standard current matched tandem, which is used as a reference for comparison. Although

small variations resulting from the IV curves fitting may be found, the FF of the S-P structure closely approached that of the sub-cell with the highest FF for most of the cases considered. On the other hand, the V_{oc} of the S-P is roughly limited by the voltage of the branch that has the lowest voltage, as can be seen in Figure 4.5. We studied two cases, one where the V_{oc} of the PVK was fixed to 1180 mV while the V_{oc} of the CIGS was varied in the 600-700 mV range, and a second case where the V_{oc} of the CIGS was fixed to 660 mV and the one of the PVK was allowed to change in the 1080-1240 mV range. The ideality factor, series resistance, shunt resistance, and saturation current were determined to match experimental curves when available, as seen in Figure 4.6, or from the computer generated single junction IV curves exhibiting the targeted J_{sc}, FF and V_{oc} parameters. Note that the changes in V_{oc} considered in here are not associated to bandgap modifications which will be considered below. Indeed the V_{oc} ranges encompass a wide variety of voltages that are often found in experimental CIGS or PVK single junction devices.

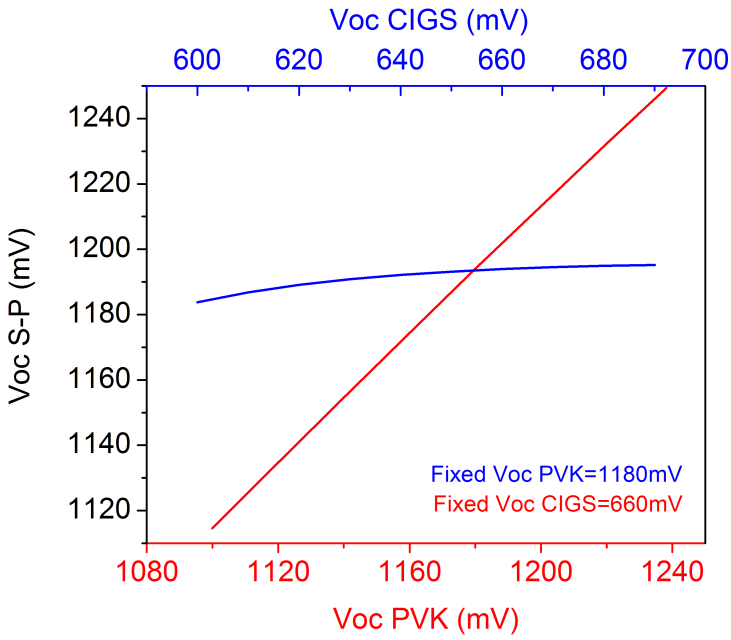

Figure 4.5: Equivalent V_{oc} for the S-P configuration when varying the V_{oc} of the PVK subcell with a fixed V_{oc} for the CIGS of 660 mV (red) and for variations of the CIGS $V_{oc}$with a fixed PVK V_{oc} of 1180 mV.

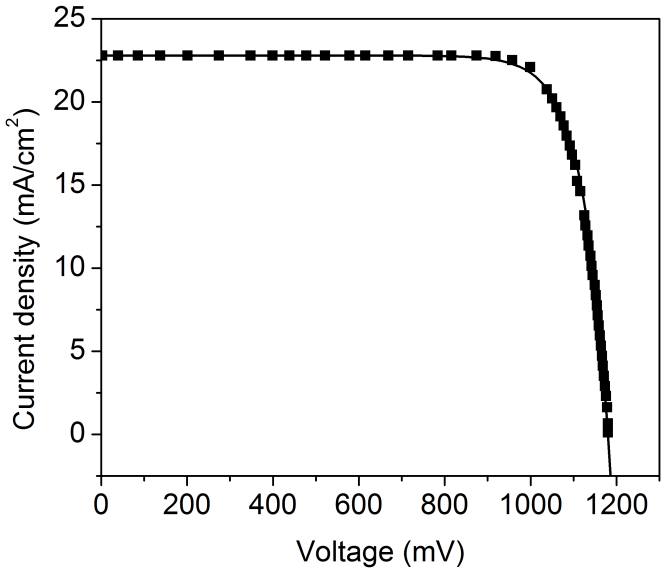

Figure 4.6: Fitting of experimental IV curve of a Perovskite cell (squares) Ref. [160] with model (line) using parameters in Table 4.1.

Table 4.1: Diode parameters for the fitting of an experimental curve in Ref. [160].

Saturation current density $[mA/cm^2]$	$4e-8$
Diode ideality factor	2.34097
Resistance $[ohmcm^2]$	$3.91e-5$
Short-circuit current density $[mA/cm^2]$	22.8

As seen in Figure 4.4, when a PVK cell with a V_{oc} of 1180 mV is combined with a CIGS cell in the S-P configuration, the efficiency remains more less around the 28% as the V_{oc} of the CIGS changes. This PCE is clearly larger than the PCE from any of the possible tandem configurations also shown in Figure 4.4. In the event that the V_{oc} of the PVK is further increased, PCEs above 29% would be reachable while for the standard tandem PCEs larger than 27% are, in prin-

ciple, not possible. This confirms that the S-P configuration clearly outperforms the standard tandem by more than two percentage points in almost all cases. Note that, when optimal single junction cells are considered, both configurations tandem and S-P, will clearly outperform record PCEs for CIGS [51] and PVK [10] single junction cells.

Provided that in the S-P configuration no current-matching is required between the PVK and the CIGS cells, a further increase in the PCE may be achieved by tuning the band-gap of either the PVK or CIGS cells. For PVK cells, several authors have considered tuning the band-gap by changing the relative halide composition and observed an increase in the V_{oc}. Although in most cases studied no clear relationship was established between the V_{oc} and the band-gap, from the wide band-gap tuning study reported by Noh et al. [37], one may extract a close to linear correspondence between these two parameters when the band-gap is changed from 1.57 eV to 2.29 eV. The V_{oc} values therein reported are, however, low in comparison to recent reports. For instance, PVK cells with a measured band-gap of 1.56 eV have reached a V_{oc} as high as 1.19 V [161]. Similarly, for a higher band-gap PVK of 1.62 eV, a V_{oc} of 1.24 eV [160] was recently achieved which corresponds to a loss-in-potential (difference between the band-gap and V_{oc}) of 0.39 eV which is close to the thermodynamic limit. Thus, an increase in V_{oc} may be achievable for the other band-gaps as well, once the charge extraction contacts and the perovskite composition have been optimized to overcome limiting effects such as the one described in Ref [159]. For this work, the above two values are taken as references and used to establish a linear relation between the V_{oc} and the band-gap in the range of 1.51 eV to 1.71 eV, as shown in Figure 4.7. At present, there are material compositions for PVK cells yielding band-gaps below 1.56 eV [162, 163, 164]. However, such compositions have led to suboptimal devices, which were not taken as references for this analysis.

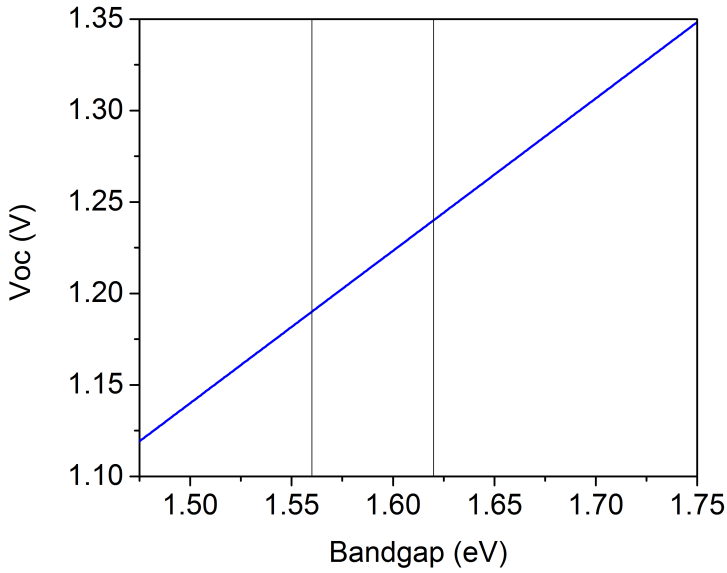

Figure 4.7: Estimate of PVK V_{oc} as a function of the PVK bandgap. The two reference values are marked as vertical lines.

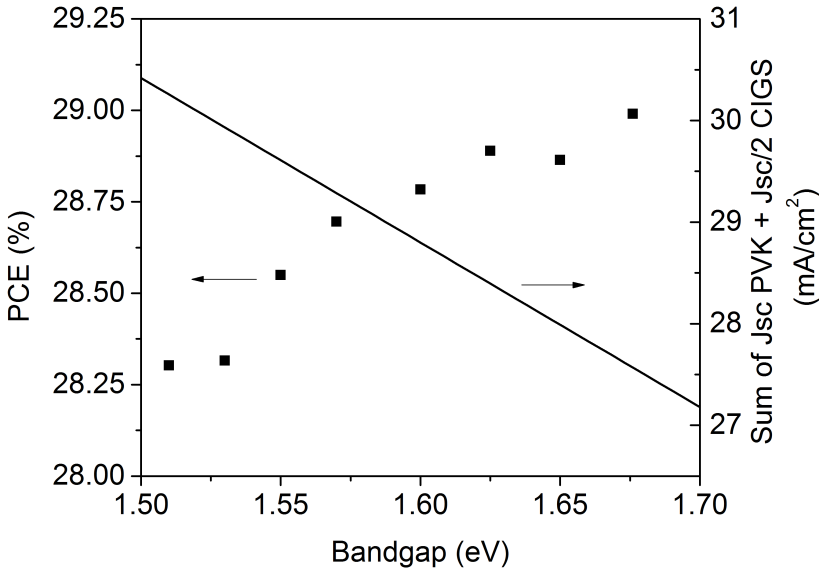

Figure 4.8: PCE of the CIGS/PVK S-P cells as a function of the PVK bandgap (squares) and sum of PVK and CIGS halved short-circuit current densities for the S-P configuration as a function of the PVK bandgap (line).

A monotonic decrease in the total calculated short-circuit current density as the band-gap increases is observed in Figure 4.8. Note that we have plotted the sum of the short-circuit density of the PVK with half of the CIGS to account for the differences in area inherent to the S-P structure. When estimating the PCE using the same single diode model described above one observes, as can be seen in Fig. 4.8, an increase in PCE as the band gap of the PVK increases. Although this may seem counter-intuitive provided the bandgap of PVK is well above the optimal single junction solar cell bandgap, the explanation is that the bandgap increase implies a better voltage matching with the CIGS branch of the circuit.

4.2 Design and experimental considerations of S-P architecture

4.2.1 Intercalated non-periodic photonic structure for an optimal light harvesting

To design the specific architecture for the S-P cell, we set the sum of the photocurrents as the target optimization parameter within our numerical calculations. We use a combined approach using TMM and inverse problem solving, as explained in Chapter 1. From Figure 4.2, it can be seen that the maximum electrical power P derived from the device is given by:

$$P = (I_{CIGS} + I_{PVK}) * V_p * FF \tag{4.1}$$

where I_{CIGS} is the short-circuit current generated by the CIGS solar cell and I_{PVK} s the short-circuit current generated by the PVK. V_p and FF are the corresponding voltage and fill factor from the parallel connection.

$$I_{PVK} = J_{PVK} * (A_T) \tag{4.2}$$

J_{PVK} being the short-circuit current density from the PVK and A_T the total illumination area of the device. Neglecting the dead area, A_T corresponds to:

$$A_T = A_1 + A_2 \tag{4.3}$$

where A_1 and A_2 are the areas for the CIGS sub-cells (for practical considerations refer to the next subsection). The current flowing through the CIGS cells must fulfil:

$$I_{CIGS} = A_1 * J_{CIGS1} = A_2 * J_{CIGS2}. \tag{4.4}$$

By simple algebra, one may write the PCE as:

$$PCE = ([(A_1 * J_{CIGS1}) + (A_T * J_{PVK})] * V_p * FF)/(P_{AM1.5} * A_T) \quad (4.5)$$

Using the calculated optical electric field intensities for the CIGS and PVK, together with their optical constants, the absorption is computed to finally determine the short-circuit current density (J_{sc}) for each sub-cell. J_{sc}' s for the PVK and CIGS cells were computed for 10,000 different combinations of layer thicknesses when varying the absorber layers, the entrance transparent electrode, and the intermediate dielectric NDS layers. The refractive indexes for each layer were taken from references [165, 166] for the CIGS solar cell and from references [167, 168] for most of the layers in the PVK solar cell. The thickness ranges were always in accordance with the experimental constraints to obtain optimal FF or V_{oc} for both cells. We assumed an internal quantum efficiency (IQE) of 100% for the PVK cell as demonstrated in Refs. [169, 170] and 92% for the CIGS solar cells [171]. In the PCE estimates, we obtained the equivalent parallel voltage V_p and FF by adding the IV curves corresponding to each one of the branches of the circuit.

4.2.2 Experimental implementation of S-P structure

The CIGS bottom cells in this design can be deposited in the different ways described in literature, since there are no special limitations on process temperature or conditions present at this point. In order to reach the desired efficiency, a deposition by co-evaporation or precursor selenization seems to be favorable. The substrate can be rigid (soda lime glass) or flexible (polyimides, steel), especially in view of possible roll-to-roll production. Back contact is typically Mo around 500 nm. The absorber will be between 2 and 3 µm thick, followed by a buffer layer (most likely CdS by chemical bath deposition) and a multilayer of intrinsic

and doped Zinc oxide as TE. The front contact sheet resistance should be below 10 Ohm/sq for a monolithic cell interconnection.

Concerning the fabrication of the PVK device on top of the CIGS, a number of constraints are introduced to prevent damage to the bottom CIGS layer. For instance, thermal instability has been observed for the n-type buffer layer in CIGS solar cells, where atoms tend to diffuse from the buffer to the absorber layer, significantly reducing the performance of the device by an augmented recombination. Temperatures above 300°C trigger this process and have been shown to be detrimental to all PV parameters of CIGS solar cells [172]. Therefore, annealing processes used to manufacture all the layers within the PVK device are temperature-limited, which excludes the use of frequent configurations like the mesoscopic PVK on 500°C sintered TiO_2. The PVK layer itself does not require high temperature annealing and neither does the PCBM. On the other hand, both ITO and In_2O_3:H have been shown to provide good quality transparent electrodes at the bottom or the top of PVKs solar cells [44, 173]. Connection of PVK cells to modules has been reported in the literature [174], some with a reduced area loss of 3% of the total 16 cm^2 module area [175].

As with the case of PVK, for the lateral serial connection of the CIGS solar cells, three structured patterns denominated P1, P2 and P3 are required, as seen in Figure 4.1. The first pattern P1 and the third pattern P3 separate the positive and negative contacts of adjacent cells, respectively. The second pattern P2 allows the negative contact of one cell to be connected to the positive contact of the following cell. The region between P1 and P3, inclusive, is the dead area (DA). Typically, laser scribing is employed to define such patterns. If we assume that the dead area corresponds to a fraction X of the total CIGS active cell area, then:

$$DA = X * (A_1 + A_2) \tag{4.6}$$

Within the optically optimized S-P structure, we consider the effect of the DA in the total PCE by normalizing it without neglecting the DA. As can be seen in Figure 4.9, under the assumption of a cell larger than 1 cm, the effective loss in PCE is less than 2% even when the separation between P1 and P3, including the width of such laser cuts, is as large as 500 µm. For separations as small as 100 µm, which have been recently outperformed in the series connection of CIGS cells [176], the loss in PCE is negligible.

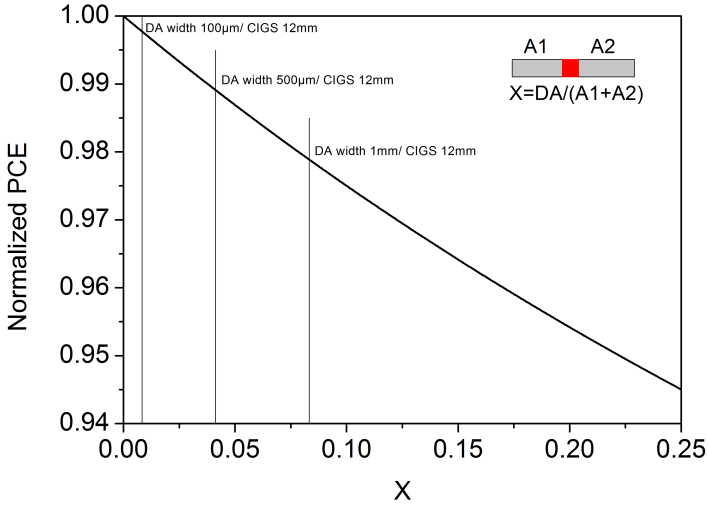

Figure 4.9: PCE as a function of DA width of the serial connected cells assuming devices with an area of 12x12 mm^2.

4.3 Conclusions

In summary, we proposed and studied a new monolithic tandem configuration where the constraint of current density matching is removed. Two CIGS cells laterally connected in series may be connected in parallel with a PVK cell matching the maximum power point voltages. As indicated above, the configuration studied is monolithic but the currents from the top PVK and the bottom CIGS cells can be extracted separately. We demonstrated that when the two cells are electrically separated by a dielectric non-periodic photonic multilayer structure, such photonic structure can be designed to effectively confine the incident sunlight above the PVK band-gap in the PVK absorber layer. The same photonic structure is used to reach an optimal transparency for sunlight below such band-gap and efficiently couple it into the CIGS bottom cell. Using realistic current state of

the art parameters for all layers in the multi-junction architecture, we estimated that PCEs above 28% can be achieved. The PCE of the S-P configuration is for most of the cases studied two percentage points higher in efficiency than the estimated for an optimal series connected standard tandem configuration or the 22.6% and 22.1% which are the maximum efficiencies reported for CIGS and PVK single junction cells, respectively. Any improvement in the sub-cells will further increase the potential efficiency of the S-P cell. For a successful experimental implementation of the S-P configuration, the procedures to fabricate high quality semi-transparent electrodes with the limitations imposed by the layers already deposited must be improved. In addition, the optical optimization of the NDS must be made compatible with its role of preventing short-circuiting between the two sub-cells.

Chapter 5

Semi-transparent Organic Solar Cells

Throughout the work performed during this thesis with multi-junction organic solar cells, we have found a common problem, namely, the development of high quality TEs to be deposited on top of the organic layers. For semi-transparent electrodes deposited on top of the glass substrates, a vast number of possibilities exist. However, not all deposition methods used in most of the high quality TEs are compatible with the fragile nature of the organic films. This represents a major challenge when fabricating regular tandem devices, 4-terminal devices and naturally, single junction semi-transparent solar cells. In the tandem devices, the intermediate electrode functions as an ICL for the recombination of charges, thus requiring less lateral conductivity. In the case of 4-terminal devices or single junction semi-transparent devices, the top TEs should exhibit a good lateral conductivity for the extraction of charges, together with a high level of semi-transparency in the visible range.

Semi-transparency is perhaps one of the characteristics in which organic materials offer a winning solution for future integrated photovoltaics. When com-

pared with other technologies, the almost colorless semi-transparency that can be achieved with some high efficiency polymers is barely obtained with other materials such as, for instance, perovskites or amorphous silicon. For this reason, efforts towards the optimization of semi-transparent OSC are of cumbersome importance in order to be able to launch this technology onto the market.

Several authors have reported their work on semi-transparent OSCs using different top electrodes including thin metallic films [100, 142], silver nanowires (AgNWs) [157, 177, 178], highly conductive PEDOT:PSS formulations [179, 180, 181], graphene [182], Ag nanoparticles ink [183, 184], and hybrid layers [185].

In this chapter, we present our studies towards optimization of semi-transparent devices exploring some of the techniques from the aforementioned for the fabrication of the top TE. These include the evaporation of metallic thin films, the use of AgNWs, and the use of thin metal films combined with microgrids. When using thin evaporated silver films, we perform a wider optical and electrical characterization. We also show the advantages and limitations of the different systems. Our findings point towards an evaporated solution for which we further demonstrate its compatibility with upscaling.

5.1 Device structure with thin silver

PTB7-Th is a high performance polymer material with an absorption maxima located at 700 nm. When mixed with the $PC_{71}BM$, it forms a layer of a neutral color which is ideal for semi-transparent devices. The device architecture of the inverted semi-transparent devices is shown in Figure 5.1. The difference between this and a regular opaque device is introduced in the top electrode, which instead of being a 100 nm silver layer, is formed by a MAM structure using thin silver in between two MoO_3 layers. The photoactive layer is a bulk heterojunction blend consisting of the polymer PTB7-Th or PCE10 as the electron donor and $PC_{71}BM$

as the electron acceptor.

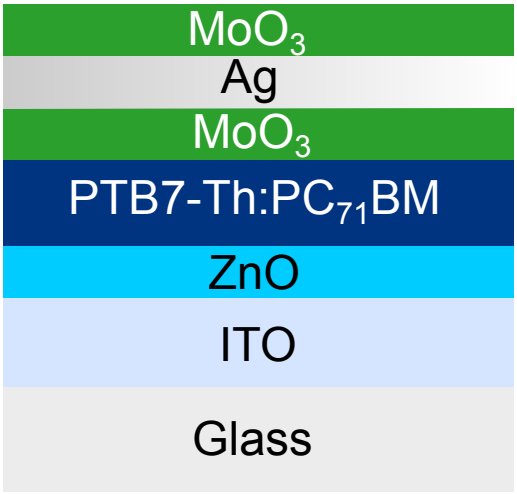

Figure 5.1: Architecture of a PTB7-Th:$PC_{71}BM$ semi-transparent organic solar cell.

5.2 Optical characterization of thin silver layers

The UV–Vis transmission spectra of different thicknesses of Ag films are displayed in Figure 5.2. In all the cases, the films are deposited on top of an eagle glass substrate with 5 nm MoO_3. Simulated transmissions for the films above 5.77 nm when employing the optical constants of the bulk Ag are shown in Figure 5.3. When comparing Figures 5.2 and 5.3, it is observed that as the film gets thicker, its transmission shape resembles the one predicted with the bulk constants, while for the thinner films the shape deviates suggesting a plasmonic behavior. In the latter case, the calculated transmission is overestimated with respect to the actual values. On the other hand, for the 11 and 13 nm films, the actual transmission is higher than the calculated one. This can be explained by the reduction in k that characterizes the thin silver films for the longer wavelengths, as shown previously

in Chapter 3.

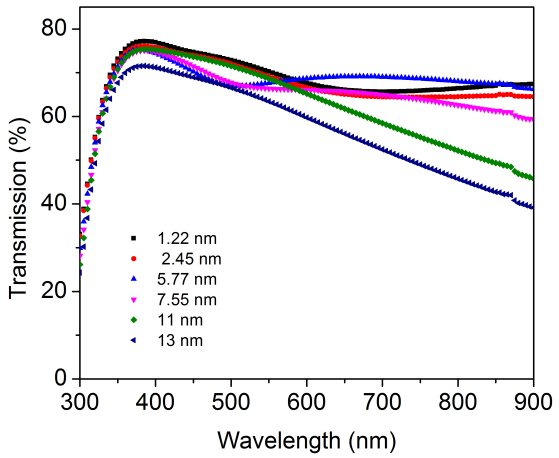

Figure 5.2: Experimental transmission of thin silver films with different thicknesses evaporated on top of a MoO_3 layer of 5 nm.

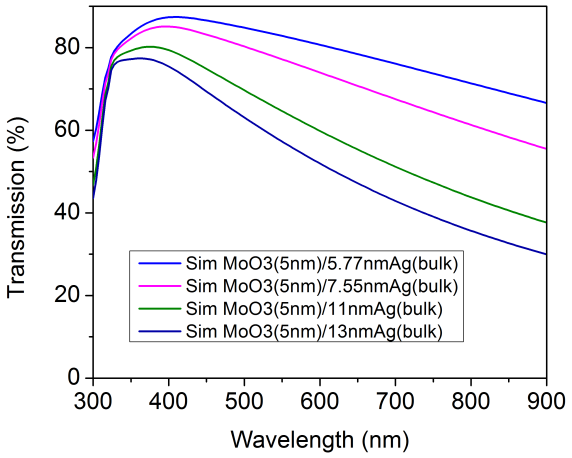

Figure 5.3: Simulated transmission of thin silver films with different thicknesses evaporated on top of a MoO_3 layer of 5 nm using the Ag bulk constants.

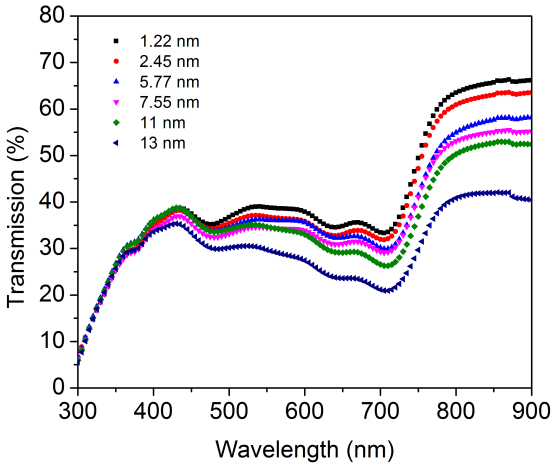

Figure 5.4: Experimental transmission of thin silver layers on top of Glass/ZnO/PTB7-Th:$PC_{71}BM$/MoO_3.

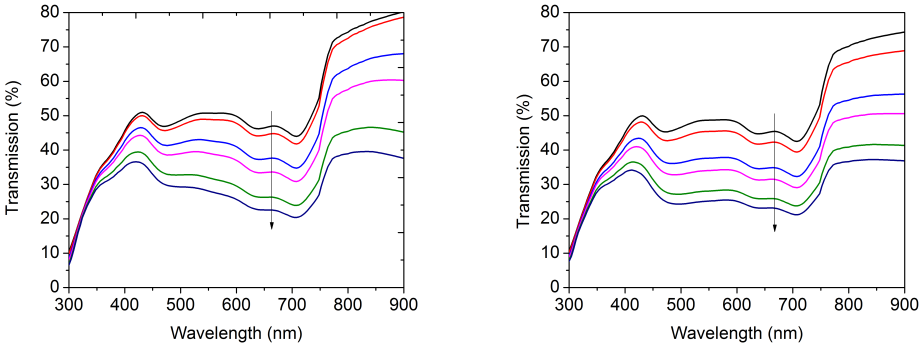

(a) (b)

Figure 5.5: Simulated transmission of thin silver layers on top of Glass/ZnO/PTB7-Th:$PC_{71}BM$ a) using bulk Ag constants, b) using constants measured at ICFO. The arrow indicates the direction of thickness increase. Ag layers were deposited with thicknesses: 1.22 nm, 2.45 nm, 5.77 nm, 7.55 nm, 11 nm, and 13 nm.

Figure 5.4 shows the experimental transmission of the structure Glass/ZnO/PTB7-Th:$PC_{71}BM$/MoO_3/Ag (variable). Figure 5.5 displays the simulated transmissions in the cases where the Ag bulk constants or the Ag thin silver constants measured at ICFO are employed. Similarly to the case of the thin silver deposited on glass, the bulk constants already represent fairly the experimental transmission for the thicker films (above 11 nm), while for thinner layers the modified index is more accurate. For 10 nm layers or thinner, we chose the modified silver constants for all our calculations.

5.3 Electrical characterization of thin silver layers

5.3.1 Sheet resistance of thin silver films

In order to determine what is the minimum thickness of Ag layer that can still exhibit lateral conductivity when measuring with the 4-point method, we deposited thin silver films on top of MoO_3 covered glass. As the growth of silver depends strongly on the seed layer, we also prepared films on top of the blend. All layers, including the thin silver, were prepared following the protocol explained in Appendix section B.4. In the calculation of sheet resistance Rs, we used the resistance obtained from regular IV measurements together with the geometrical characteristics of the samples and inserted them into equation 5.1. The geometrical characteristics are depicted in Figure 5.6.

$$R = Rs * (L/W) \tag{5.1}$$

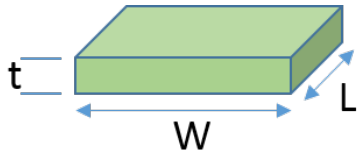

Figure 5.6: Geometrical parameters

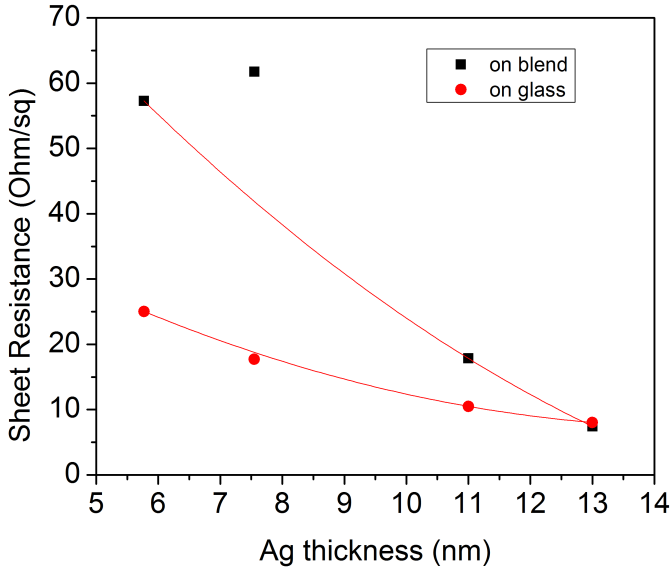

Figure 5.7: Sheet resistance of thin silver films deposited on blend (black squares) and on glass (red circles).

As shown in Figure 5.7, the sheet resistance of the thin silver is sligthly higher for the films deposited on top of the blend. To keep the sheet resistance around values comparables to those of the ITO, the silver film thickness should not decrease much below 11 nm.

5.3.2 PV parameters of semi-transparent solar cells with different Ag thicknesses

Complementary to the fabrication of single thin silver films to study their electrical and optical properties, we fabricated complete semi-transparent solar cells using different Ag thickness at the top electrode to verify their performance. The average PV parameters for the devices are depicted in Table 5.1. Within all semi-transparent electrodes, there is a natural compromise of transparency and electrical resistance. For the semi-transparent solar cells, this compromise implies the determination of a minimun thickness of silver transparent electrode that can still provide a good FF. From the experimental results, we found that when pushing the thickness below 7 nm the losses in FF reached 13% compared to an opaque reference. This significant loss of FF, together with the hindered transmission of very thin Ag layers due to aggregation, suggest that good quality films can be only formed with thicknesses of 10 nm or more. For devices employing a 10 nm silver layer, the efficiency is maintained at 60% of the efficiency of the opaque device, without including a photonic structure.

Table 5.1: Comparison of average PV parameters for semi-transparent solar cells with different thicknesses of top silver electrode + capping MoO_3 using a CB based PTB7-Th:$PC_{71}BM$ blend.

Device	$J_{sc}[mA/cm^2]$	$V_{oc}[mV]$	FF[%]	PCE[%]
4.77 nm	10.05 ± 0.06	789.17 ±2.56	53.31 ± 4.09	4.23± 0.40
6.77 nm	9.26 ± 0.23	801.21 ±1.82	62.27 ± 0.21	4.62± 0.11
10 nm	10.94±0.09	799.47 ± 0.50	66± 0.23	5.77± 0.03
12 nm	11.82±0.11	798.16 ±1.43	64.96± 0.24	6.13± 0.06
Opaque	16.65±0.13	783.02 ±2.10	71.81±1.32	9.36± 0.25

5.3.3 Optical optimization

Similarly to what has been described for previous configurations, for the semi-transparent solar cells we set the optimization target parameters and extract the best solutions out of a large set of calculations. The optimization parameters are the photocurrent together with the average transmission in the visible range. We select a minimum transmission of 26%. With this approach we can derive an architecture that optimizes the efficiency and at the same time guarantees a high transmittance. The freedom allowed within the different layers is restricted to experimental constrains, for instance, the thin silver is not allowed to go below 10 nm, following the experimental results presented in Section 5.3.2.

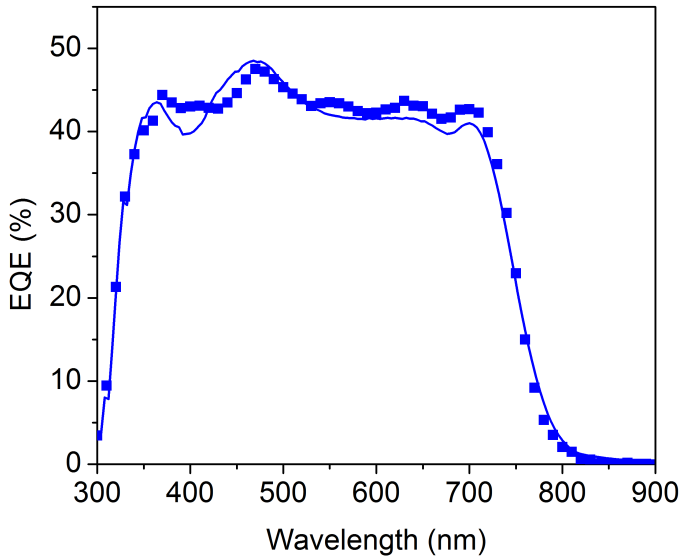

Figure 5.8: Experimental (squares) and simulated (line) EQE of an encapsulated semi-transparent OSC with the architecture (in nm) ITO (135)/ PFN(4)/ PTB7-Th:$PC_{71}BM$(100)/MoO_3(5)/Ag(10)/MoO_3(86).

As shown in Figure 5.8 the simulated EQE results can describe the values obtained experimentally. Althoug, the matching of the experimental and simulated curves for the transmission is not exact, the obtained experimental transmission is around the 30% for the visible wavelengths, as observed in Figure 5.9.

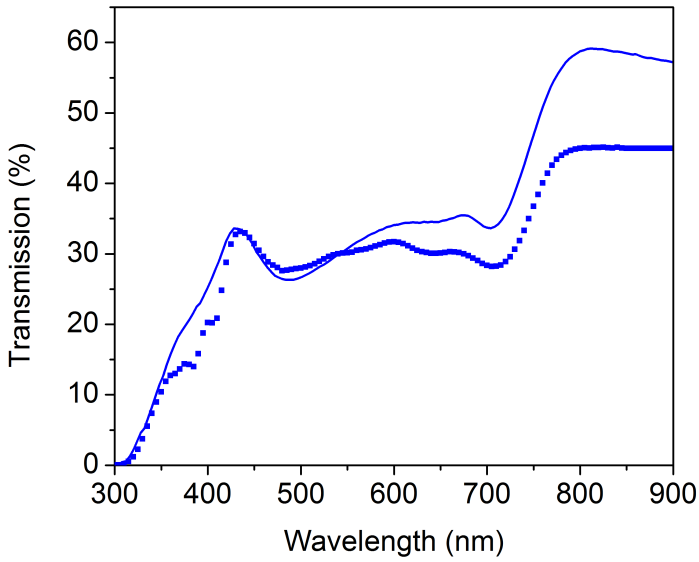

Figure 5.9: Experimental (squares) and simulated (line) transmission of an encapsulated semi-transparent solar cell wih an architecture corresponding to Figure 5.8.

5.4 Microgrids to improve evaporated thin silver quality

From the studies performed in Section 5.3.2 we concluded that thin Ag electrodes below 7 nm were not suitable for the fabrication of semi-transparent solar cells due to FF losses. The problem is aggravated when trying to upscale the devices. In an attempt to increase the conductivity while maintaining the high transparency

of an ultrathin silver electrode with a thickness around 5 nm, we designed a combined structure using the ultrahin silver electrode and a conductive Ag grid on top. The architecture of a semi-transparent device with a top microgrid is depicted in Figure 5.10. The Ag grid was evaporated on the semi-transparent solar cell, using a 4 by 6 mm silver mask with a micrometer grid featuring slots of 10 µm width and a period of 500 µm. Figures 5.11, 5.12 and 5.13 show the geometry of the designed masks. A total of 6 lines with a height of 20 nm were evaporated on top of the thin silver electrode for each solar cell.

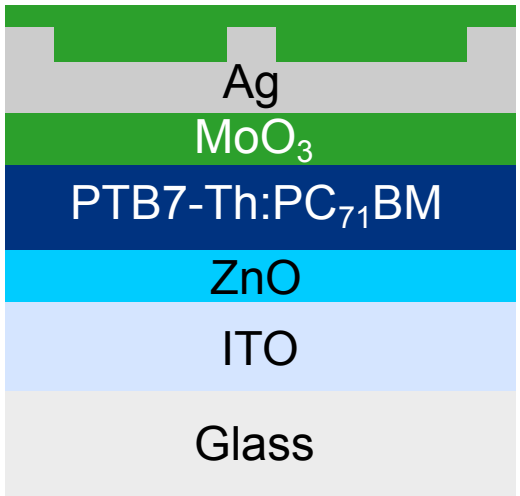

Figure 5.10: Architecture of semi-transparent organic solar cell using top microgrids.

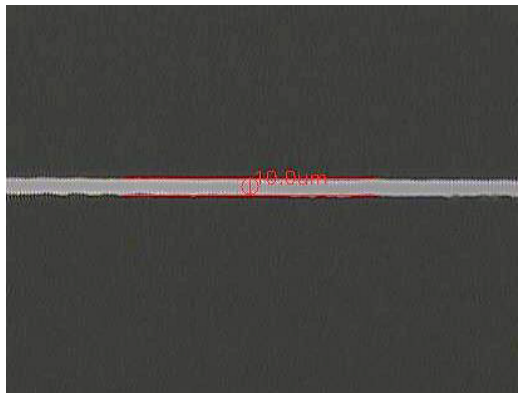

Figure 5.11: Width of grid slot.

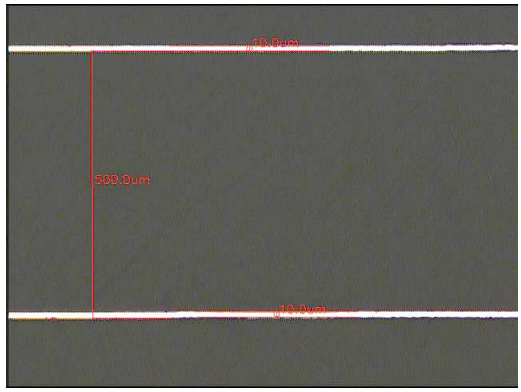

Figure 5.12: Period of grid slots.

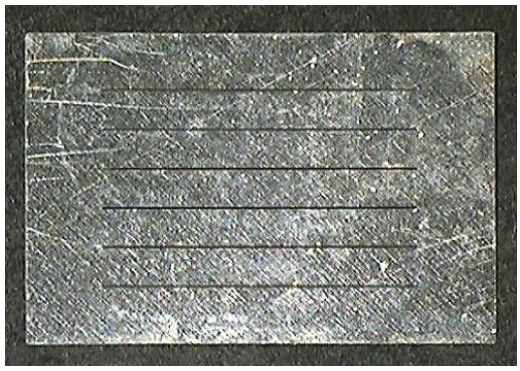

Figure 5.13: View of complete mask with grid.

We observed that using the grid kept the V_{oc} and J_{sc} practically unaffected while recovering the FF from 53 % to 61 %, equivalent to an improvement of 15% (Table 5.2). The resultant FF was, however, rather low compared to the best opaque devices.

Table 5.2: Average PV parameters of thin silver devices with and without top silver grid.

Cell	$J_{sc}[mA/cm^2]$	$V_{oc}[mV]$	$FF[\%]$	$PCE[\%]$
4.77 nm	10.05 ± 0.06	789.17 ±2.56	53.31 ± 4.09	4.23± 0.40
Devices with top silver grid of 20 nm	10.19	805.91	61.07	5.02

5.5 Silver Nanowires (AgNWs)

Significant interest in Ag nanowires (AgNWs) has arisen for their applicability to solution-processed transparent electrodes. In particular, AgNWs present outstanding opto-electronic properties such as a high transmittance of around 90% at 550 nm, combined with a sheet resistance below 20 Ohms/square, being comparable with commercial ITO. A large number of studies have reported the use of AgNWs as bottom electrodes using different blends; however, only a few have

shown the use of AgNWs as top electrodes in semi-transparent solar cells. This application is perhaps the most interesting for AgNWs, given that there exists a wide variety of transparent electrodes that can be deposited on glass but not as top electrodes due to them damaging of the underlying organic layers. To familiarize ourselves with the processability of the AgNWs, we fabricated opaque solar cells with AgNWs in the bottom as depicted in Figure 5.14.

We used AgNWs dissolved in Isopropanol (IPA) from the company Seashell. The average length was in the range of 15 to 30 µm and the average diameter from 15 - 35 nm, as specified by the provider.

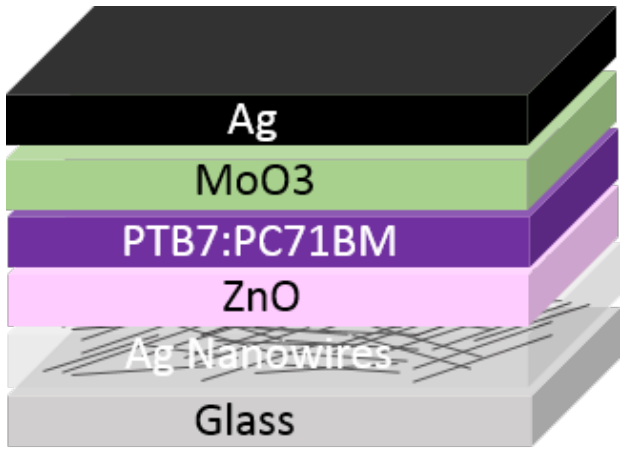

Figure 5.14: AgNWs as bottom electrode in an inverted opaque device configuration using the blend PTB7:$PC_{71}BM$.

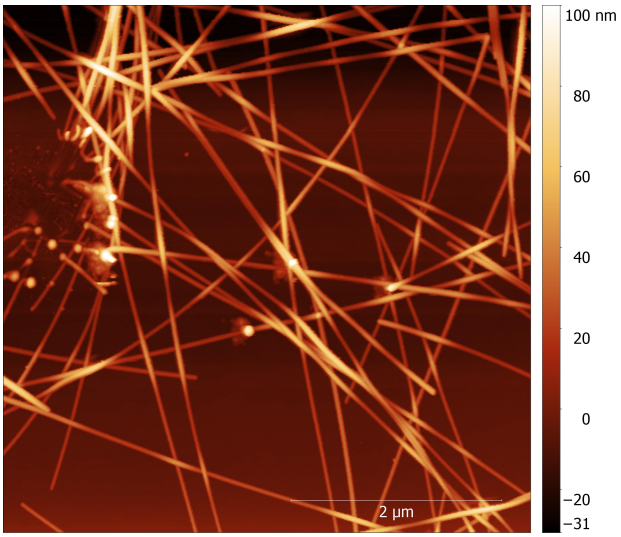

Figure 5.15: AFM image of AgNWs.

Figure 5.15 shows that the AgNWs distribute randomly creating an intermixed network. The denser it is, the higher the conductivity of the film but the lower the transmission. A rather good compromise between sheet resistance and transmission of the AgNWss layers was obtained using 2000 rpm velocity with 10000 rpm/s acceleration, having sheet resistances on the 15 to 20 Ohms/square range on top of glass. The transmission of the AgNWs deposited at 2K rpm is compared to that of a 100 nm ITO in Figure 5.16, showing major differences. A broadband specular high transmittance above 85% is observed for the AgNWs for wavelengths above 400 nm, while for 100 nm commercial ITO, the transmittance is lower for the visible range. The narrow dips of the AgNWs transmittance at around 350 nm are due to the localized surface plasmon resonance [187].

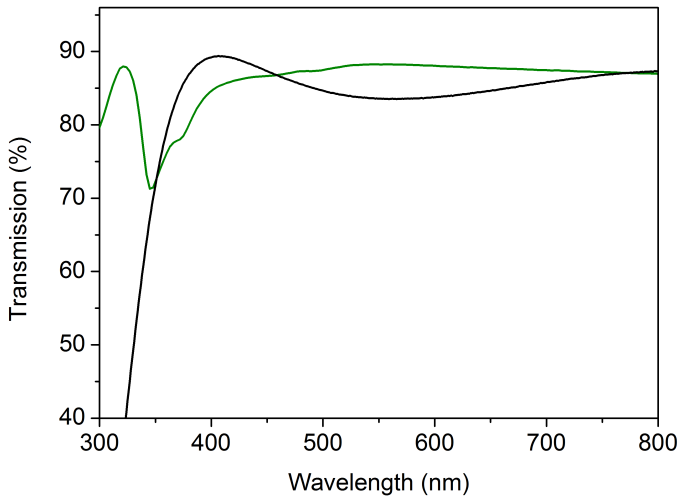

Figure 5.16: Transmission of AgNWs layer deposited at 2K rpm (green line) compared to 100 nm ITO (black line).

Using the regular ZnO thickness (20 to 30 nm) on top of the AgNWs, all the cells were short-circuited. To prevent shunts coming from the superposition of AgNWs, different ZnO thicknesses were tested.

Finally, single junction solar cells were fabricated on top of the AgNWs using thick ZnO layers of around 60 nm and were compared to reference devices with the same ZnO thicknesses. When looking at the PV parameters of the reference devices against the AgNWs devices, the latter perform almost as well (Table 5.3). The J_{sc} and V_{oc} are practically unchanged, while the FF is slightly reduced. Overall, the AgNWs based solar cells reach 95% of the efficiency of the references.

Table 5.3: Performance parameters of reference inverted PTB7:$PC_{71}BM$ devices and with AgNWs as bottom electrode.

Device	$J_{sc}[mA/cm^2]$	$V_{oc}[mV]$	$FF[\%]$	$PCE[\%]$
Reference thick ZnO	12.52 ± 0.12	743.34 ± 1.87	73.17 ± 1.15	6.81 ± 0.17
AgNWs thick ZnO	12.483 ± 0.51	739.20 ± 2.91	70.30± 1.80	6.48± 0.28

As the final goal was to use the AgNWs as top electrodes in a semi-transparent configuration, we fabricated devices using an ITO bottom electrode and finishing with the AgNWs as shown in Figure 5.17.

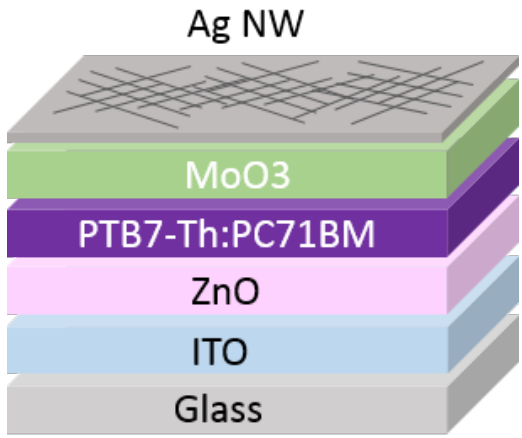

Figure 5.17: Silver Nanowires as top electrodes for semi-transparent organic solar cells.

Depositing the IPA-based AgNWs by spin coating directly on top of the evaporated MoO_3 damaged the cells in all cases. Inverted devices with top AgNWs have typically been fabricated by replacing the MoO_3 with PEDOT:PSS on top of the blend [177]. The annealing required for PEDOT:PSS, however, is harmful to the PTB7-Th:$PC_{71}BM$ blend. Several strategies, including modification of PE-

DOT:PSS to overcome surface energy incompatibilities with the organic blend, together with milder temperature treatments to avoid damaging the active layer, led to low quality reference devices. Sticking to the inverted architecture, we tested the use of an intermediate ultrathin evaporated silver layer to protect the MoO_3. We introduced a 1 nm silver layer, deposited at a rate of 1 Å/s, in between the MoO_3 and the spin coated AgNWs. As a protective layer for the AgNWs, we deposited a ZnO nanoparticles layer of 30 nm on top by spin coating and annealed it for 1 minute at 70°C. The cell area was defined by mechanically scratching.

Table 5.4: Performance parameters of PTB7-Th:$PC_{71}BM$ devices and with AgNWs as top transparent electrode and ZnO capping layer.

Device	$J_{sc}[mA/cm^2]$	$V_{oc}[mV]$	$FF[\%]$	$PCE[\%]$
ITO-AgNWs/ZnO np	10.52±0.28	775.84 ±7.12	60.12 ± 0.99	4.90 ± 0.12

We observed that only 1 nm of evaporated silver was necessary to be effective in preventing the damage to the solar cell when spin coating the AgNWs. The measured EQE for a semi-transparent solar cell employing the combined thin evaporated silver with the AgNWs is displayed in Figure 5.18. When comparing this result with published work, it can be seen that the obtained PCE for a cell of 36% semi-transparency at 550 nm is quite remarkable for devices applying AgNWs.

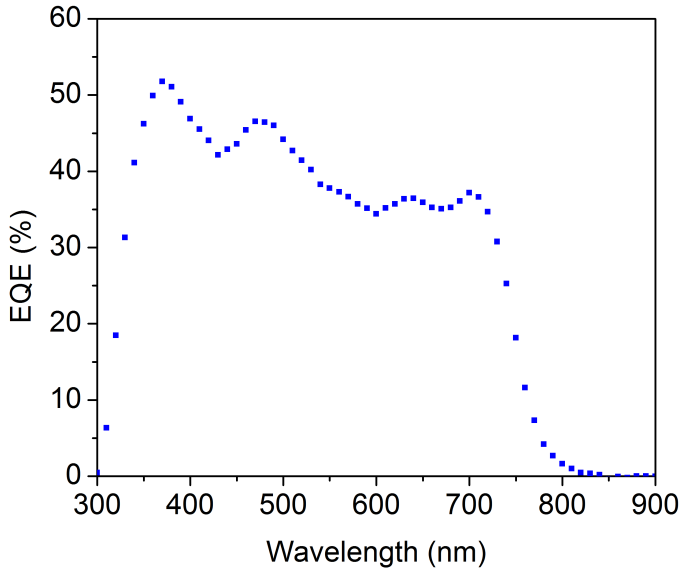

Figure 5.18: Measured EQE of a semi-transparent solar cell with the architecture (layers in nm): ITO(135)/ZnOsg(20)/PTB7-Th:$PC_{71}BM$(100)/MoO_3(5)/Ag(1)/AgNWs.

Table 5.5: Comparison of performance parameters of semi-transparent devices using top AgNWs. The transmission is at 550 nm.

Device	J_{sc} [mA/cm^2]	V_{oc} [mV]	FF [%]	*PCE* [%]	T [%]
AgNW/PEDOT:PSS/pDPP5T-2:PCBM/ZnO np/AgNW [188]	8.48	559	60.22	2.89	56
ITO/ZnO/PCE11:PC71BM:PC61BM/ MoO_3/AgNW+PEDOT:PSS [189]	14.7±0.7	786 ±1	64 ± 1	7.6 ± 1.2	6
ITO/ZnO/PTB7-Th:PC71BM/MoO_3/AgNW + 1nm Evaporated Ag/ ZnO np (this work)	10.5±0.3	775.8 ±7.1	60.1 ± 1	4.9 ± 0.1	36

Nevertheless, this approach would only make sense in a scenario that combined a solution- processed fabrication of organic solar cells with certain vacuum-processed steps. The benefit of such a structure when thinking of an industrial application where AgNWs are employed is that it avoids the use of the water based PEDOT:PSS, which has been shown to accelerate the degradation of solar cells [190].

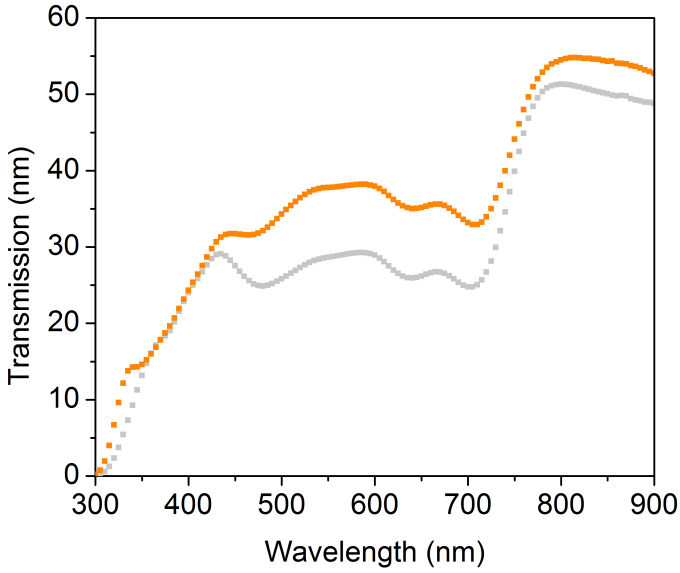

Figure 5.19: Transmission of semi-transparent device (orange squares) using silver nanowires as follows (layers in nm): ITO(100)/ZnOsg (20)/PTB7-Th:$PC_{71}BM$(100)/MoO_3(5)/Ag(1)/AgNWs/ZnOnp(30nm) and (grey squares) ITO(135)/ZnOsg(20)/PTB7-Th:$PC_{71}BM$(100)/MoO_3(5)/Ag(12)/MoO_3(88).

Using the AgNWs, we were able to fabricate devices with a transmission in the visible well above 30%, surpassing the transmission of the semi-transparent devices based solely in thin Ag films, as seen in Figure 5.19. Note that, for the AgNWs based devices we reached a performance comparable to that of 6.77 nm

thick silver films based OSC (refer to Table 5.1) , yet with a higher transmission in the visible. Further increases in the PV parameters like the FF might follow from an improvement in the quality of the AgNWs themselves, from a reduction in impurities, and from a careful optimization of the top spin coated AgNWs, varying concentrations and spin coating conditions. The application of other deposition techniques for the AgNWs are another route towards optimization. On the other hand, improvements in the photocurrent might result from implementation of photonic structures on top, similarly to the case of evaporated silver films.

5.6 Upscaling of semi-transparent organic solar cells

One important step towards the introduction of organic solar cells to the market is demonstrating the scalability of laboratory concepts. Our contribution in this area focused on the study of serial interconnection of semi-transparent solar cells based in the high efficiency blend system PTB7:$PC_{71}BM$. Our group had already established a laser ablation system. The laser source consisted of a Verdi-V6 laser pumping a Mira900-F oscillator, whose laser beam seeds the Legend F amplifier which is pumped by an Evolution laser (Coherent). This system delivered a pulsed laser beam with a power of approximately 1 W, a pulse length of 120 fs, a repetition frequency of 1 kHz and a wavelength of 800 nm. Neutral density (ND) filters were used to attenuate the beam power. A convex and a concave lens were used as inverse beam expanders in order to change the beam diameter to match the aperture of the objective. This objective (10x, 0.25 NA) focused the beam onto the sample for scribing. In order to ablate with a wavelength of 400 nm (800 nm is only weakly absorbed by the absorber blend), a second harmonic generator (SHG) based on a BBO crystal was used.

Figure 5.20 shows the three laser cuts that are necessary to establish a serial

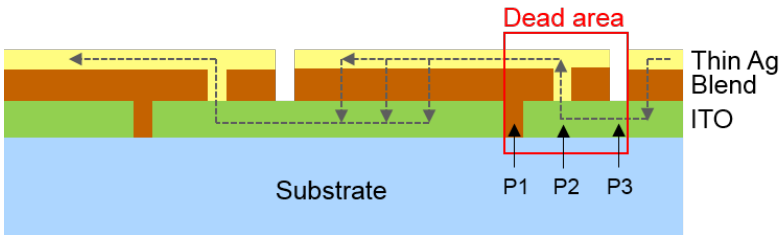

Figure 5.20: Sketcth of laser scribes required for serial connection of semi-transparent solar cells.

connection between the cells. For organic solar cells, the laser scribing is similar to the already discussed case of CIGS and PVK. The first cut is denominated P1 and it scribes both the ITO electrode and the ZnO electron transporting layer. The second cut is denominated P2 and it ablates the organic layer. At this point, it is important to calibrate the laser power such that the organic layer is completely cut but without reaching the ITO below. Finally, P3 scribes the organic layer together with the hole transporting MoO_3 and the thin Ag. Care must be taken to avoid harming the ITO and ZnO layers. The arrows indicate the direction of current flow inside the structure. A dead area is generated in between the P1 and P3 scribes, meaning that such an area is not contributing to photocurrent. In general, it is desired to keep this area as small as possible.

To fabricate serially connected cells, we first deposited ZnO on top of an ITO covered glass substrate, as explained in section **??**. The ITO and ZnO were then laser scribed. The cuts were inspected in situ with a CCD camera and in detail with SEM to verify their quality. After the scribing of P1, the cells were put into the glovebox for deposition of the PTB7:$PC_{71}BM$ blend. Once the drying period under vacuum was finished, the cells were scribed inside a protective, hermetic box which allowed an N_2 flow during the laser scribing. This flow helped to maintain the cell in an inert atmosphere and to remove debris generated during

the scribing process. The laser reached the solar cell layers from the glass side of the substrate. The final cut was performed after the top semi-transparent silver was evaporated. Again, the use of the protective box was intended to prevent any degradation due to humidity and oxygen.

Using the described system we fabricated and characterized serially-connected devices. The PV parameters of working proof of concept devices are shown in Table 5.6. As reference devices we took solar cells of 0.45 cm^2 area. We observed that the serial connected cells had a voltage approaching twice that of the reference device, as expected. The FF of the ablated cells is slightly higher than the reference devices. A smaller J_{sc} is expected from the serial connection.

Table 5.6: Performance parameters of serially connected PTB7:$PC_{71}BM$ semi-transparent devices.

Device	Area $[cm^2]$	$J_{sc}[mA/cm^2]$	$V_{oc}[mV]$	$FF[\%]$	$PCE[\%]$
Big reference	0.45	7.98	744.71	53.99	3.21
Ablated cell including dead area	0.345	2.53	1422.42	54.93	1.98
Ablated cell excluding dead area	0.21	4.16	1422.42	54.93	3.25

Nevertheless, we observed problems in the connections coming mainly from the P2 cut. As observed in Figure 5.21, the ablation of the organic layer leaves protrusions of material on the edges of the cut. The deposition of only 10 nm silver might not sufficient in some cases to coat the agglomerated edges and reach the bottom ITO, as it is required for the serial connection. Although the development of an improved laser scribing method seems necessary to achieve higher cell efficiencies and reproducibility, the results indicate the viability of applying laser scribing to semi-transparent cells with the PTB7:$PC_{71}BM$ system.

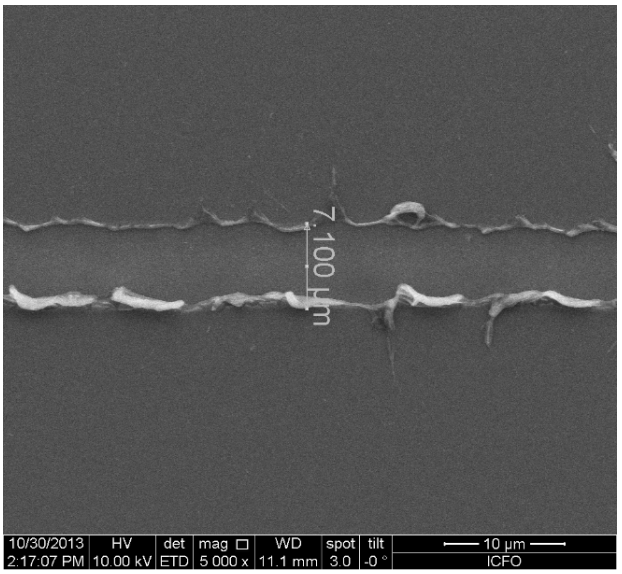

Figure 5.21: SEM image of an ablated organic layer on top of ITO/ZnO.

5.7 Conclusions

Deposition of a high quality semi-transparent electrode on top of the active layer is one of the major challenges within semi-transparent organic solar cells. Several strategies were implemented for the top semi-transparent electrode in order to find the option that would lead to the highest efficiencies. The methods studied included the use of evaporated thin silver layers, a combination of ultrathin silver layers with microgrids and finally, solution-processed AgNWs. We found that AgNWs could provide an outstanding transmission and rather good performance, but their functionality within the device was only guaranteed with an intermediate evaporated 1 nm silver layer. The combined approach using microgrids and thin silver proved effective in improving the conductivity of the thin silver film. The geometry of the microgrid was, however, limited to the fabrication procedure of the masks. Only evaporated grids through a mask were considered so as to avoid any technique that could harm the underlying organic layer. The

improvement in FF that followed the attachment of the microgrids on top of a 4.77 nm thin silver was not yet sufficient to provide the highest efficiency device. We found that the best results for semi-transparent single junction devices were obtained with a layer of thin silver with a minimum thickness of around 10 nm. Such a film could not only provide the highest FF and efficiency, but also complied with the criteria of transmission in the visible, around 30%. In addition, this semi-transparent electrode proved suitable for upscaling, where it was demonstrated that the laser scribing process to serially connect the cells can work with semi-transparent devices employing high efficiency polymers such as PTB7:$PC_{71}BM$.

Chapter 6

Conclusions

In this thesis we examined the enhancements on light harvesting of multi-junction thin film solar cells using the same or complementary absorber materials, to increase the performance of single junction solar cells. For the determination of optimal multi-junction architectures, we employed an inverse integration approach combined with a transfer matrix calculation of the optical electrical field distribution. In addition, to overcome the problem of charge collection within the sub-cells intermediate electrodes, we tested different alternatives compatible to tandem, triple, 4-terminal and to a series-parallel architecture.

In Chapter 2, we described the design of tandem and triple-junction organic solar cells using the blend PTB7:$PC_{71}BM$ with an optimal light absorption within the active layers and complying with the current-matching criteria. The devices were experimentally fabricated, showing, in the case of the tandem architecture, an improvement in the power conversion efficiency of 12% over the single junction device. For the optimized triple-junction solar cell, we achieved a solar-to-hydrogen efficiency of 6%, able to drive a water splitting reaction with minimum electrical losses. We were able to observe how the electrical field distributes among the three sub-cells, showing that each sub-cell has maxima in a different

wavelength portion, irrespective of the fact that the same absorber is employed.

Chapter 3 introduced the study of multi-junction devices in a 4-terminal architecture, where current-matching is no longer mandatory. Using the blend systems PTB7:$PC_{71}BM$ and PTB7-Th:$PC_{71}BM$, we proposed architectures incorporating a dielectric layer in between the sub-cells, operating the devices both electrically connected in series or completely independently. The theoretical photocurrent improvements of the 4-terminal architectures when operated independently over the best single junction device reach the 20% when using silver and 11% when using gold as intermediate electrodes. The numerically calculated trends for the explored 4-terminal architectures were in good agreement with the experimental results, once the right optical constants were employed. Furthermore, in an experimental implementation of the 4-terminal architecture using the blend PTB7-Th: $PC_{71}BM$ with gold intermediate electrodes, we demonstrated that an improvement is indeed obtained in the photocurrent over the best single junction device. This improvement reached a 4% in the photocurrent of the 4-terminal structure compared to the single junction devices. Additional optimization of this architecture is required to maintain the V_{oc} and FF at their reference values.

In Chapter 4, a new multi-junction architecture was theoretically proposed, with the advantages of being monolithic and where the constraint of current density matching is removed. The architecture combines serially connected CIGS solar cells with a parallel connected perovskite cell to match their maximum power point voltages. The structure required the implementation of an inner dielectric, which was properly designed to form a non-periodic photonic structure able to optimize light absorption in the spectrally complementary sub-cells. PCEs above 28% were estimated for this structure, being for most of the cases studied two percentage points higher in efficiency than the estimated for an optimal series

connected standard tandem, and the 22.6 % and 22.1% maximum efficiencies reported for CIGS and PVK single junction cells, respectively.

Finally, in Chapter 5 we explored different semi-transparent electrodes to be deposited on top of organic active layers to implement into multi-junction solar cells. All the studied electrodes were, in principle, compatible with multi-junction architectures, up-scaling and industrial applications. We studied vacuum-processed layers and also solution-processed layers and tested them within single semi-transparent organic solar cells. The selection criteria was that they could provide an average transmission of around 30% while keeping a FF close to the opaque references. We found that such criteria could be met using semi-transparent cells based in thin silver electrodes, which also proved suitable for upscaling by means of laser scribing.

Appendix A

nk coefficients

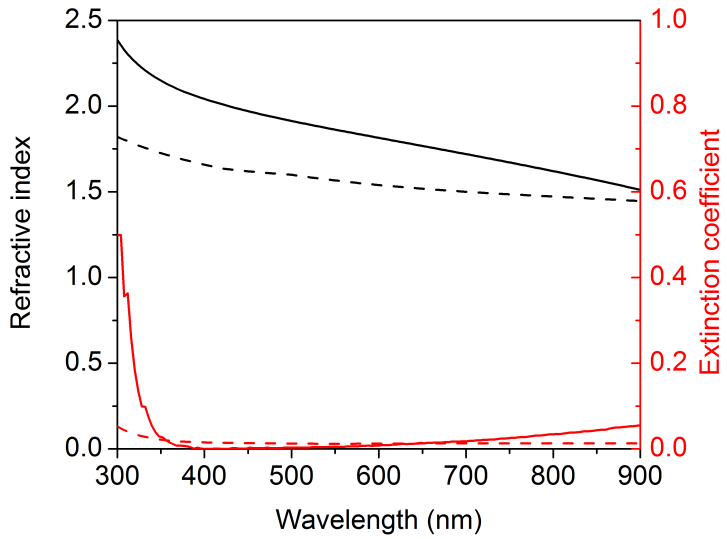

Figure A.1: nk coefficients of ITO (lines) and ZnO (dash)

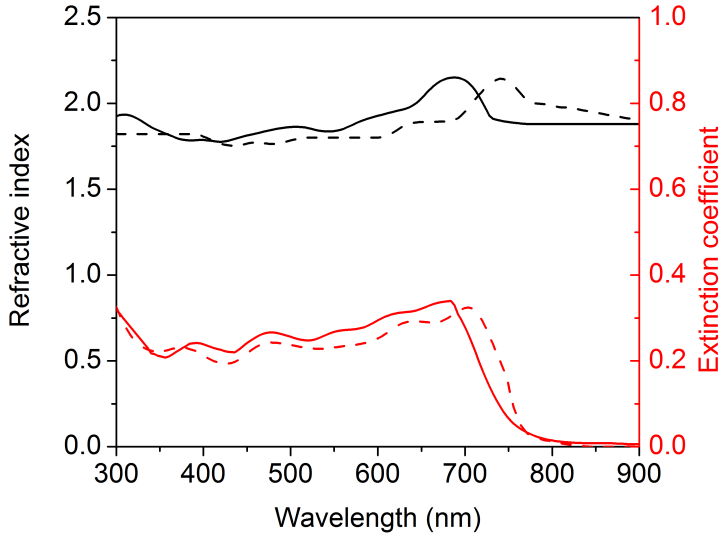

Figure A.2: nk coefficients of PTB7:$PC_{71}BM$ (lines) and PTB7-Th:$PC_{71}BM$ (dash)

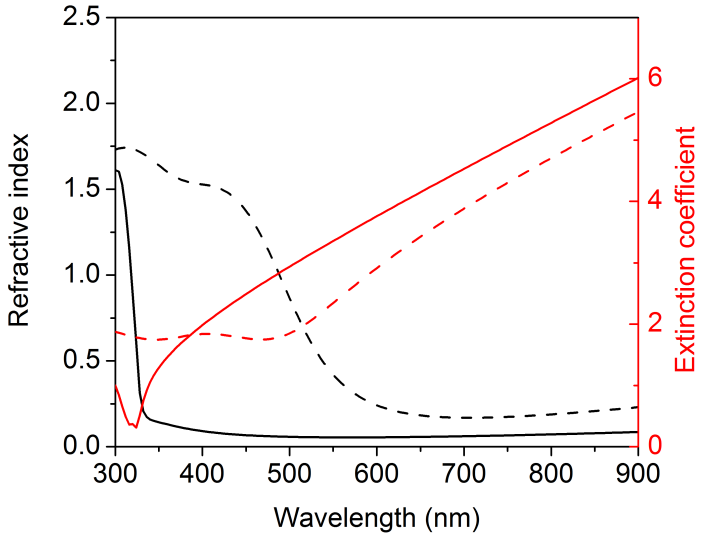

Figure A.3: nk coefficients of Ag (lines) and Au (dash)

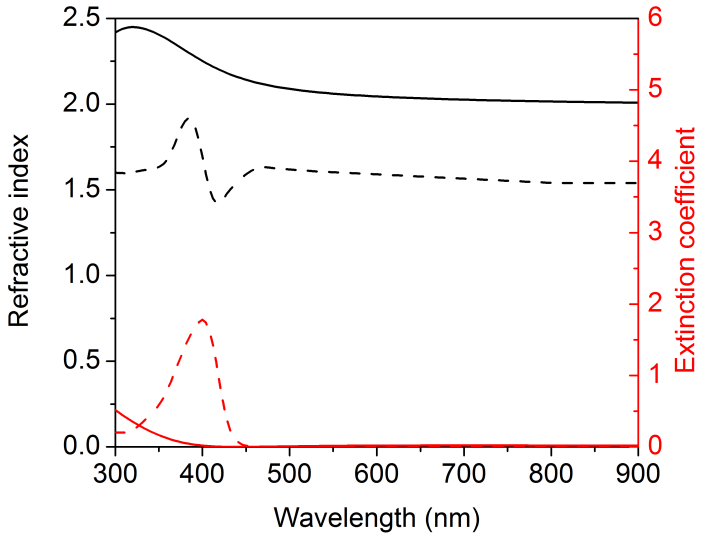

Figure A.4: nk coefficients of MoO_3 (lines) and PFN (dash)

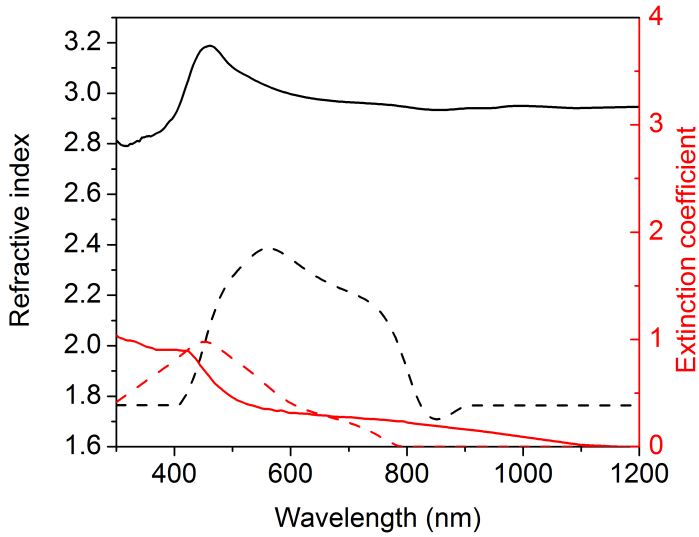

Figure A.5: nk coefficients of CIGS (lines) and PVK (dash)

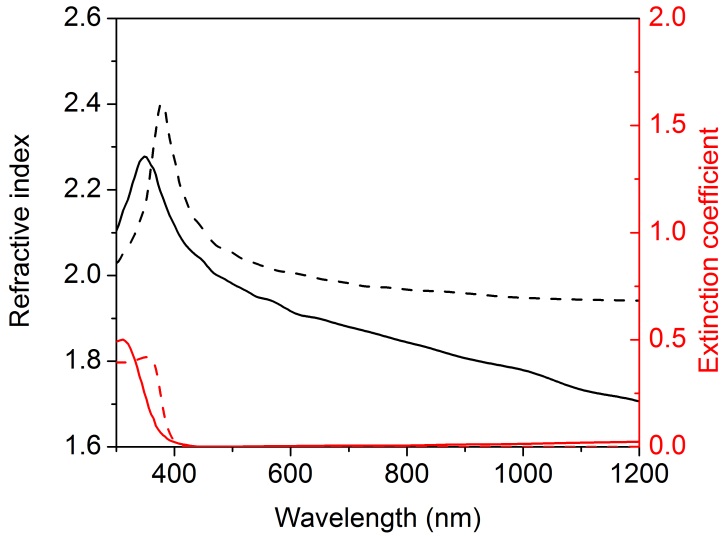

Figure A.6: nk coefficients of AZO (lines) and iZO (dash)

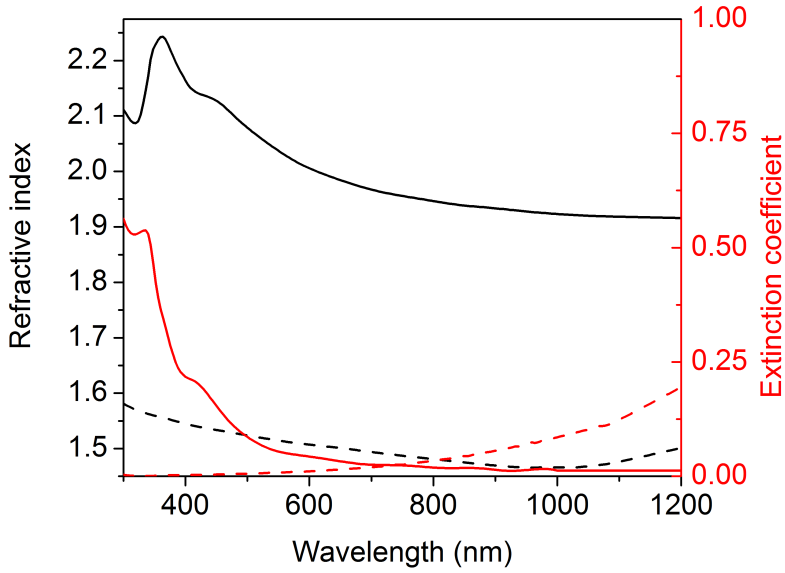

Figure A.7: nk coefficients of $PC_{61}BM$ (lines) and PEDOT:PSS (dash)

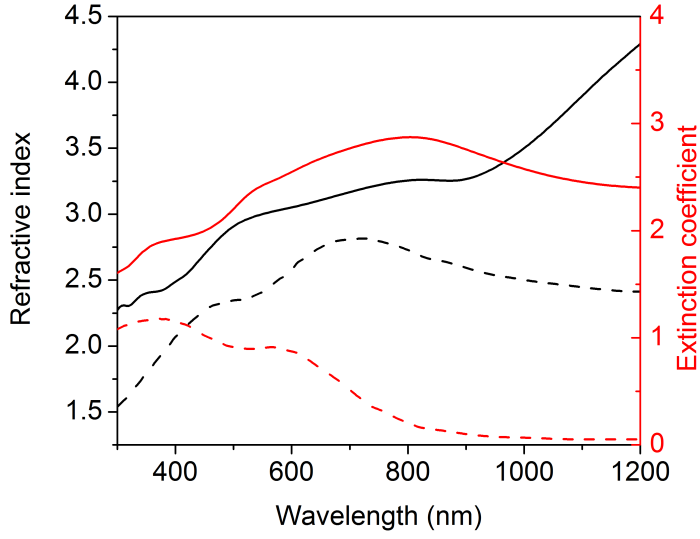

Figure A.8: nk coefficients of Mo (lines) and MoSe (dash)

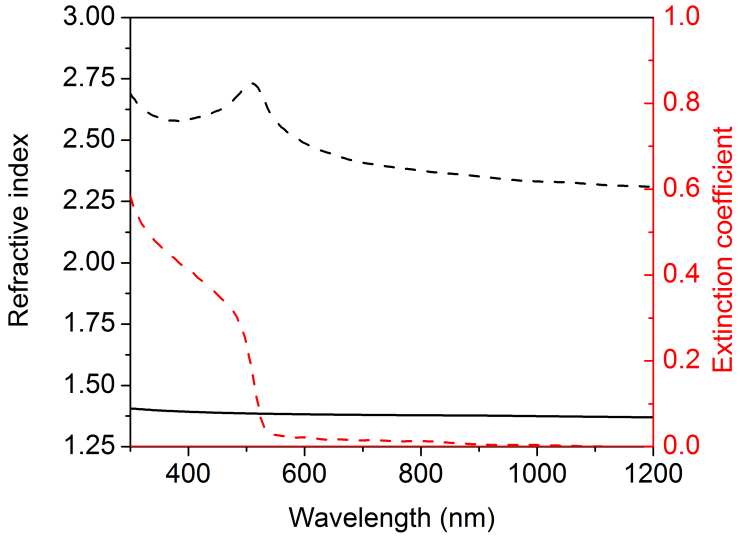

Figure A.9: nk coefficients of MgF_2 (lines) and CdS (dash)

Appendix B

Experimental procedures

B.1 Fabrication of single, tandem and triple solar cells with PTB7:$PC_{71}BM$

The polymers PTB7 and PFN were purchased from the company 1-Material. The fullerene $PC_{71}BM$ was purchased from American Dye Source (ADS). Other materials such as the ZnO precursor based in zinc acetate, was purchased from Sigma Aldrich. Materials for evaporation such as the pellets for MoO_3 and Ag were purchased from Kurt Lesker. No further purification treatments were performed on the materials. The precursor for the solgel ZnO was prepared by dissolving zinc acetate dehydrate (Zn(CH3COO)22H2O, Aldrich, 99.9%, 1 g) and ethanolamine (NH2CH2CH2OH, Aldrich, 99.5%, 0.28 g) in 2-methoxyethanol (CH3OCH2CH2OH, Aldrich, 99.8%, 10 mL) and stirring for at least 12 h [186]. The PFN was prepared at a concentration of 1mg/mL, in methanol. Both ZnO and PFN acted as electron transporting layers. The blend of PTB7:$PC_{71}BM$ was prepared at a concentration of 10 mg/mL (1:1.5), dissolved in chlorobenzene (CB). It was left to stirring for at least 12 hours at 60°C. 3% vol of 1,8-Diiodooctane (DIO) was added at least 1 hour prior blend deposition. For the

single devices, a layer of ZnO or PFN was deposited by spin coating on top of the ITO patterned substrates (15 Ohms/sq). The ZnO was spin coated at around 4000 rpm/s on the ITO and annealed at 150°C for 10 min. PFN was deposited at 5000 rpm/s. The blend was deposited at 1800 rpm by dynamic spin coating inside the glovebox. The samples were then left to dry in vacuum for 1 hour before evaporation. 3 nm of MoO_3, followed by 100 nm of Ag were deposited at rates 0.5 Å/s and 1 Å/s, respectively. In the case of tandem devices, after blend deposition, the ICL was fabricated by thermal evaporation of 7 nm of MoO_3 and 0 to 2 nm of Ag followed by the spin coating of the PFN layer inside the glovebox. A second active layer was deposited on top of the ICL and left to dry in vacuum for an hour. The tandem device was then finished similar to the case of the single junction cells.

For the triple junction devices, the materials were similar except for the used ZnO. In this case, ZnO nanoparticles (N-10, 6083, 2.5 wt % in isopropyl alcohol) from Nanograde were diluted with isopropyl alcohol (1:1, vol%) before use. Recipe for PTB7:$PC_{71}BM$ preparation was as described for the tandem devices. PFN was dissolved in methanol (1.0 mg/ml) in the presence of a small amount of acetic acid (10 µm/ml), which was filtered with a 0.45 µm PTFE filter prior to use. The triple junction devices were fabricated by spin casting ZnO solution on the precleaned ITO patterned glass substrates (Lumtec, 15 Ohms/sq) and annealing at 120°C in the glovebox for 10 min to form a 20 nm electron transporting layer. The active layer of the front subcell (60 nm) was then spin coated on the ZnO surface and the films were dried under high vacuum for 1 h. Afterwards, an ICL similar to the case of the tandem was deposited, composed by MoO_3 (10 nm, 0.5 Å/s), ultrathin Ag (0.5 nm, 0.2 Å/s) and PFN (10 nm). Then, the active layer of the middle subcell (105 nm) was spin coated on the PFN surface, dried in vacuum for 1 h. The second ICL was deposited using exactly the same procedure as the first one. The active layer of the rear subcell (110 nm) was deposited on

top of the second ICL and again left to dry in vacuum for 1 h. Finally, MoO3 (5 nm, 0.5 Å/s) and Ag (150 nm, 1.0 Å/s) electrodes were sequentially deposited through a shadow mask by thermal evaporation, which defined the device area of 9.0 mm^2. The triple-junction solar cells were encapsulated with glass slides using a UV-curable epoxy (ELC- 4908, Electro-Lite Corp) in a N_2 glovebox before testing in ambient air.

B.2 Fabrication of 4-Terminal devices with PTB7:$PC_{71}BM$

Commercial one-sided patterned ITO substrates were covered on the other substrate side with ITO layers deposited by RF sputtering. The bi-coated ITO substrates were solvent cleaned and treated with ultraviolet-ozone for 10 min on each side. Fabrication of the bi-coated cells was successfully carried out without damaging any of the two sides using a lightweight aluminum holder specially designed for the bifacial spin coating processes. The lightweight holder prevented any scratches on the deposited films by holding the samples only from the edges during spin coating. Additionally, to further protect the top and bottom surfaces, vertical sample holders instead of Petri dishes were used during the transportation of the substrates through the different processing steps.

Sol gel ZnO, prepared as explained in section B.1 was spin coated on the ITO and annealed at 150°C for 10 min. The process was repeated for the other side of the ITO substrate, obtaining 30 nm thickness films. The samples were then transferred into a glovebox for further fabrication steps. An active layer of PTB7:$PC_{71}BM$, prepared as in B.1, was spin coated on one side of the ITO bi-coated substrate. The active layer of 90 nm was left to dry in vacuum for 1 h, followed by the evaporation of MoO_3 and a thick Ag electrode. After removing the samples out of the evaporation chamber, a second active layer of 90 nm was

spin coated on the other side of the substrate and left to dry in vacuum for 1 h. A 3 nm MoO_3 layer was deposited prior to the evaporation of a thin Ag layer at a 6 Å/s rate using a homemade holder cooled down to -5°C. To finish the structure, another layer of MoO_3 was deposited on top of the device at a rate of 1 Å/s . The last three layers formed the MoO_3 /Ag (10 nm)/ MoO_3 (MAM) electrode with a four point probe measured sheet resistance of 7 ohms/square. The subcells were then removed from the inert atmosphere to be externally connected in series and characterized in air.

B.3 Fabrication of 4-Terminal devices with PTB7-Th:$PC_{71}BM$

PTB7-Th was purchased from 1-Material. The epoxy NOA65 was purchased from Norland Products. Evaporation Au pellets were purchased from Kurt Lesker. The blend of PTB7-Th:$PC_{71}BM$ was prepared at a concentration of 10 mg/mL (1:1.5) dissolved in CB and left to stirring for 12 h at 60°C . ZnO sol gel was prepared as explained in section B.1 and further diluted to reach a solution of 0.3M (400 mg of Zinc Acetate per 6mL of Methoxyethanol). ZnO was spin coated at 5000 rpm on top of pre-cleaned patterned ITO substrates with a sheet resistance of 15 Ohms/square. The layer was annealed at 150°C for 10 min. 3% volume DIO was added to the blend of PTB7-Th:$PC_{71}BM$ at least one hour prior to deposition. The solution was left to cool down at room temperature and then it was deposited at 2100 rpm by dynamic spin coating inside the glovebox. Then, it was left to dry in vacuum for 1 hour. A layer of 5 nm of MoO_3 was evaporated at 0.5 Å/s followed by a thin silver layer of around 10 nm, evaporated at a 6 Å/s rate using a homemade holder cooled down to -5°C. Thick silver contacts were evaporated at 6 Å/s on the edges of the semi-transparent electrodes to improve the contacts. A layer of 65 nm of MoO_3 was evaporated on top at 1 Å/s. Subsequently, NOA65

was deposited inside the GB using a two step spin coating rate of 500 rpm for 20 secs and then 2000 rpm for 30 seconds. The layer was cured for 8 minutes under UV light. A thin layer of 5 nm was further evaporated on the NOA65 layer. The second silver layer was evaporated under the same conditions as the first thin silver. Then, PFN at a concentration of 1 mg/mL was deposited at 3000 rpm by static spin coating on top of the substrates. The second active layer was spin coated at 2.1K rpm using dynamic spin coating and left to dry in vacuum for at least 1 hour. To finish the devices, a layer of 5 nm MoO_3 followed by 150 nm Ag were evaporated at 1 Å/s.

Devices employing Au were prepared in a similar fashion as devices based in Ag. For deposition of the Au thin layers, the cooling system was also employed, with an evaporation rate of 2 Å/s.

B.4 Fabrication of semi-transparent devices

The fabrication of such devices started with patterned ITO-glass with a sheet resistance of 15 Ohms/square. The ZnO and first layer of MoO_3 used as electron transport and hole transport layers respectively, as their energetic levels match accordingly to the PTB7-Th and PCBM. The procedure for preparation and deposition of the sol-gel ZnO are as explained in B.1. An active layer of PTB7-Th:$PC_{71}BM$, at a concentration of 10 mg/mL (1:1.5) dissolved in CB or 10 mg/mL (1:2) dissolved in DCB, was spin coated on the ITO substrate. The CB based blend was deposited at a rate of 1900 rpm while the DCB based blend was deposited at 1200 rpm to form a layer of approximately 100 nm in both cases. 3% v/v dioodoctane (DIO) was added to the blend solution with CB at least 1 h before spin coating. The active layer was left to dry in vacuum for 1 h, followed by the evaporation of 8 nm MoO_3 and the thin Ag electrode at a 6Å/s rate using a MiniSpektros system from Lesker and a homemade holder cooled down to -5°C.

Different thicknesses of Ag were studied. To finish the structure, another layer of MoO_3 was deposited on top of the device at a rate of 1Å/s. Thick silver was then deposited on the edges of the thin silver, outside the cell area, in order to strengthen the contacts. In some cases, the cells were encapsulated inside the glovebox using a UV curable epoxy. The active area was between 0.06 and 0.09 cm^2, which was determined by the overlap between the ITO and the thin silver.

B.5 Measurements and characterization

Current-voltage characteristics of the solar cells were measured under 1 sun AM 1.5 G simulated sunlight (ABET Sol3A, 1000 W/m^2) with a Keithley 2420 source measurement unit. The illumination intensity of the light source (Xenon lamp, 300 W, USHIO) was determined using a Hamamatsu monocrystalline silicon reference cell calibrated by ISE Fraunhofer. EQEs were measured using a QEX10 Quantum Efficiency Measurement System from PV Measurements. The light transmission spectra for the fabricated devices were recorded using an UV-Vis near IR spectrophotometer (Lambda950, PerkinElmer). For the morphology and thickness studies, a Veeco Dimension 3100 AFM operated under ambient conditions in tapping mode was used. A scratching technique was used for accurate measurements of layer thicknesses.

Bibliography

[1] J.-M. Barnola, D. Raynaud, et al. Historical CO_2 record from the Vostok ice core. In Trends: A Compendium of Data on Global Change. Carbon Dioxide Information Analysis Center, Oak Ridge National Laboratory, U.S. Department of Energy, Oak Ridge, Tenn., U.S.A, 2003.

[2] http://climate.nasa.gov/scientific-consensus/

[3] J. M. Melillo, T.C. Richmond, G. W. Yohe. Climate Change Impacts in the United States: The Third National Climate Assessment. U.S. Global Change Research Program. Eds., 2014.

[4] http://ec.europa.eu/clima/policies/international/negotiations/paris /index_en.htm

[5] Instituto para la Diversificación y Ahorro de la Energía (IDAE). Ministerio de industria, energía y turismo. Informe estadístico energías renovables 2015. http://informeestadistico.idae.es/t1.htm

[6] K. Kurowska, H. Kryszk, E. Kitelinska. Photovoltaics as an Element of Intelligent Transport System Development. Paper presented at the Symposium GIS Ostrava 2014 on Geoinformatics for Intelligent Transportation 2014, Ostrava, Czech Republic, 27-29 June.

[7] B. Burger, K. Kiefer, C. Kost, S. Nold, S. Philipps, R. Preu, et al. https://www.ise.fraunhofer.de/de/downloads/pdf-files/aktuelles/photovoltaics-report-in-englischer-sprache.pdf. Photovoltaics Report. Fraunhoffer Institute for Solar Energy Systems, ISE and PSE AG Freiburg. 17, November 2016.

[8] D. Compaaan, J.R. Sites, et al. Critical Issues and Research Needs for CdTe-Based Solar Cells. Paper presented at the Electrochemical Society Symposium Proceedings vol 99-11, Photovoltaics for the 21st Century 1999, Seattle, USA.

[9] G. Conibeer. Third-Generation Photovoltaics. Materials Today 2007, 10, 42-50.

[10] http://www.nrel.gov/ncpv/

[11] M. Scharber, N. Sariciftci. Efficiency Of Bulk-Heterojunction Organic Solar Cells. Progress in Polymer Science 2013, 38, 1929-1940.

[12] S. Berny, N. Blouin, et al. Solar Trees: First Large-Scale Demonstration Of Fully Solution Coated, Semitransparent, Flexible Organic Photovoltaic Modules. Advanced Science 2015, 3, 1500342.

[13] J. Myers, W. Cao, et al. A Universal Optical Approach To Enhancing Efficiency Of Organic-Based Photovoltaic Devices. Energy & Environmental Science 2012, 5, 6900.

[14] W. Cao, J. Myers, et al. Enhancing Light Harvesting In Organic Solar Cells With Pyramidal Rear Reflectors. Applied Physics Letters 2011, 99, 023306.

[15] M. Niggemann, M. Glatthaar, et al. Functional Microprism Substrate For Organic Solar Cells. Thin Solid Films 2006, 511-512, 628-633.

[16] Y. Zhou, F. Zhang, et al. Multifolded Polymer Solar Cells On Flexible Substrates. Applied Physics Letters 2008, 93, 033302.

[17] Y. Liu, J. Zhao, et al. Aggregation And Morphology Control Enables Multiple Cases Of High-Efficiency Polymer Solar Cells. Nature Communications 2014, 5, 5293.

[18] L. Dou,W.-H. Chang, et al. A Selenium-substituted Low-bandgap Polymer with Versatile Photovoltaic Applications, Adv. Mater. 2013, 25, 825–831.

[19] W. Li, K. Hendriks, et al. Diketopyrrolopyrrole Polymers For Organic Solar Cells. Accounts of Chemical Research 2016, 49, 78-85.

[20] H. Lu, J. Zhang, et al. Ternary-Blend Polymer Solar Cells Combining Fullerene And Nonfullerene Acceptors To Synergistically Boost The Photovoltaic Performance. Advanced Materials 2016, 28, 9559-9566.

[21] L. Lu, M. Kelly, et al. Status And Prospects For Ternary Organic Photovoltaics. Nature Photonics 2015, 9, 491-500.

[22] W. Zhao, D. Qian, et al. Fullerene-Free Polymer Solar Cells With Over 11% Efficiency And Excellent Thermal Stability. Advanced Materials 2016, 28, 4734-4739.

[23] Y. Lin, Z. Zhang, et al. Zhan. High-Performance Fullerene-Free Polymer Solar Cells With 6.31% Efficiency. Energy Environ. Sci. 2015, 8, 610-616.

[24] R. a J. Janssen, J. Nelson. Factors Limiting Device Efficiency in Organic Photovoltaics, Adv. Mater. 2013, 25, 1847–1858.

[25] V. Coropceanu, J. Cornil, et al. Charge Transport in Organic Semiconductors, Chem. Rev. 2007, 107, 926–952.

[26] J. Peet, L. Wen, et al. Bulk heterojunction Solar Cells with Thick Active Layers and High Fill Factors Enabled by a Bithiophene-co-thiazolothiazole Push-Pull Copolymer, Appl. Phys. Lett. 2011, 98, 043301.

[27] A. Kojima, K. Teshima, et al. Organometal Halide Perovskites as Visible-Light Sensitizers for Photovoltaic Cells. J. Am. Chem. Soc. 2009, 131, 60506051.

[28] H. Kim, et al. Lead Iodide Perovskite Sensitized All-Solid-State Submicron Thin Film Mesoscopic Solar Cell with Efficiency Exceeding 9%. Sci. Rep. 2012, 2, 591.

[29] M. M. Lee, J. Teusche, et al. Efficient Hybrid Solar Cells Based on Meso-Superstructured Organometal Halide Perovskites. Science 2012, 338, 643647.

[30] M. Liu, M.B. Johnston, H.J. Snaith. Efficient planar heterojunction perovskite solar cells by vapour deposition. Nature 2013, 501, 395398.

[31] N.J. Jeon, et al. Solvent Engineering for High-Performance Inorganic-Organic Hybrid Perovskite Solar Cells. Nat. Mater. 2014, 13, 897903.

[32] W.S. Yang, et al. High-Performance Photovoltaic Perovskite Layers Fabricated Through Intramolecular Exchange. Science 2015, 348, 12341237.

[33] H. Jung, N. Park. Perovskite Solar Cells: From Materials To Devices. Small 2015, 11, 2-2.

[34] M. Green, A. Ho-Baillie, H. Snaith. The Emergence Of Perovskite Solar Cells. Nature Photonics 2014, 8, 506-514.

[35] M. Saliba, T. Matsui, et al. Cesium-containing Triple Cation Perovskite Solar Cells: Improved Stability, Reproducibility and High Efficiency. Energy Environ. Sci. 2016, 9, 1989-1997.

[36] S. D. Stranks, H. J. Snaith. Metal-halide Perovskites for Photovoltaic and Light-emitting Devices, Nat. Nanotechnology 2015.

[37] J.H. Noh, S.H. Im, et al. Chemical Management for Colorful, Efficient, and Stable Inorganic-Organic Hybrid Nanostructured Solar Cells. Nano Lett., 2013, 13 (4), pp 1764-1769.

[38] S. Kulkarni, T. Baikie, et al. Band-Gap Tuning Of Lead Halide Perovskites Using A Sequential Deposition Process. J. Mater. Chem. A 2014, 2, 9221-9225.

[39] D. P. McMeekin, G. Sadough, et al. A Mixed-cation Lead Mixed-halide Perovskite Absorber for Tandem Solar Cells, Science 2016, Volume 351, 6269, 151–155.

[40] G. E. Eperon et al. Perovskite-perovskite Tandem Photovoltaics with Optimized Bandgaps, Science 2016, 10.1126/science.aaf9717.

[41] T. Todorov, T. Gershon, et al. Monolithic Perovskite-CIGS Tandem Solar Cells Via In Situ Band-gap Engineering. Advanced Energy Materials 2015, 5, 1500799.

[42] C.Bailie, M. Christoforo, et al. Semi-Transparent Perovskite Solar Cells For Tandems With Silicon And CIGS. Energy Environ. Sci. 2015, 8, 956-963.

[43] P. Löper, S. Moon, et al. Organic-Inorganic Halide Perovskite/Crystalline Silicon Four-Terminal Tandem Solar Cells. Phys. Chem. Chem. Phys. 2015, 17, 1619-1629.

[44] F. Fu, T. Feurer, et al. Low-Temperature-Processed Efficient Semi-Transparent Planar Perovskite Solar Cells For Bifacial And Tandem Applications. Nature Communications 2015, 6, 8932.

[45] L. Kranz, A. Abate, et al. High-Efficiency Polycrystalline Thin Film Tandem Solar Cells, J. Phys. Chem. Lett. 2015, 6, 2676-2681.

[46] J. P. Mailoa, C. D. Bailie, et al. A 2-Terminal Perovskite/Silicon Multijunction Solar Cell Enabled By A Silicon Tunnel Junction. Appl. Phys. Lett. 2015, 106, 121105.

[47] K. A. Bush, C. D. Bailie, et al. Thermal And Environmental Stability Of Semi-Transparent Perovskite Solar Cells For Tandems Enabled By A Solution-Processed Nanoparticle Buffer Layer And Sputtered ITO Electrode. Adv. Mater. 2016, 28 , 3937.

[48] S. Albrecht, M. Saliba, et al. Monolithic Perovskite/Silicon-Heterojunction Tandem Solar Cells Processed At Low Temperature. Energy Environ. Sci. 2016, 9, 81-88.

[49] B. Chen, Y. Ba, et al. Efficient Semitransparent Perovskite Solar Cells For 23.0%-Efficiency Perovskite/Silicon Four-Terminal Tandem Cells. Advanced Energy Materials 2016, 6, 1601128.

[50] O. Graydon. View from... PSCO 2016: The race for tandems. Nature Photonics 2016, 10, 754755.

[51] P. Jackson, R. Wuerz, et al. Effects of Heavy Alkali Elements in Cu(In,Ga)Se2 Solar Cells with Efficiencies up to 22.6%. Phys. Status Solidi RRL 2016, 10, No. 8, 583586.

[52] X. Liu, Y. Feng, et al. The Current Status And Future Prospects Of Kesterite Solar Cells: A Brief Review. Progress in Photovoltaics: Research and Applications 2016, 24, 879-898.

[53] S. Delbos. Këwhile Thin Films For Photovoltaics : A Review. EPJ Photovoltaics 2012, 3, 35004.

[54] W. Wang, M. Winkler, et al. Device Characteristics Of CZTsSe Thin-Film Solar Cells With 12.6% Efficiency. Advanced Energy Materials 2013, 4, 1301465.

[55] E.H. Sargent. Infrared Photovoltaics Made by Solution Processing. Nat. Photon. 2009, 3, 325331.

[56] H.W. Hillhouse, M.C. Beard. Solar Cells from Colloidal Nanocrystals: Fundamentals, Materials, Devices, and Economics. Curr. Opin. Colloid Interface Sci. 2009, 14, 245 259.

[57] G. Carey, A. Abdelhady, et al. Colloidal Quantum Dot Solar Cells. Chemical Reviews 2015, 115, 12732-12763.

[58] M. Bernechea, N. Miller, et al. Solution-Processed Solar Cells Based On Environmentally Friendly $AgBiS_2$ Nanocrystals. Nature Photonics 2016, 10, 521-525.

[59] M. Yuan, M. Liu, E. Sargent. Colloidal Quantum Dot Solids For Solution-Processed Solar Cells. Nature Energy 2016, 1, 16016.

[60] M. Ma. Kim, D. Ma. Quantum-Dot-Based Solar Cells: Recent Advances, Strategies, And Challenges. The Journal of Physical Chemistry Letters 2015, 6, 85-99.

[61] A. Bosio, G. Rosa, et al. How The Chlorine Treatment And The Stoichiometry Influences The Grain Boundary Passivation In Polycrystalline Cdte Thin Films. Energies 2016, 9, 254.

[62] B. Qi, J. Wang. Open-circuit Voltage in Organic Solar Cells. J. Mater. Chem. 2012, 22, 24315.

[63] D. Woehrle, D. Meissner. Organic Solar Cells. Adv. Mater.1991, 3, No. 3.

[64] B. Gregg. Excitonic Solar Cells. The Journal of Physical Chemistry B 2003, 107, 4688-4698.

[65] C. Brabec. Organic Photovoltaics: Technology And Market. Solar Energy Materials and Solar Cells 2004, 83, 273-292.

[66] Bernède, J. Organic Photovoltaic Cells: History, Principle and Techniques. Journal of the Chilean Chemical Society 2008, 53.

[67] T. Clarke, J. Durrant. Charge Photogeneration In Organic Solar Cells. Chemical Reviews 2010, 110, 6736-6767.

[68] C. Tang. Two-Layer Organic Photovoltaic Cell. Applied Physics Letters 1986, 48, 183-185.

[69] G. Yu, J. Gao, et al. Polymer Photovoltaic Cells: Enhanced Efficiencies via a Network of Internal Donor-Acceptor Heterojunctions. Science 1995, 270, 17891791.

[70] J.J.M. Halls, et al. Efficient photodiodes from interpenetrating polymernetworks. Nature 1995, 376, 498500.

[71] A. L. Ayzner, C. J. Tassone, et al. Reappraising the Need for Bulk Heterojunctions in Polymer-Fullerene Photovoltaics: The Role of Carrier Transport in All-Solution-Processed P3HT/PCBM Bilayer Solar Cells, J. Phys. Chem. C 2009, 113, 20050–20060.

[72] G. Garcia-Belmonte, A. Munar, et al. Charge Carrier Mobility And Lifetime Of Organic Bulk Heterojunctions Analyzed By Impedance Spectroscopy. Organic Electronics 2008, 9, 847-851.

[73] F. Fabregat-Santiago, G. Garcia-Belmonte, I. Mora-Seró, J. Bisquert. Characterization Of Nanostructured Hybrid And Organic Solar Cells By

Impedance Spectroscopy. Physical Chemistry Chemical Physics 2011, 13, 9083.

[74] G. Dibb, M. Muth, et al. Influence Of Doping On Charge Carrier Collection In Normal And Inverted Geometry Polymer:Fullerene Solar Cells. Scientific Reports 2013, 3.

[75] K. Tvingstedt, K. Vandewal, et al. Electroluminescence From Charge Transfer States In Polymer Solar Cells. Journal of the American Chemical Society 2009, 131, 11819-11824.

[76] C. Deibel, T. Strobel, V. Dyakonov. Role Of The Charge Transfer State In Organic Donor-Acceptor Solar Cells. Advanced Materials 2010, 22, 4097-4111.

[77] C. Wehrenfennig, G. Eperon, et al. High Charge Carrier Mobilities And Lifetimes In Organolead Trihalide Perovskites. Advanced Materials 2013, 26, 1584-1589.

[78] W. Nie, H. Tsai, et al. High-Efficiency Solution-Processed Perovskite Solar Cells With Millimeter-Scale Grains. Science 2015, 347, 522-525.

[79] S. Stranks, G. Eperon, et al. Electron-Hole Diffusion Lengths Exceeding 1 Micrometer In An Organometal Trihalide Perovskite Absorber. Science 2013, 342, 341-344.

[80] V. Gonzalez-Pedro, E.Juarez-Perez, et al. General Working Principles Of $Ch_3NH_3PbX_3$ Perovskite Solar Cells. Nano Letters 2014, 14, 888-893.

[81] V. D'Innocenzo, G. Grancini, et al. Excitons Versus Free Charges In Organo-Lead Tri-Halide Perovskites. Nature Communications 2014, 5.

[82] K. Tanaka, T. Takahashi, et al. Comparative Study On The Excitons In Lead-Halide-Based Perovskite-Type Crystals $Ch_3NH_3PbBr_3$ $Ch_3NH_3PbI_3$. Solid State Communications 2003, 127, 619-623.

[83] A. Miyata, A. Mitioglu, et al. Direct Measurement Of The Exciton Binding Energy And Effective Masses For Charge Carriers In Organic-Inorganic Tri-Halide Perovskites. Nature Physics 2015, 11, 582-587.

[84] H. S. Kim, et al. Lead Iodide Perovskite Sensitized All-Solid-State Submicron Thin Film Mesoscopic Solar Cell With Efficiency Exceeding 9%. Sci. Rep. 2012, 2, 591.

[85] J.H. Heo, et al. Efficient Inorganic-Organic Hybrid Heterojunction Solar Cells Containing Perovskite Compound and Polymeric Hole Conductors. Nat. Photon.2013, 7, 486-491.

[86] J. Burschka, et al. Sequential Deposition as a Route to High-Performance Perovskite-Sensitized Solar Cells. Nature 2013, 499, 316319.

[87] T. Salim, S. Sun, et al. Perovskite-Based Solar Cells: Impact Of Morphology And Device Architecture On Device Performance. J. Mater. Chem. A 2015, 3, 8943-8969.

[88] L. Meng, J. You, et al. Recent Advances In The Inverted Planar Structure Of Perovskite Solar Cells. Accounts of Chemical Research 2016, 49, 155-165.

[89] E. Juarez-Perez, M. Wuler, et al. Role Of The Selective Contacts In The Performance Of Lead Halide Perovskite Solar Cells. The Journal of Physical Chemistry Letters 2014, 5, 680-685.

[90] P. Boix, K. Nonomura, et al. Current Progress And Future Perspectives For Organic/Inorganic Perovskite Solar Cells. Materials Today 2014, 17, 16-23.

[91] J. Liu, S. Chen, et al. Fast Charge Separation In A Non-Fullerene Organic Solar Cell With A Small Driving Force. Nature Energy 2016, 1, 16089.

[92] L. Pettersson, L. Roman, O. Inganäs. Modeling Photocurrent Action Spectra Of Photovoltaic Devices Based On Organic Thin Films. Journal of Applied Physics 1999, 86, 487-496

[93] Z. He, C. Zhong, et al. Enhanced Power-Conversion Efficiency In Polymer Solar Cells Using An Inverted Device Structure. Nature Photonics 2012, 6, 593-597.

[94] A. Martinez-Otero, X. Elias, et al. Solar Cells: High-Performance Polymer Solar Cells Using An Optically Enhanced Architecture. Advanced Optical Materials 2013, 1, 36-36.

[95] K. Kim, T. Pfadler, et al. Decoupling Optical And Electronic Optimization Of Organic Solar Cells Using High-Performance Temperature-Stable TiO_2/Ag/TiO_2 Electrodes. APL Materials 2015, 3, 106105.

[96] R. Betancur, A. Martinez-Otero, et al. Optical Interference For The Matching Of The External And Internal Quantum Efficiencies In Organic Photovoltaic Cells. Solar Energy Materials and Solar Cells 2012, 104, 87-91.

[97] Y. Galagan, M. Debije, P. Blom. Semitransparent Organic Solar Cells With Organic Wavelength Dependent Reflectors. Applied Physics Letters 2011, 98, 043302.

[98] W. Yu, X. Jia, et al. Highly Efficient Semi-transparent Polymer Solar Cells With Color Rendering Index Approaching 100 Using One-Dimensional Photonic Crystal. ACS Applied Materials and Interfaces 2015, 7, 9920-9928.

[99] R. Lunt, V. Bulovic. Transparent, Near-Infrared Organic Photovoltaic Solar Cells For Window And Energy-Scavenging Applications. Applied Physics Letters 2011, 98, 113305.

[100] R. Betancur, P. Romero-Gomez, et al. Transparent Polymer Solar Cells Employing A Layered Light-Trapping Architecture. Nature Photonics 2013, 7, 995-1000.

[101] C.C. Chen et al. Visibly Transparent Polymer Solar Cells Produced by Solution Processing. ACS Nano 2012, 6, 71857190

[102] L. Dou et al. A Selenium-Substituted Low-Bandgap Polymer with Versatile Photovoltaic Applications. Adv. Mater. 2013, 25, 825831.

[103] C.C. Chueh et al. Toward High-Performance Semi-Transparent Polymer Solar Cells: Optimization of Ultra-Thin Light Absorbing Layer and Transparent Cathode Architecture. Adv.Energy Mater. 2013, 417423.

[104] W. Yu, L. Shen, L, et al. Simultaneous Improvement In Efficiency And Transmittance Of Low Bandgap Semitransparent Polymer Solar Cells With One-Dimensional Photonic Crystals. Solar Energy Materials and Solar Cells 2013, 117, 198-202.

[105] W. Yu, Y. Long, et al. Semitransparent Polymer Solar Cells With One-Dimensional (WO_3/LiF)N Photonic Crystals. Applied Physics Letters 2012, 101, 153307.

[106] J. Choi, H. Cho, et al. Enhancement Of Organic Solar Cell Efficiency By Patterning The PEDOT:PSS Hole Transport Layer Using Nanoimprint Lithography. Organic Electronics 2013, 14, 3180-3185.

[107] L. Zhou, Q. Ou, et al. Light Manipulation For Organic Optoelectronics Using Bio-Inspired Moth's Eye Nanostructures. Scientific Reports 2014, 4.

[108] W. Lan, Y. Cui, et al. Broadband Light Absorption Enhancement In Moth's Eye Nanostructured Organic Solar Cells. AIP Advances 2015, 5, 057164.

[109] X. Li, W.C.H. Choy, et al. Efficiency Enhancement of Organic Solar Cells by Using Shape-Dependent Broadband Plasmonic Absorption in Metallic Nanoparticles. Adv. Funct. Mater. 2013, 23, 27282735.

[110] H.F. Zarick, O. Hurd, et al. Enhanced Efficiency in Dye-Sensitized Solar Cells with Shape-Controlled Plasmonic Nanostructures. ACS Photonics 2014, 1, 806811.

[111] S. In, D.R. Mason, et al. Enhanced Light Trapping and Power Conversion Efficiency in Ultrathin Plasmonic Organic Solar Cells: A Coupled Optical-Electrical Multiphysics Study on the Effect of Nanoparticle Geometry. ACS Photonics 2015, 2 (1), 7885.

[112] K. Tvingstedt, N. Persson, et al. Surface Plasmon Increase Absorption In Polymer Photovoltaic Cells. Applied Physics Letters 2007, 91, 113514.

[113] B. Niesen, B. Rand, et al. Plasmonic Efficiency Enhancement Of High Performance Organic Solar Cells With A Nanostructured Rear Electrode. Advanced Energy Materials 2012, 3, 145-150.

[114] S. Lee, J. Kim, et al. Plasmonic Organic Solar Cell Employing Au NP:PEDOT:PSS Doped Rgo. RSC Adv. 2015, 5, 23892-23899.

[115] L. Lu, Z. Luo, et al. Cooperative Plasmonic Effect Of Ag And Au Nanoparticles On Enhancing Performance Of Polymer Solar Cells. Nano Letters 2013, 13, 59-64.

[116] D. Wang, D. Kim, et al. Enhancement Of Donor-Acceptor Polymer Bulk Heterojunction Solar Cell Power Conversion Efficiencies By Addition Of Au

Nanoparticles (Angew. Chem. 24/2011). Angewandte Chemie 2011, 123, n/a-n/a.

[117] D. Wang, J. Kim, et al. Enhanced Light Harvesting In Bulk Heterojunction Photovoltaic Devices With Shape-Controlled Ag Nanomaterials: Ag Nanoparticles Versus Ag Nanoplates. RSC Advances 2012, 2, 7268.

[118] D.Chi, S. Lu, et al. Fully Understanding The Positive Roles Of Plasmonic Nanoparticles In Ameliorating The Efficiency Of Organic Solar Cells. Nanoscale 2015, 7, 15251-15257.

[119] F. Pastorelli, S. Bidault, et al. Self-Assembled Plasmonic Oligomers For Organic Photovoltaics. Advanced Optical Materials 2013, 2, 171-175.

[120] T. Ameri, G. Dennler, et al. Organic Tandem Solar Cells: A review, Energy Environ. Sci. 2009, 2, 347–363.

[121] N. Li, C. Brabec. Air-Processed Polymer Tandem Solar Cells With Power Conversion Efficiency Exceeding 10%. Energy Environ. Sci. 2015, 8, 2902-2909.

[122] C. Chen, W. Chang, et al. An Efficient Triple-Junction Polymer Solar Cell Having A Power Conversion Efficiency Exceeding 11%. Advanced Materials 2014, 26, 5670-5677.

[123] S. Kouijzer, S. Esiner, et al. Efficient Inverted Tandem Polymer Solar Cells With A Solution-Processed Recombination Layer. Advanced Energy Materials 2012, 2, 945-949.

[124] Z. Tang, Z. George, et al. Semi-Transparent Tandem Organic Solar Cells With 90% Internal Quantum Efficiency. Advanced Energy Materials 2012, 2, 1467-1476.

[125] http://www.heliatek.com/en/news/news/details/heliatek-sets-new-organic-photovoltaic-world-record-efficiency-of-13-2-228.

[126] J. You , C.-C. Chen , et al. 10.2% Power Conversion Effi ciency Polymer Tandem Solar Cells Consisting of Two Identical Sub-Cells, Adv. Mater. 2013, 25, 39733978.

[127] D. Bahro, M. Koppitz, et al. Understanding the External Quantum Effi ciency of Organic Homo-Tandem Solar Cells Utilizing a Three-Terminal Device Architecture, Adv. Energy Mater. 2015, 5, 1501019.

[128] H. Kang, S. Kee , et al. Simplified Tandem Polymer Solar Cells with an Ideal Self-Organized Recombination Layer, Adv. Mater. 2015, 27, 14081413.

[129] S. Reynolds, V. Smirnov. Modelling Performance of Two- and Four-terminal Thin-film Silicon Tandem Solar Cells Under Varying Spectral Conditions, Energy Procedia 2015, 84, 251-260.

[130] R. Gehlhaar, D. Cheynsa, et al. Four-terminal Organic Solar Cell Modules with Increased Annual Energy Yield. Proc. of SPIE 2013 Vol. 8830 88300I-1.

[131] J. Yang, R. Zhu, et al. A Robust Inter-connecting Layer for Achieving High Performance Tandem Polymer Solar Cells, Adv. Mater. 2011, 23, 3465–3470.

[132] J. You, Z. Hong, et al. Recent Trends In Polymer Tandem Solar Cells Research. Progress in Polymer Science 2013, 38, 1909-1928.

[133] J. Mailoa, C. Bailie, et al. A 2-Terminal Perovskite/Silicon Multijunction Solar Cell Enabled By A Silicon Tunnel Junction. Applied Physics Letters 2015, 106, 121105.

[134] Y. Özen, N. Akin, et al. S. Performance Evaluation Of A GaInP/GaAs Solar Cell Structure With The Integration Of AlGaAs Tunnel Junction. Solar Energy Materials and Solar Cells 2015, 137, 1-5.

[135] A. Hadipour, B. de Boer, et al. Solution-Processed Organic Tandem Solar Cells. Advanced Functional Materials 2006, 16, 1897-1903.

[136] A. Yakimov, S. Forrest. High Photovoltage Multiple-Heterojunction Organic Solar Cells Incorporating Interfacial Metallic Nanoclusters. Applied Physics Letters 2002, 80, 1667.

[137] D. Zhao, X. Sun, et al. Efficient Tandem Organic Solar Cells With An Al/MoO_3 Intermediate Layer. Applied Physics Letters 2008, 93, 083305.

[138] S. Hau, H. Yip, et al. Solution Processed Inverted Tandem Polymer Solar Cells With Self-Assembled Monolayer Modified Interfacial Layers. Applied Physics Letters 2010, 97, 253307.

[139] T. Abachi, L. Cattin, et al. Highly Flexible, Conductive And Transparent MoO_3/Ag/MoO_3 Multilayer Electrode For Organic Photovoltaic Cells. Thin Solid Films 2013, 545, 438-444.

[140] N. P. Sergeant, A. Hadipour, et al. Design of Transparent Anodes for Resonant Cavity Enhanced Light Harvesting in Organic Solar Cells, Adv. Mater. 2012, 24, 728–732.

[141] W. Cao, Y. Zheng, et al. Flexible Organic Solar Cells Using An Oxide/Metal/Oxide Trilayer As Transparent Electrode. Organic Electronics 2012, 13, 2221-2228.

[142] S. Schubert, J. Meiss, et al. Improvement Of Transparent Metal Top Electrodes For Organic Solar Cells By Introducing A High Surface Energy Seed Layer. Advanced Energy Materials 2013, 3, 438-443.

[143] A. Mertens, J. Mescher, et al. Understanding The Angle-Independent Photon Harvesting In Organic Homo-Tandem Solar Cells. Optics Express 2016, 24, A898.

[144] J. Mescher, A. Mertens, et al. Illumination Angle And Layer Thickness Influence On The Photo Current Generation In Organic Solar Cells: A Combined Simulative And Experimental Study. AIP Advances 2015, 5, 077188.

[145] J. Ball, S. Stranks, et al. Optical Properties And Limiting Photocurrent Of Thin-Film Perovskite Solar Cells. Energy Environ. Sci. 2015, 8, 602-609.

[146] J.D. Jackson. Classical Electrodynamics. Chapter 6. John Wiley and Sons. 1998

[147] S. Lu , X. Guan, et al. A New Interconnecting Layer of Metal Oxide/Dipole Layer/Metal Oxide for Efficient Tandem Organic Solar Cells, Adv. Energy Mater. 2015, 1500631.

[148] S. Esiner, R. E. M. Willems, et al. Photoelectrochemical Water Splitting in an Organic Artificial Leaf, J. Mater. Chem. A 2015, 3, 23936.

[149] S. Esiner , H. Eersel, et al. Triple Junction Polymer Solar Cells for Photoelectrochemical Water Splitting, Adv. Mater. 2013, 25, 29322936.

[150] P. Mantilla-Perez, A. Martinez-Otero, et al. 4-Terminal Tandem Photovoltaic Cell Using Two Layers of PTB7:$PC_{71}BM$ for an Optimal Light Absorption, ACS Appl. Mater. Interfaces 2015, 7, 184351844.

[151] E. D. Palik. Handbook of Optical Constants of Solids (Academic, 1998), Vol. I.

[152] https://www.norlandprod.com/adhesives/noa%2065.html

[153] J. Bulíř, M. Novotný, et al. Preparation of Nanostructured Ultrathin Silver Layer. J. Nanophoton. 2011, 5(1), 051511.

[154] K.M. McPeak, S. V. Jayant, et al. Plasmonics Films Can Easily Be Better: Rules and Recipes, ACS Photonics 2015, 2, 326–333.

[155] A. D. Rakić, A. B. Djurišic, et al. Optical Properties of Metallic Films for Vertical-Cavity Optoelectronic Devices, Appl. Opt. 1998, 37, 5271–5283.

https://www.norlandprod.com/adhesives/noa

[156] R. Strandberg. Detailed Balance Analysis Of Area De-Coupled Double Tandem Photovoltaic Modules. Applied Physics Letters 20015, 106, 033902.

[157] F. Guo, N. L, et al. A Generic Concept To Overcome Bandgap Limitations For Designing Highly Efficient Multi-Junction Photovoltaic Cells, Nat Commun. 2015, 6: 7730.

[158] S. Albrecht, M. Saliba, et al. Monolithic Perovskite/Silicon-Heterojunction Tandem Solar Cells Processed At Low Temperature. Energy Environ. Sci. 2016, 9, 81-88.

[159] D. Slotcavage, H. Karunadasa, M. McGehee. Light-Induced Phase Segregation In Halide-Perovskite Absorbers. ACS Energy Letters 2016, 1, 1199-1205.

[160] M. Saliba, T. Matsui, et al. Incorporation Of Rubidium Cations Into Perovskite Solar Cells Improves Photovoltaic Performance. Science 2016, 354, 206-209.

[161] J. Correa Baena, L. Steier, et al. Highly Efficient Planar Perovskite Solar Cells Through Band Alignment Engineering. EnergyEnviron. Sci. 2015, 8, 2928-2934.

[162] M. Filip, G. Eperon, H.J. Snaith, F. Giustino. Steric Engineering of Metal-halide Perovskites with Tunable Optical Band Gaps. Nat. Comms.2014, 5, 5757.

[163] Z. Yang, A. Rajagopal, et al. Stable Low-Bandgap Pb-Sn Binary Perovskites For Tandem Solar Cells, Advanced Materials 2016, 28, 8990-8997.

[164] G. Eperon, T. Leijtens, et al. Perovskite-Perovskite Tandem Photovoltaics With Optimized Bandgaps, Science 2016.

[165] T. Hara, T Maekawa, et al. Quantitative Assessment of Optical Gain and Loss in Submicron-Textured CuIn1xGaxSe2 Solar Cells Fabricated by Three-Stage Coevaporation. Phys. Rev. Applied. 2014, 2, 034012.

[166] B. Macco, Y. Wu, et al. High Mobility In_2O_3:H Transparent Conductive Oxides Prepared By Atomic Layer Deposition And Solid Phase Crystallization. physica status solidi (RRL) - Rapid Research Letters 8, 2014, 987-990.

[167] J.P. Correa-Baena, M. Anaya, et al. Unbroken Perovskite: Interplay of Morphology, Electro-optical Properties, and Ionic Movement, Adv. Mater. 2016.

[168] C-W. Chen, S.-H. Hsiao, et al. Optical Properties of Organometal Halide Perovskite Thin Films and General Device Structure Design Rules for Perovskite Single and Tandem Solar Cells. J. Mater. Chem. A. 2015, 3, 9152–9159.

[169] B. Yang, O. Dyck, et al. Perovskite Solar Cells With Near 100% Internal Quantum Efficiency Based On Large Single Crystalline Grains And Vertical Bulk Heterojunctions. J. Am. Chem. Soc. 2015, 137, 9210-9213.

[170] Q. Lin, A. Armin, et al. Electro-Optics Of Perovskite Solar Cells. Nature Photonics 2014, 9, 106-112.

[171] J. Pettersson, T. Torndah, et al. The Influence of Absorber Thickness on Cu(In, Ga)Se2 Solar Cells With Different Buffer Layers. IEEE, Journal of Photovoltaics 2013, 3.

[172] J.H. Wi, T.G. Kim, et al. Chung, Photovoltaic Performance and Interface Behaviors of Cu(In,Ga)Se2 Solar Cells with a Sputtered-Zn(O,S) Buffer

Layer by High-Temperature Annealing, ACS Appl. Mater. Interfaces, 2015, 7 (31), pp 17425–17432.

[173] T. Duong, N. Lal, et al. Semitransparent Perovskite Solar Cell With Sputtered Front And Rear Electrodes For A Four-Terminal Tandem. IEEE Journal of Photovoltaics 2016, 6, 679-687.

[174] A. Fakharuddin, F. Di Giacomo, et al. Vertical TiO_2 Nanorods As A Medium For Stable And High-Efficiency Perovskite Solar Modules. ACS Nano 2015, 9, 8420-8429.

[175] R. Gehlhaar, T. Merckx, et al. Perovskite Solar Modules with Minimal Area Loss Interconnections. SPIE Newsroom 2015, 10.1117/2.1201509.006116 Page 2/3.

[176] S. Nishiwaki, A. Burn, et al. A Monolithically Integrated High-efficiency Cu(In,Ga)Se2 Mini-module structured solely by laser. Prog. Photovolt: Res. Appl. 2015, 23:1908–1915.

[177] F. Guo, P. Kubis, et al. Solution-Processed Parallel Tandem Polymer Solar Cells Using Silver Nanowires as Intermediate Electrode. ACS Nano 2014, 8 (12), pp 12632–12640.

[178] M. Reinhard, R. Eckstein, et al. Solution-Processed PolymerSilver Nanowire Top Electrodes For Inverted Semi-Transparent Solar Cells. Organic Electronics 2013, 14, 273-277.

[179] Z. Tang, Z. George, et al. Semi-Transparent Tandem Organic Solar Cells With 90% Internal Quantum Efficiency. Advanced Energy Materials 2012, 2, 1467-1476.

[180] J. Yim, S. Joe, et al. Fully Solution-Processed Semi-transparent Organic Solar Cells With A Silver Nanowire Cathode And A Conducting Polymer Anode. ACS Nano 2014, 8, 2857-2863.

[181] Y. Zhou, H. Cheun, et al. Optimization Of A Polymer Top Electrode For Inverted Semi-transparent Organic Solar Cells. Organic Electronics 2011, 12, 827-831.

[182] Z. Liu, P. You, et al. Neutral-Color Semi-transparent Organic Solar Cells With All-Graphene Electrodes. ACS Nano 2015, 9, 12026-12034.

[183] T. Eggenhuisen, Y. Galagan, et al. High Efficiency, Fully Inkjet Printed Organic Solar Cells With Freedom Of Design. J. Mater. Chem. A 2015, 3, 7255-7262.

[184] Y. Galagan, E. Coenen, et al. Photonic Sintering Of Inkjet Printed Current Collecting Grids For Organic Solar Cell Applications. Organic Electronics 2013, 14, 38-46.

[185] B. Patil, S. Shanmugam, et al. All-Solution Processed Organic Solar Cells With Top Illumination. Organic Electronics 2015, 21, 40-46.

[186] Y. Sun, J. Seo, et al. Inverted Polymer Solar Cells Integrated with a Low-temperature-annealed Solgel-derived ZnO Film as an Electron Transport Layer. Adv. Mater. 2011, 23, 16791683.

[187] S. Xie, Z. Ouyang, et al. Large-size High-uniformity Random Silver Nanowire Networks as Transparent Electrodes for Crystalline Silicon Wafer Solar Cells. Opt. Express 2013, Vol. 21, No. S3.

[188] F. Guo, P. Kubis, et al. Fully Solution-Processing Route toward Highly Transparent Polymer Solar Cells. ACS Appl. Mater. Interfaces, 2014, 6 (20), pp 1825118257.

[189] J. Czolk, D. Landerer, et al. Highly Efficient, Mechanically Flexible, Semi-Transparent Organic Solar Cells Doctor Bladed from Non-Halogenated Solvents. Advanced Materials Technologies, 1600184.

[190] B. Ecker , J. C. Nolasco, et al. Degradation Effects Related to the Hole Transport Layer in Organic Solar Cells, Adv. Funct. Mater. 2010, 17.